N73 25830

NASA TECHNICAL NOTE

N73-25830

NASA TN D-7163

NASA TN D-7163

CASE FILE COPY

EFFECTS OF FINENESS AND CLOSURE RATIOS ON BOATTAIL DRAG OF CIRCULAR-ARC AFTERBODY MODELS WITH JET EXHAUST AT MACH NUMBERS UP TO 1.3

by David E. Reubush

Langley Research Center
Hampton, Va. 23365

NATIONAL AERONAUTICS AND SPACE ADMINISTRATION • WASHINGTON, D. C. • MAY 1973

1. Report No.	2. Government Accession No.	3. Recipient's Catalog No.
NASA TN D-7163		

4. Title and Subtitle	5. Report Date
EFFECTS OF FINENESS AND CLOSURE RATIOS ON BOAT-TAIL DRAG OF CIRCULAR-ARC AFTERBODY MODELS WITH JET EXHAUST AT MACH NUMBERS UP TO 1.30	May 1973
	6. Performing Organization Code
7. Author(s)	8. Performing Organization Report No.
David E. Reubush	L-8678
	10. Work Unit No.
9. Performing Organization Name and Address	764-64-60-02
NASA Langley Research Center Hampton, Va. 23365	11. Contract or Grant No.
	13. Type of Report and Period Covered
12. Sponsoring Agency Name and Address	Technical Note
National Aeronautics and Space Administration Washington, D.C. 20546	14. Sponsoring Agency Code

15. Supplementary Notes

16. Abstract

The effects of variations in fineness ratio and closure ratio on the boattail drag of circular-arc afterbody models have been investigated at static conditions and at Mach numbers from 0.40 to 1.30. Jet total-pressure ratio was varied from jet off to about 6, depending on Mach number. Reynolds number based on model maximum diameter varied from about 1.20×10^6 to 2.18×10^6. Angle of attack was varied from -4^o to 8^o. The results indicate that, at subsonic speeds before the drag rise and at a scheduled pressure ratio, the total drag (pressure plus calculated skin friction) is approximately equal for configurations with the same closure ratio. Also, for configurations with the same closure ratio, increasing fineness ratio results in an increased drag-rise Mach number; and for configurations with the same fineness ratio, increasing closure ratio results in an increased drag-rise Mach number.

17. Key Words (Suggested by Author(s))	18. Distribution Statement
Afterbody drag Jet interference effects Circular-arc boattails Jet-engine exhaust nozzles	Unclassified – Unlimited

19. Security Classif. (of this report)	20. Security Classif. (of this page)	21. No. of Pages	22. Price*
Unclassified	Unclassified	120	$3.00

*For sale by the National Technical Information Service, Springfield, Virginia 22151

EFFECTS OF FINENESS AND CLOSURE RATIOS ON BOATTAIL DRAG OF CIRCULAR-ARC AFTERBODY MODELS WITH JET EXHAUST AT MACH NUMBERS UP TO 1.30

By David E. Reubush
Langley Research Center

SUMMARY

The effects of variations in fineness ratio and closure ratio on the boattail drag of circular-arc afterbody models have been investigated at static conditions and at Mach numbers from 0.40 to 1.30. Angle of attack was varied from -4° to 8°. Jet total-pressure ratio was varied from jet off to about 6, depending on Mach number. Reynolds number based on model maximum diameter varied approximately from 1.20×10^6 to 2.18×10^6.

The results of this investigation indicate (1) that for configurations with the same closure ratio, increasing fineness ratio results in lower pressure drag and a higher drag-rise Mach number and (2) that for configurations with the same fineness ratio, increasing closure ratio generally results in lower pressure drag and an increased drag-rise Mach number. For all configurations at most subsonic Mach numbers, going from jet off to jet on generally had a greater effect on lowering pressure drag than did further increases in pressure ratio for the range of pressure ratios tested. Also, at subsonic speeds before the drag rise and at a scheduled jet total-pressure ratio, the total drag (pressure plus calculated skin friction) is approximately equal for configurations with the same closure ratio. Pressure axial force increased with increasing angle of attack but pressure drag decreased.

INTRODUCTION

With the projected cruising speed of the next generation of transports approaching sonic velocity, the need for information to enable the designer to push the drag-rise Mach number to the highest possible value has become especially acute.

One of the particularly important areas of an aircraft where drag information is needed is that of the afterbody-nozzle region. For low-drag configurations the drag of this portion of the aircraft can be a large percentage of the total drag. At present, theoretical methods are not fully satisfactory in predicting accurately the drag of this area

(especially with the presence of exhaust flow), and, as a result, designers must rely on wind-tunnel data to assist in the design process.

There have been numerous previous investigations of afterbodies and jet-exhaust nozzles, both in isolated nacelles and installed on twin-engine configurations (see, for example, refs. 1 to 8). An afterbody shape which has shown promise of lower drag is the circular-arc type (see ref. 5); as yet, however, there have been no systematic investigations to yield data on the effects of parametric variations in length and exit size on the drag of this type of afterbody.

As part of the program to develop technology applicable to the design of a near-sonic transport, a parametric investigation of circular-arc afterbodies (with convergent internal nozzle contour) was conducted in the Langley 16-foot transonic tunnel. The primary purpose of this investigation was to obtain pressure-drag data on a series of circular-arc boattails with variations in fineness ratio and closure ratio. A secondary purpose was to obtain thrust and thrust-minus-drag data for these nozzles. Tested in this investigation were five configurations with variations in fineness ratio from 1.0 to 2.0 and with closure ratios of 0.6 and 0.7. A related study of variation only in fineness ratio for boattails of 0.5 closure ratio can be found in reference 4. A limited amount of data from reference 4 for a boattail with 1.0 fineness ratio is presented for comparison purposes in the present paper. The boattail models were mounted on a cone-cylinder single-engine nacelle model which used high-pressure air at near room temperature to simulate the jet exhaust. The investigation was conducted statically and at Mach numbers ranging from 0.40 to 1.30 at angles of attack from -4° to 8°. Jet total-pressure ratio (ratio of jet total pressure to free-stream static pressure) was varied from jet off to about 6, depending on Mach number.

SYMBOLS

A	cross-sectional area, m^2
A_{bel}	effective annular area between metal bellows and surrounding sleeve, m^2
A_m	maximum cross-sectional area of model, m^2
A_t	throat area, m^2
A_β	incremental area assigned to one static pressure orifice of boattail (either axial projection or normal projection), m^2

$C_{A,\beta}$ pressure-axial-force coefficient of boattail, $F_{A,\beta}/qA_m$

C_D drag coefficient

$C_{D,f}$ skin-friction drag coefficient of boattail, $D_{f,\beta}/qA_m$

$C_{D,n}$ total-drag coefficient of boattail, D_n/qA_m

$C_{D,\beta}$ pressure-drag coefficient of boattail, D_β/qA_m

$C_{F,i}$ aerodynamic ideal-thrust coefficient, F_i/qA_m

$C_{N,\beta}$ pressure-normal-force coefficient of boattail, $F_{N,\beta}/qA_m$

C_d discharge coefficient, $\dot{m}_j/\dot{m}_i$

C_p pressure coefficient of boattail, $\frac{p_\beta - p_\infty}{q}$

$C_{p,b}$ base-pressure coefficient, $\frac{p_b - p_\infty}{q}$

$D_{f,cyl}$ calculated flat-plate skin friction on cylindrical portion of model between stations 52.07 cm and 121.92 cm, N

$D_{f,\beta}$ calculated flat-plate skin friction on boattail (i.e., portion of model aft of station 121.92 cm), N

D_n total drag of boattail, $D_{f,\beta} + D_\beta$, N

D_β pressure drag of boattail, N

d_b base diameter, m

d_e exit diameter, m

d_m maximum diameter of model, m

$F_{A,\beta}$ pressure axial force of boattail, N

$F_{N,\beta}$ pressure normal force of boattail, N

F_{bal}	force sensed by balance, N
F_i	ideal isentropic gross thrust, N
F_j	gross thrust of nozzle, N
l	length of boattail measured from station 121.92 cm
M	free-stream Mach number
$\dot{m}_i$	ideal mass-flow rate, kg/s
$\dot{m}_j$	measured mass-flow rate, kg/s
p_b	base pressure, N/m^2
p_{cav}	cavity pressure, N/m^2
p_{down}	pressure acting on downstream bellows, N/m^2
$p_{t,j}$	jet total pressure, N/m^2
p_{up}	pressure acting on upstream bellows, N/m^2
p_β	static pressure of boattail, N/m^2
p_∞	free-stream static pressure, N/m^2
q	free-stream dynamic pressure, N/m^2
R	gas constant, 287.3 N-m/kg-K; also, circular-arc radius of boattail (see fig. 4), m
r	radial dimension from center line of model, cm
r_m	maximum radius of model, m
S	length of nozzle convergent section (see fig. 4), m
s	internal axial coordinate in convergent section (see fig. 4), m

$T_{t,j}$	jet total temperature, K
t	nozzle throat length (see fig. 4), m
X	axial coordinate from nose of model (see fig. 3), m
x	axial coordinate from start of boattail at station 121.92 (see fig. 4), m
α	angle of attack of model, deg
β	terminal angle of boattail, deg
β_c	chord angle of boattail, deg
γ	ratio of specific heats
ϕ	meridian angle about afterbody axis (clockwise direction positive facing upstream, 0^o at top of model), deg

APPARATUS AND PROCEDURE

Wind Tunnel

The investigation was conducted in the Langley 16-foot transonic tunnel, which is a single-return, continuous, atmospheric tunnel. The test section is a regular octagon in cross section with slots at the corners of the octagon. The tunnel has a continuously variable speed range from M = 0.20 to 1.30. Further description of the Langley 16-foot transonic tunnel can be found in references 9 and 10.

Model and Support System

The air-powered cone-cylinder nacelle model on which the various afterbodies were mounted for this investigation is shown in figure 1 with a typical configuration attached. Dry, high-pressure air at a stagnation temperature of about 274 K is introduced perpendicularly to the model axis into that portion of the nacelle supported by the balance (shown by the fine hatching in fig. 1). Air passage from the high-pressure plenum to the low-pressure plenum is through eight multiholed sonic nozzles spaced in equal angles around the axis of the high-pressure plenum. Since the eight nozzles are not supported by the balance and since the air is introduced perpendicularly to the model axis, the balance measures only the thrust developed by the rearward acceleration of the air. The low-pressure air chamber into which the air is introduced is sealed by a set of

flexible metal bellows arranged so that the net axial force caused by pressurization of the system is zero. The flow-smoothing screens in the model tail pipe were constructed of 0.635-cm-mesh, 0.0635-cm-diameter wire screen supported by four vanes. Figure 2 is a photograph of the nacelle model, with configuration 5 attached, installed in the Langley 16-foot transonic tunnel.

A sketch of the model and support system is shown in figure 3, along with corresponding cross-sectional area distributions. The model was supported in the tunnel by a sting-strut support system, with the swept strut being attached to the nose of the model as shown in figures 1, 2, and 3. The center line of the model was located on the wind-tunnel center line, with the center line of the sting 55.88 cm below that level. The cross section of the sting was 5.08 cm by 10.16 cm, with the top and bottom capped by half cylinders of 2.54-cm radius. The strut blade was 5 percent thick with a 50.8-cm chord in the streamwise direction and with the leading and trailing edges swept 45°. The model blockage was 0.099 percent of the test-section cross section, and the maximum blockage cross section of the model and support system was 0.148 percent.

Description of Afterbody Models

A detailed sketch of a typical afterbody with tables of dimensions for all the configurations is presented in figure 4. Photographs of the afterbodies are shown in figure 5. The internal contour of each of the nozzles is a modification of the standard exhaust nozzle described in reference 1. The contour was modifed to fit within dimensional constraints imposed by the external contour of the afterbody, wall thickness, and the necessary exit size. The throat (length t on fig. 4) was circular in cross section.

Instrumentation and Tests

Each of the afterbody models was equipped with a number of static pressure orifices (48 to 69 depending on configuration) at various stations on its surface (the longitudinal distribution of which was on an equal annular area basis). The location of the various orifices for the different configurations is given in table I. Each of these orifices was connected to an individual, remotely located, electrical pressure transducer. Forces and moments on the model downstream of the gap at model station 52.07 cm (see fig. 1) were measured simultaneously with the pressure measurements by using a three-component strain-gage balance. Jet total pressure and temperature were measured in the internal flow just ahead of the nozzle connect station by use of an area-weighted five-tube total-pressure rake and a thermocouple (see figs. 1 and 4). A flowmeter with axial flow impeller was used to measure the mass flow of the exhaust simulation air. Also there were special base plates available to obtain jet-off base pressures for each of the configurations. These plates were fitted inside the nozzle, flush with the exit, and

were instrumented with three pressure orifices (center, 2.79 cm from center toward 0°, and 2.79 cm from center toward 180°). To obtain these pressures, special runs were made with the plates in place and with jets off.

The tests were conducted in the Langley 16-foot transonic tunnel at $M = 0$ (static condition) and at $M = 0.40$ to 1.30 at $\alpha = -4^{\circ}$ to 8°. The model attitude was set so as to account for tunnel upflow, but possible sting deflection, which was found to be extremely small, was not taken into account. The ratio of jet total pressure to free-stream static pressure varied from jet off to approximately 6, depending on Mach number. While the Mach number and jet total-pressure ratio were held constant, 13 frames of force, moment, and pressure data were recorded, of which the average was used to compute the values of force, moment, and pressure coefficients and of jet stagnation temperature. The Reynolds number based on model maximum diameter varied approximately from 1.20×10^6 to 2.18×10^6. For all tests the model boundary-layer transition was fixed by a 0.254-cm strip of No. 100 carborundum grit, which was located 2.54 cm from the nose in accordance with techniques described in references 11 and 12.

Data Reduction

From the measured pressures on each boattail, coefficients of pressure axial force, normal force, and drag were computed. These coefficients were based on maximum cross-sectional area of the model and were obtained from the pressure data by assigning an incremental area to each orifice; these coefficients were computed from the following equations:

$$C_{A,\beta} = \frac{1}{qA_m} \sum_{i=1}^{n} \left(p_{\infty} - p_{\beta,i}\right) A_{\beta,i} \tag{1}$$

where $A_{\beta,i}$ are axial projected areas,

$$C_{N,\beta} = \frac{1}{qA_m} \sum_{i=1}^{n} \left(p_{\infty} - p_{\beta,i}\right) A_{\beta,i} \tag{2}$$

where $A_{\beta,i}$ are normal projected areas, and

$$C_{D,\beta} = C_{A,\beta} \cos \alpha + C_{N,\beta} \sin \alpha \tag{3}$$

No attempt was made to include the forces on the small rim at the nozzle exit between d_b and d_e (see fig. 4). Because of the possibility of strut interference (see refs. 1 and 4),

the computed values of $C_{A,\beta}$ ($\alpha = 0^{\circ}$ only) utilized only the top-row orifices which were considered interference free. Strut interference on boattail pressures is discussed in the appendix. Also, because of the possible errors in the step integration used for $C_{A,\beta}$, $C_{N,\beta}$, and $C_{D,\beta}$ where large pressure gradients exist, the accuracy of the step integration was spotchecked by comparing the results obtained by plotting top-row C_p as a function of $(r/r_m)^2$ and by integrating with a planimeter. The results of these checks were favorable.

Thrust minus drag on the metric portion of the model was measured with an internal three-component strain-gage balance (fig. 1). The forces measured by the balance F_{bal} include nozzle gross thrust F_j, external pressure and viscous forces from the gap station (52.07 cm) to the end of the boattail, and internal pressure tare forces. The nozzle thrust minus drag was computed utilizing the following equation:

$$F_j - D_n = F_{bal} + (p_{cav} - p_\infty)A_m + (p_{down} - p_{up})A_{bel} + D_{f,cyl} \tag{4}$$

In equation (4), the term F_{bal} is the axial force indicated by the balance, corrected for weight tares and balance interactions. The term $(p_{cav} - p_\infty)A_m$ is a tare force which accounts for the static-pressure difference between the inside of the model and the free stream. The cavity pressure was measured at 13 points within the model, and each pressure was assumed to act on an element of area of which the sum equaled A_m, the maximum cross-sectional area (see fig. 1). The term $(p_{down} - p_{up})A_{bel}$ is a bellows tare correction which by design should be essentially zero. However, when internal flow velocities are large, a small pressure difference between the ends of the bellows can exist (see fig. 1). In the present investigation the maximum bellows tare was about 0.5 percent of ideal isentropic gross thrust F_i. The term $D_{f,cyl}$ is the calculated flat-plate skin friction on the cylindrical portion of the afterbody between the metric break and the beginning of the boattail. For static tests (M = 0) the afterbody drag is zero and the thrust ratio reduces to F_j/F_i. Also, for wind-on tests, the nozzle drag D_n obtained from pressure integration and skin-friction calculation has been added in to obtain F_j/F_i.

The ideal isentropic gross thrust is

$$F_i = \dot{m}_j\sqrt{\frac{2\gamma}{\gamma - 1}RT_{t,j}\left[1 - \left(\frac{p_\infty}{p_{t,j}}\right)^{\frac{\gamma-1}{\gamma}}\right]} \tag{5}$$

The nozzle discharge coefficient is defined as the ratio of measured mass flow to ideal mass flow; that is,

$$C_d = \frac{\dot{m}_j}{\dot{m}_i} \tag{6}$$

where

$$\dot{m}_i = A_t p_{t,j} \sqrt{\frac{\gamma}{RT_{t,j}} \left(\frac{2}{\gamma + 1} \right)^{\frac{\gamma+1}{\gamma-1}}}$$

for choked flow and

$$\dot{m}_i = A_t p_{t,j} \left(\frac{p_\infty}{p_{t,j}} \right)^{1/\gamma} \sqrt{\frac{2\gamma}{(\gamma - 1)RT_{t,j}} \left[1 - \left(\frac{p_\infty}{p_{t,j}} \right)^{\frac{\gamma-1}{\gamma}} \right]}$$

for unchoked flow.

PRESENTATION OF RESULTS

The results of the investigation are presented in the following figures:

	Figure
Jet-off data –	
Boattail pressure-coefficient distributions	6 and 7
Base pressure coefficients	8
Drag coefficient variation with Mach number	9 to 12
Drag coefficient variation with fineness ratio	13
Drag coefficient variation with closure ratio	14
Jet-on data –	
Boattail pressure-coefficient distributions	15 to 19
Comparison with theory	20
Boattail drag coefficient variation with jet total-pressure ratio	21 to 24
Drag coefficient cross plotted at a typical full-scale jet-total-pressure-ratio schedule	25 to 27
Angle-of-attack data –	
Boattail axial-force coefficient variation with jet total-pressure ratio and angle of attack	28 to 31
Boattail drag coefficient variation with jet total-pressure ratio and angle of attack	32 to 35

Figure

Typical boattail normal-force coefficient variation with angle of attack 36
Drag coefficient at various angles of attack cross plotted at a typical full-scale jet-total-pressure-ratio schedule 37

Force data –
Static thrust ratio variation with jet total-pressure ratio 38
Static discharge coefficient variation with jet total-pressure ratio 39
Wind-on thrust ratio variation with jet total-pressure ratio . . . . . 40 and 41
Thrust-minus-drag ratio variation with jet total-pressure ratio . . . . . 42 and 43
Aerodynamic ideal-thrust coefficients 44

DISCUSSION

All data except those found in figures 28 to 37 were obtained at an angle of attack of 0^{o}; hence boattail axial force and drag are the same.

Jet-Off Measurements

The data obtained from jet-off measurements in this investigation are shown in figures 6 to 14. All data are based on the top-row orifices because of the previously mentioned possibility (in the section entitled "Data Reduction") of strut interference on the other rows.

Pressure distributions.- Figure 6 presents the jet-off pressure-coefficient distributions at various Mach numbers for configurations 1 and 2 $\left(d_e/d_m = 0.6;\ l/d_m = 1.0 \text{ and } 1.5, \text{ respectively}\right)$. These data indicate that increasing fineness ratio for this value of closure ratio at subsonic speeds tends to reduce the magnitude of both the minimum and maximum pressures occurring on the boattail. The only exception is for Mach numbers at which the shorter of the two is separated and the longer one is not; the flow on the longer one will recompress to a higher pressure coefficient. At supersonic speeds the results were similar to the results at subsonic speeds.

The jet-off pressure-coefficient distributions for configurations 3, 4, and 5 $\left(d_e/d_m = 0.7;\ l/d_m = 1.0, 1.5, \text{ and } 2.0, \text{ respectively}\right)$ are shown in figure 7. The same trend with fineness ratio is observed for these three configurations as for the configurations with $d_e/d_m = 0.6$. As fineness ratio is increased at subsonic speeds, the pressure-coefficient curves tend to flatten out with both minimums and maximums decreasing as fineness ratio is increased. Again, at supersonic speeds, the higher the fineness ratio the higher the level of pressures on the boattail.

Base pressures.- Presented in figure 8 are the jet-off base-pressure coefficients obtained for all configurations through use of the base plates described previously. The data obtained for configurations 1 and 3 $\left(l/d_m = 1.0;\ d_e/d_m = 0.6 \text{ and } 0.7, \text{ respectively}\right)$

exhibit similar trends with increasing Mach number at subsonic speeds. Both have relatively constant positive base-pressure coefficients until about M = 0.90, at which point the pressures drop off abruptly. Configurations 2, 4, and 5 $\left(l/d_m = 1.5, 1.5, \text{and } 2.0; d_e/d_m = 0.6, 0.7, \text{and } 0.7, \text{respectively}\right)$ exhibit slightly different results in that at subsonic speeds the base-pressure coefficients are always increasing with Mach number. At supersonic speeds the results for all the configurations are similar in that all have relatively constant negative base-pressure coefficients.

Drag variation with Mach number.- The jet-off boattail pressure-drag variation with Mach number for the five configurations tested in this investigation, plus one from reference 4, are presented in figures 9, 10, 11, and 12. In the first two figures the configurations of constant closure ratio d_e/d_m are grouped together and in the second two those of constant fineness ratio l/d_m are grouped together.

Figure 9 presents the results for configurations 1 and 2 $\left(d_e/d_m = 0.6;\ l/d_m = 1.0 \text{ and } 1.5, \text{respectively}\right)$. As would be expected from the pressure distributions (fig. 6) the configuration with the higher fineness ratio (configuration 2) has lower pressure drag, both at subsonic and supersonic speeds. Also, it has a higher drag-rise Mach number. The indication of drag-rise Mach number used in the present paper is represented by the intersection of a linear fairing through the subsonic slope of the drag curve with a linear extrapolation of the steep supercritical portion of the curve.

Shown in figure 10 are the results for configurations 3, 4, and 5 $\left(d_e/d_m = 0.7;\ l/d_m = 1.0, 1.5, \text{and } 2.0, \text{respectively}\right)$. These results indicate similar trends to those found for the configurations with $d_e/d_m = 0.6$. As fineness ratio is increased for a constant closure ratio, the boattail pressure drag is decreased, both at subsonic and supersonic speeds, and the drag-rise Mach number is increased.

The results for the three configurations with $l/d_m = 1.0$ (configuration 1 with $d_e/d_m = 0.6$, configuration 3 with $d_e/d_m = 0.7$, and the configuration of reference 4 with $d_e/d_m = 0.5$) are presented in figure 11. The expected trend for these three configurations is that the jet-off boattail drag would decrease as the closure ratio is increased (i.e., an increase in closure ratio such as from 0.6 to 0.7). Although the results for configurations 1 and 3 bear out this trend, the subsonic results for the configuration of reference 4 seem to be anomalous, with the drag of this configuration being lowest of the three (before drag rise). It is shown in reference 4 that the flow on the boattail of this configuration is separated for most Mach numbers tested and that at subsonic speeds this separation has a large portion of the boattail under the influence of a positive pressure which tends to reduce the drag. Thus is explained why the configuration of reference 4 exhibits a lower jet-off drag than do configurations 1 and 3. Even though the subsonic drag levels do not progress in the expected manner for these configurations, they exhibit

the expected trends of giving lower drag-rise Mach number and higher supersonic drag at lower closure ratios.

Figure 12 presents the results for configurations 2 and 4 $\left(l/d_m = 1.5;\ d_e/d_m = 0.6\right.$ and 0.7, respectively$\left.\right)$. These data exhibit the expected trends of giving higher drag (both subsonic and supersonic) and lower drag-rise Mach number with the lower closure ratio.

Afterbody jet-off friction drag $C_{D,f}$, pressure drag $C_{D,\beta}$, and total drag $C_{D,n}$ are presented as a function of fineness ratio for configurations 3, 4, and 5 $\left(d_e/d_m = 0.7\right)$ at several Mach numbers in figure 13. As expected, higher fineness ratio gave higher friction drag but lower pressure drag. Since the differences in friction drag are not so great as the differences in pressure drag, the afterbody which had the highest fineness ratio and the lowest pressure drag also had the lowest jet-off total drag for all Mach numbers.

Figure 14 presents the jet-off friction drag, pressure drag, and total drag as a function of closure ratio for configurations 1 and 3 with $l/d_m = 1.0$ and the configuration of reference 4 with $l/d_m = 1.0$ at various Mach numbers. As in figure 10, the configurations with $d_e/d_m = 0.6$ and 0.7 exhibit the expected characteristic of higher closure ratio giving lower drag, whereas the configuration from reference 4 with $d_e/d_m = 0.5$ has the lowest subsonic drag until it reaches the drag rise.

Jet-On Measurements

Effects of jet operation on boattail pressure distributions.- Figures 15 to 19 show the effects of jet operation on the boattail pressure distributions at various Mach numbers for the five configurations tested. Generally, for the subsonic Mach numbers at which there is no separation on a given afterbody, the greatest relative changes occur when going from jet off to jet on $\left(p_{t,j}/p_\infty \approx 2\right)$. Increases in jet total-pressure ratio have a much smaller effect (at least in the range of pressure ratios tested) than does going from jet off to jet on. However, when a shock (shock-induced separation) is present on the afterbody, either at subsonic or supersonic speeds, the data indicate that this effect may change (see, for example, fig. 15(c)); that is, the increase in pressure ratio (from jet on to maximum) can move the shock forward to such an extent that the resulting effect is larger than that produced by turning the jet on.

Comparison of measured pressure distributions with theoretical predictions.- Figure 20 presents jet-on $\left(p_{t,j}/p_\infty \approx 2\right)$ pressure distributions for all five configurations at two representative subsonic Mach numbers (0.4 and 0.8) compared with theoretical predictions, from the theory of reference 13, using a circular cylinder to simulate the jet shape. (This theory includes a correction for compressibility effects but does not include any correction for viscous effects.) It was believed that this theoretical method would give results typical of the present-day state of the art in theoretical pressure-distribution

prediction; it was also believed that using a circular cylinder to simulate the jet shape would be typical of the type of simulation used when trying to use theory to predict the jet-on pressure distribution for a nozzle operating on design. For most conditions, the theory predicts the minimum pressure coefficient and the general shape of the distributions quite well. However, this prediction method breaks down near the end of the boattail where the theory forces the flow toward a stagnation point; as a result, all predicted pressures are too high.

Effects of jet operation on boattail pressure drag.- Figures 21 to 24 present the effects of jet total-pressure ratio on the boattail pressure drag of the five configurations tested, plus the configuration from reference 4. The effects for the two configurations with $d_e/d_m = 0.6$, the three configurations with $d_e/d_m = 0.7$, the three configurations with $l/d_m = 1.0$, and the two configurations with $l/d_m = 1.5$ are shown in figures 21, 22, 23, and 24, respectively. Flagged symbols indicate repeat prints.

The data of figures 21 and 22 indicate two main results. First, the data support the conclusion, drawn from figures 15 to 19, that increasing the jet total-pressure ratio has a relatively smaller effect on boattail pressure drag than does going from jet off to jet on at most subsonic speeds. Second, the data show that increasing fineness ratio for a given closure ratio results in a decrease in boattail pressure drag for all pressure ratios and that this effect increases with increasing Mach number at subsonic speeds but stays about constant at supersonic speeds.

Similar trends for increasing closure ratio are shown in figures 23 and 24. As closure ratio increased for both values of fineness ratio (1.0 and 1.5), the boattail pressure drag decreased. This effect increased with increasing Mach number at subsonic speeds while it remained relatively constant at supersonic speeds. This was true for jet-on pressure ratios for all the configurations (contrary to the previously shown jet-off results for the configuration of ref. 4). Also, these data further support the conclusion that the greatest change in boattail pressure drag occurs when going from jet off to jet on (at most subsonic speeds). A discussion of this phenomenon can be found in reference 14.

Figure 25 is a typical turbofan-engine pressure-ratio variation with Mach number at which the drag data are to be cross plotted. The pressure-ratio schedule assumes that the core and fan flows are mixed in a common nozzle.

Figure 26 is a cross plot of boattail pressure drag versus Mach number for the five configurations at the schedule of figure 25. At subsonic speeds before the drag rise and, again, at supersonic speeds, the two configurations with $d_e/d_m = 0.6$ have higher drag than do the three configurations with $d_e/d_m = 0.7$ and, within the groups of constant closure ratio, the lower fineness ratio gives the higher drag. The only points where this effect does not occur are above a Mach number of about 0.93, at which point the drag

curves of configuration 2 $\left(d_e/d_m = 0.6;\ \ell/d_m = 1.5\right)$ and configuration 3 $\left(d_e/d_m = 0.7;\ \ell/d_m = 1.0\right)$ cross over because of the fact that configuration 3 has a lower jet-on drag-rise Mach number than does configuration 2.

Boattail total drag (pressure plus calculated skin friction) is cross plotted in figure 27. The main conclusion to be drawn from this figure is that, at subsonic speeds before the drag rise, the drag levels of the two configurations with $d_e/d_m = 0.6$ are nearly the same – also true for the three configurations with $d_e/d_m = 0.7$ which have lower drag than the configurations with $d_e/d_m = 0.6$. This conclusion is not readily apparent from the figure because of the staggered scale which was necessary to show the drag-rise characteristics. As stated before, the higher fineness ratio for a given closure ratio gave the higher drag-rise Mach number. At supersonic speeds, although all the configurations are clustered together on the figure because of the staggered scale, the relative positions are the same as for the pressure-drag data shown in figure 26.

Angle-of-Attack Effects

Figures 28 to 31 present boattail axial-force coefficients based on all pressure orifices (see appendix) as a function of jet total-pressure ratio for the various angles of attack and Mach numbers tested for configurations 2, 3, 4, and 5. Data for configuration 1 are not presented due to unacceptable strut interference effects on the lower surface (see appendix). All the data indicate that boattail axial force generally tends to increase with angle-of-attack variation for all configurations.

Boattail drag coefficients for configurations 2, 3, 4, and 5 at various Mach numbers and angles of attack are presented in figures 32 to 35. Again, these coefficients are based on all pressure orifices, and data for configuration 1 are not shown because of the strut interference effects. The effect of angle of attack on boattail drag was generally slightly larger in magnitude and opposite in sign to the effect on boattail axial force. This phenomenon occurred because a negative normal force was produced on the boattails at positive angles of attack (and positive normal force at negative angles of attack) and this normal force contributed a negative term to the drag equation (see section entitled "Data Reduction") – hence the drag was lower than that at an angle of attack of 0°. Plots of normal-force coefficient as a function of angle of attack for all the configurations at a jet total-pressure ratio of about 2 for two typical Mach numbers are shown in figure 36. Figure 37 is a cross plot of boattail drag coefficient versus Mach number for the four configurations at the four angles of attack and the pressure-ratio schedule of figure 25. The difference between data for $\alpha = 4^\circ$ and $\alpha = -4^\circ$ is unexplainable at the present time.

Force Data

Internal performance.- Wind-off (static) thrust-ratio data for the five configurations are shown in figure 38, with two runs plotted to show repeatability. All of the nozzles have an acceptably high level of performance. The sometimes poor repeatability below a pressure ratio of about 1.5 may be due to the fact that the balance and other measuring devices were sized for the maximum anticipated conditions and that at these low pressure ratios the relative accuracy suffers as a result.

Figure 39 presents the static discharge coefficients for all five configurations. As with the thrust-ratio performance all the nozzles have discharge coefficients which are of acceptably high level, and the same comment concerning repeatability at low pressure ratios applies.

Wind-on thrust ratios (i.e., thrust minus drag to which nozzle pressure and friction drag have been added) are presented in figure 40 for configurations 1 and 2 $\left(d_e/d_m = 0.6\right)$. When these data are compared with the static data (fig. 38) for the same configurations, the results indicate that within the accuracy of the measurements (about ± 0.5 percent) there seems to be little, if any, effect of the external stream on the internal performance for these two nozzles which have long internal throats. Similar results for configurations 3 and 4 $\left(d_e/d_m = 0.7;\ l/d_m = 1.0 \text{ and } 1.5, \text{ respectively}\right)$ are shown in figure 41. Wind-on data for configuration 5 are not presented because of an unexplainable systematic error in the balance measurement.

Thrust minus drag.- Presented in figure 42 are data of thrust minus drag ratioed to ideal thrust at various Mach numbers for configurations 1 and 2 $\left(d_e/d_m = 0.6;\ l/d_m = 1.0 \text{ and } 1.5, \text{ respectively}\right)$. The trend shown by these data correlates well with that shown by the combination of pressure and friction drag from figure 27. At the lower subsonic Mach numbers, the thrust-minus-drag performance of both nozzles is approximately the same; whereas at the higher subsonic Mach numbers (after the lower-fineness-ratio afterbody has reached its drag rise), the higher-fineness-ratio afterbody exhibits better thrust-minus-drag performance and the difference between the performance of the two configurations increases with Mach number.

Figure 43 presents the corresponding thrust-minus-drag results for configurations 3 and 4 $\left(d_e/d_m = 0.7;\ l/d_m = 1.0 \text{ and } 1.5, \text{ respectively}\right)$. The trend shown by these data also correlates well with the trend of data from figure 27. The performance of both configurations is about the same until the drag-rise Mach number of the shorter one (configuration 3) is reached, at which point the higher-fineness-ratio configuration gains an advantage which then increases with increasing Mach number.

Values of F_i/qA_m are plotted in figure 44 as a function of jet total-pressure ratio for the two exit areas investigated at various Mach numbers. These plots can be used to convert from aerodynamic coefficients based on qA_m to propulsion coefficients based on F_i.

CONCLUSIONS

An investigation was conducted in the Langley 16-foot transonic tunnel to determine the effects of variation in fineness ratio and closure ratio on the boattail drag of circular-arc afterbodies at Mach numbers to 1.30.

The results of this investigation indicate the following (all refer to 0° angle of attack except conclusion 5):

1. For a fixed value of closure ratio d_e/d_m (ratio of exit diameter to model maximum diameter), the configuration with the lowest fineness ratio l/d_m (ratio of afterbody length to model maximum diameter) had the lowest negative pressures in the expansion region of the boattail and, if the flow has not separated, the highest positive pressures in the recompression region of the boattail.

2. For all configurations at most subsonic Mach numbers, going from jet off to jet on generally increased boattail pressures and decreased pressure drag more than did further increases in pressure ratio for the range of pressure ratios tested.

3. For a fixed value of closure ratio, increasing fineness ratio resulted in decreased pressure drag and increased drag-rise Mach number. For a fixed value of fineness ratio, increasing closure ratio resulted in decreased pressure drag and increased drag-rise Mach number.

4. When calculated friction drag has been added to pressure drag and the drag has been compared at a typical operating pressure-ratio schedule, the two configurations with $d_e/d_m = 0.6$ and $l/d_m = 1.0$ and 1.5 had approximately the same drag at subsonic speeds before the drag rise. The three configurations with $d_e/d_m = 0.7$ and $l/d_m = 1.0$, 1.5, and 2.0 exhibited the same characteristic except that the drag level was lower.

5. For all configurations, boattail pressure axial force generally increased with angle of attack whereas boattail pressure drag generally decreased.

Langley Research Center,
National Aeronautics and Space Administration,
Hampton, Va., February 12, 1973.

APPENDIX

STRUT INTERFERENCE ON BOATTAIL PRESSURES

Figures 45 to 50 treat the problem of sting-strut interference on the measured boattail pressures. In the investigation of reference 4 large effects of the sting-strut support were observed on some of the configurations with the highest boattail angles (especially at jet-off conditions). As a result, a study was made to determine the possible effects of the sting-strut on the boattail pressures for the configurations of the present investigation.

Jet-off longitudinal pressure distributions are shown in figure 45 for three stations on the circumference of configurations 1 and 2 at four representative Mach numbers. There is a relatively large effect of the sting-strut on several of the pressures in the longitudinal row at the 180° station (row directly behind strut) of configuration 1 at a Mach number of 0.96, and there is some slight effect at the other two subsonic Mach numbers for this configuration. There are also some slight effects shown at the two highest subsonic Mach numbers for configuration 2. Neither configuration was affected at supersonic speeds.

Similar data for configurations 3, 4, and 5 $\left(d_e/d_m = 0.7\right)$ are shown in figure 46. Of these, only configuration 3 $\left(l/d_m = 1.0\right)$ shows any effect of interference and that only at a Mach number of 0.96. As for the configurations with $d_e/d_m = 0.6$ there was no apparent effect at the supersonic Mach number.

In order to further investigate the phenomenon at subsonic speeds, all measured boattail pressures were plotted in figure 47 as a function of circumferential angle for all jet-off configurations at Mach numbers of 0.80 and 0.96. From these and the previous data it appears as if the disturbance from the sting-strut primarily affects the pressures at the beginning of the recompression region ($x/l \approx 0.5$) on the lower surface of the boattail; the higher the boattail angle, or the higher the subsonic Mach number, the greater the effect.

In reference 4 it was found that jet operation significantly reduced the interference. In order to investigate this effect for the afterbodies of the present study, figure 48 was made to show all the measured pressures from figure 47 but at a jet total-pressure ratio of about 4. These data show the same result as that found in reference 4, that is, the jet reduces the effect of the interference.

The effect of the interference on boattail drag is shown in figures 49 and 50. Figure 49 shows the jet-off drag variation with Mach number for the five configurations with the pressure integrations based on all orifices and on the top row (0°) of orifices only (found to be interference free in refs. 1 and 4). Corresponding to the results of figures 45 and 47, the data for configuration 1 exhibit a difference between the drag cal-

culated by the two methods at the higher subsonic Mach numbers. As mentioned before, all the data presented at $\alpha = 0^{o}$ have been based on the integration of the top row of pressures only. In order to determine the effect of the jet on boattail drag, figure 50 was prepared to show drag, calculated by both methods, as a function of jet total-pressure ratio for various Mach numbers for configuration 1. The jet-on drag data is the same for all Mach numbers. The results were similar for the other configurations; that is, the jet operation effectively eliminated the strut interference and either integration method was equally valid for jet-on data.

Although data at $\alpha = 0^{o}$ can be computed by utilizing the interference-free top row of orifices only, angle-of-attack data require the use of all orifices to obtain valid results. In order to determine the magnitude of possible strut interference effects on the angle-of-attack data of the present investigation, an investigation (data unpublished) of these afterbodies was made utilizing both the sting-strut support and a rear sting support. In both cases a solid circular cylinder was used to simulate the on-design jet shape and provide identical configurations for comparison purposes. When the data from the interference-free sting-alone configurations were compared with the data from the sting-strut mounted configurations, it was found that both $C_{A,\beta}$ and $C_{D,\beta}$ can be, at most, in error by 0.005 for configurations 2 and 3 and by 0.003 for configurations 4 and 5. These unpublished data also indicate that the possible errors in data for configuration 1 are such that angle-of-attack data for this configuration are possibly unreliable and, hence, are not reported herein.

REFERENCES

1. Compton, William B., III; and Runckel, Jack F.: Jet Effects on the Boattail Axial Force of Conical Afterbodies at Subsonic and Transonic Speeds. NASA TM X-1960, 1970.

2. Compton, William B., III: Jet Effects on the Drag of Conical Afterbodies at Supersonic Speeds. NASA TN D-6789, 1972.

3. Harrington, Douglas E.: Jet Effects on Boattail Pressure Drag of Isolated Ejector Nozzles at Mach Numbers From 0.60 to 1.47. NASA TM X-1785, 1969.

4. Reubush, David E.; and Runckel, Jack F.: Effect of Fineness Ratio on the Boattail Drag of Circular-Arc Afterbodies Having Closure Ratios of 0.50 With Jet Exhaust at Mach Numbers up to 1.30. NASA TN D-7192, 1973.

5. Shrewsbury, George D.: Effect of Boattail Juncture Shape on Pressure Drag Coefficients of Isolated Afterbodies. NASA TM X-1517, 1968.

6. Swihart, John M.; Mercer, Charles E.; and Norton, Harry T., Jr.: Effect of Afterbody-Ejector Configurations on the Performance at Transonic Speeds of a Pylon-Supported Nacelle Model Having a Hot-Jet Exhaust. NASA TN D-1399, 1962.

7. Lee, Edwin E., Jr.; and Runckel, Jack F.: Performance of Closely Spaced Twin-Jet Afterbodies With Different Inboard-Outboard Fairing and Nozzle Shapes. NASA TM X-2329, 1971.

8. Maiden, Donald L.; and Runckel, Jack F.: Effect of Nozzle Lateral Spacing on Afterbody Drag and Performance of Twin-Jet Afterbody Models With Convergent Nozzles at Mach Numbers up to 2.2. NASA TM X-2099, 1970.

9. Ward, Vernon G.; Whitcomb, Charles F.; and Pearson, Merwin D.: Air-Flow and Power Characteristics of the Langley 16-Foot Transonic Tunnel With Slotted Test Section. NACA RM L52E01, 1952.

10. Schaefer, William T., Jr.: Characteristics of Major Active Wind Tunnels at the Langley Research Center. NASA TM X-1130, 1965.

11. Braslow, Albert L.; and Knox, Eugene C.: Simplified Method for Determination of Critical Height of Distributed Roughness Particles for Boundary-Layer Transition at Mach Numbers From 0 to 5. NACA TN 4363, 1958.

12. Braslow, Albert L.; Hicks, Raymond M.; and Harris, Roy V., Jr.: Use of Grit-Type Boundary-Layer Transition Trips on Wind-Tunnel Models. NASA TN D-3579, 1966.

13. Hess, J. L.; and Smith, A. M. O.: Calculation of Potential Flow About Arbitrary Bodies. Progress in Aeronautical Sciences, Vol. 8, D. Kuchemann, ed., Pergamon Press, Ltd., c.1967, pp. 1-138.

14. Bergman, Dave: Exhaust Nozzle Drag: Engine vs. Airplane Force Model. AIAA Paper No. 70-668, June 1970.

TABLE I.- AFTERBODY-SURFACE ORIFICE LOCATIONS

x/l	x/d_m	ϕ, deg									
		0	30	60	90	120	135	150	180	225	315
Configuration 1											
0	0	x	x	x	x	x		x	x	x	x
.2365	.2365	x	x	x	x	x		x	x		
.4133	.4133	x	x	x	x	x		x	x		
.5388	.5388	x	x	x	x	x		x	x	x	x
.6443	.6443	x	x	x	x	x		x	x		
.7392	.7392	x	x	x	x	x		x	x		
.8278	.8278	x	x	x	x	x		x	x	x	x
.9130	.9130	x	x	x	x	x		x	x		
.9667	.9667	x	x	x	x	x		x	x		
Configuration 2											
0	0	x	x	x	x		x		x	x	x
.2342	.3513	x	x	x	x		x		x		
.4098	.6147	x	x	x	x		x		x		
.5349	.8023	x	x	x	x		x		x	x	x
.6404	.9607	x	x	x	x		x		x		
.7357	1.1035	x	x	x	x		x		x		
.8250	1.2375	x	x	x	x		x		x	x	x
.9113	1.3670	x	x	x	x		x		x		
.9722	1.4583	x	x	x	x		x		x		
Configuration 3											
0	0	x	x	x	x		x		x	x	x
.2720	.2720	x	x	x	x		x		x		
.4758	.4758	x	x	x	x		x		x		
.6205	.6205	x	x	x	x		x		x	x	x
.7425	.7425	x	x	x	x		x		x		
.8523	.8523	x	x	x	x		x		x		
.9550	.9550	x	x	x	x		x		x	x	x
Configuration 4											
0	0	x	x	x	x		x		x	x	x
.2706	.4058	x	x	x	x		x		x		
.4737	.7105	x	x	x	x		x		x		
.6183	.9275	x	x	x	x		x		x	x	x
.7406	1.1108	x	x	x	x		x		x		
.8509	1.2763	x	x	x	x		x		x		
.9546	1.4318	x	x	x	x		x		x	x	x
Configuration 5											
0	0	x	x	x	x		x		x	x	x
.2701	.5402	x	x	x	x		x		x		
.4729	.9458	x	x	x	x		x		x		
.6176	1.2352	x	x	x	x		x		x	x	x
.7399	1.4798	x	x	x	x		x		x		
.8504	1.7008	x	x	x	x		x		x		
.9544	1.9088	x	x	x	x		x		x	x	x

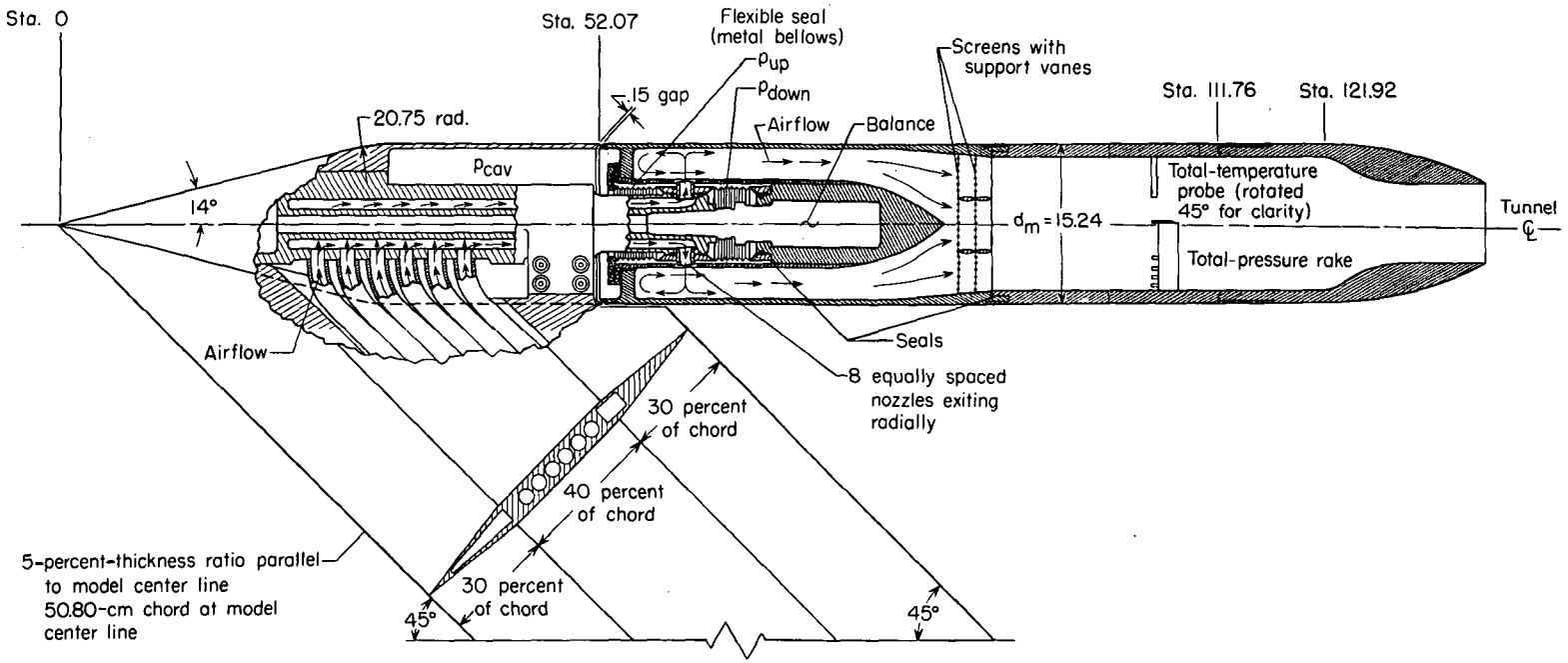
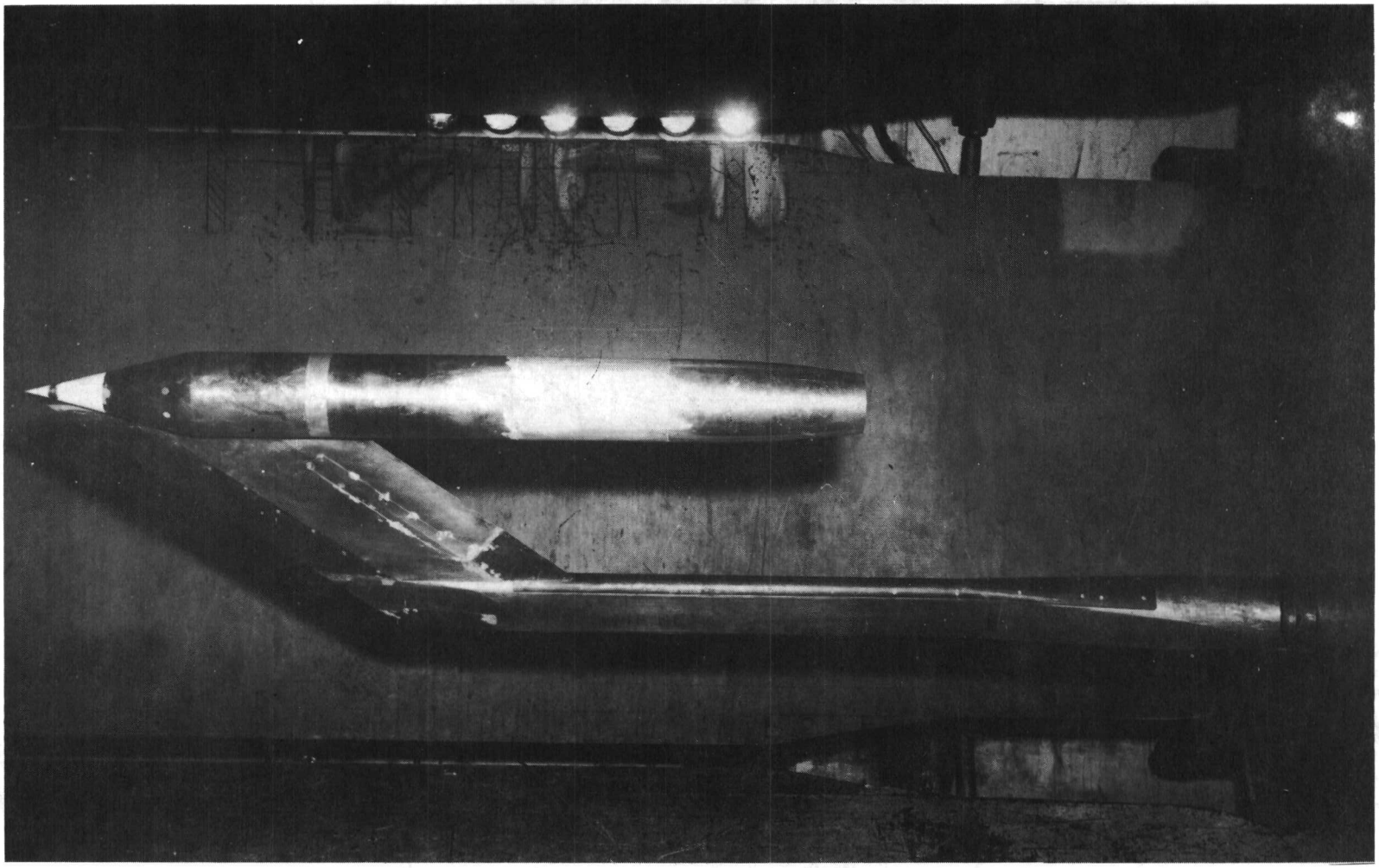


Figure 1.- Sketch of air-powered cone-cylinder model with a typical circular-arc convergent nozzle installed. All dimensions are in centimeters unless otherwise noted.



L-72-1872

Figure 2.- Model, with configuration 5 attached, installed in the Langley 16-foot transonic tunnel.

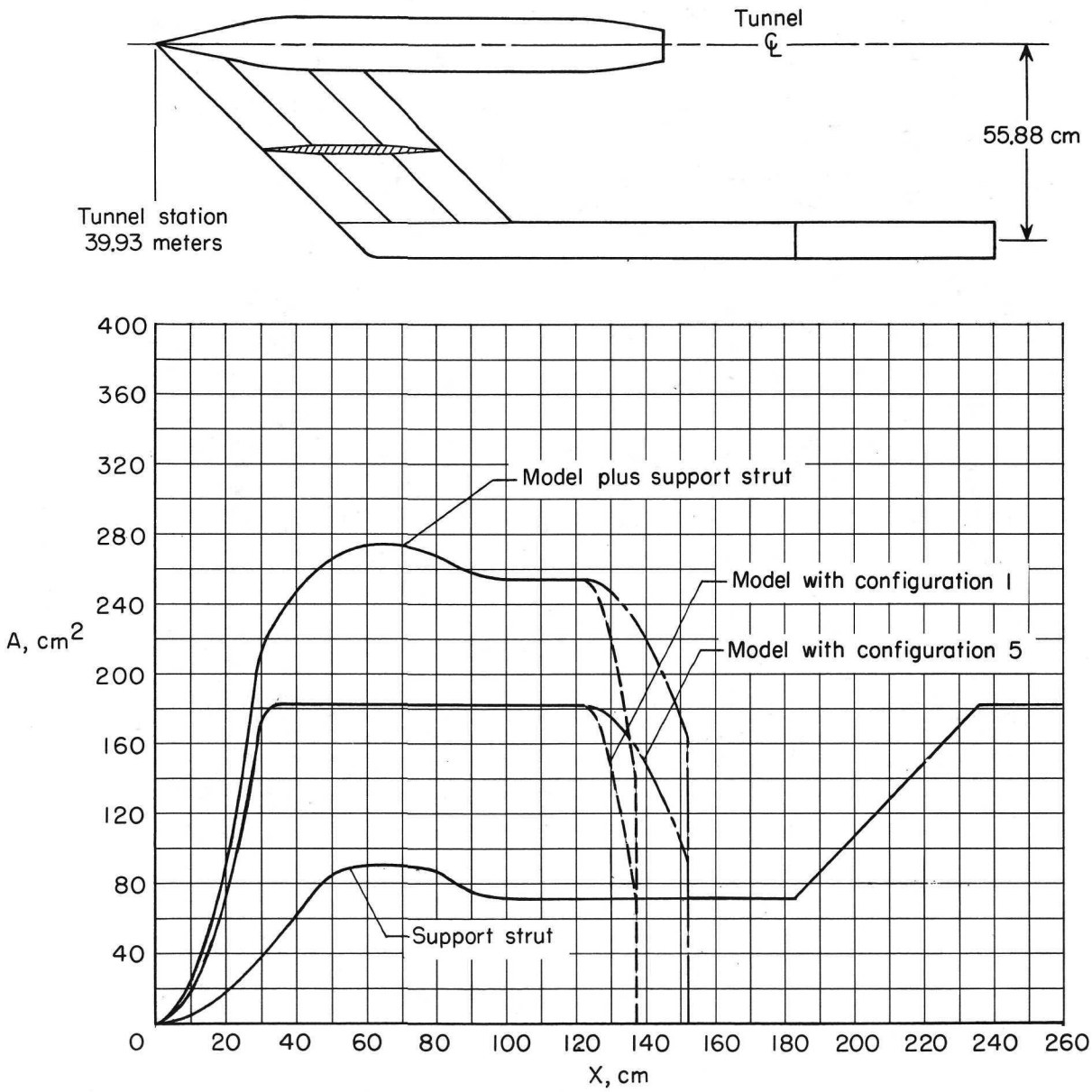
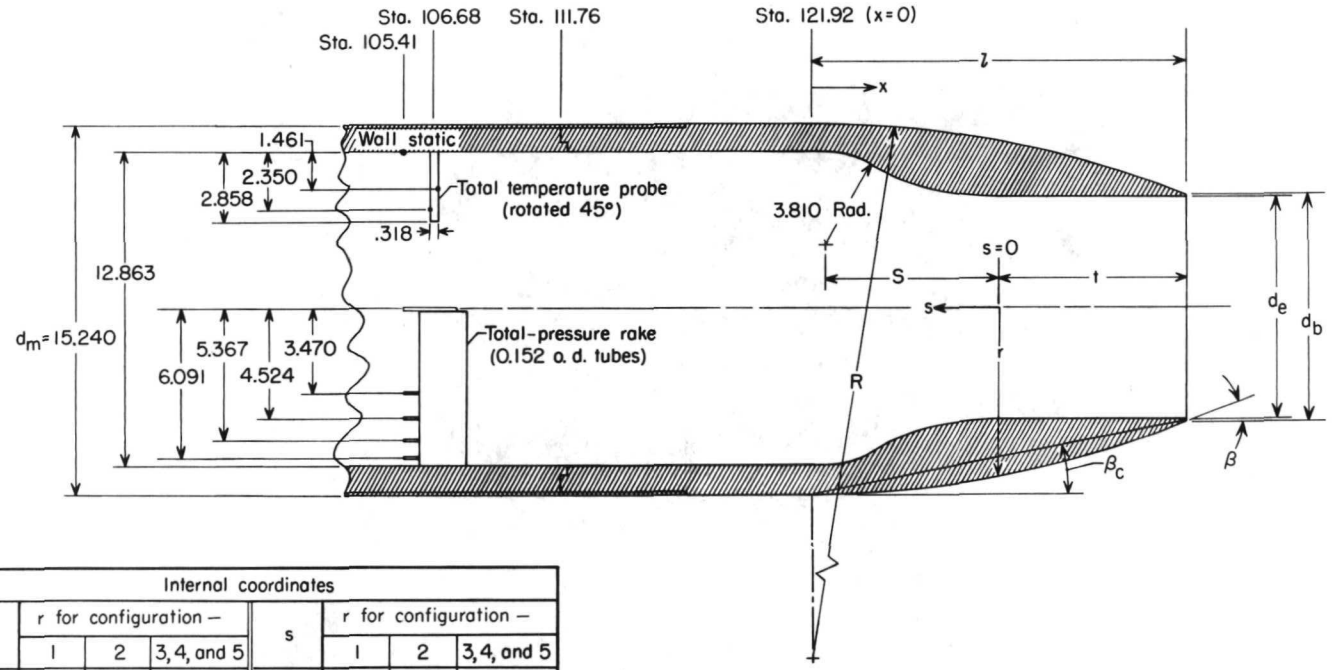


Figure 3.- Cross-sectional area distributions of support system and model.



Internal coordinates							
s	r for configuration —			s	r for configuration —		
	1	2	3, 4, and 5		1	2	3, 4, and 5
0	4.572	4.572	5.334	4.318	5.458	5.052	5.618
.254	4.575	4.575	5.337	4.445	5.517	——	——
.508	4.582	4.577	5.339	4.572	5.578	5.123	5.659
.762	4.597	4.585	5.342	4.699	5.644	——	——
1.016	4.618	4.595	5.349	4.826	5.710	5.202	5.705
1.270	4.643	4.608	5.357	4.953	5.781	5.245	——
1.524	4.674	4.625	5.364	5.080	5.852	5.291	5.758
1.778	4.712	4.646	5.377	5.207	5.931	5.339	5.786
2.032	4.755	4.669	5.390	5.334	6.010	5.392	5.819
2.286	4.803	4.694	5.405	5.461	6.096	5.448	5.852
2.540	4.859	4.722	5.423	5.588	6.182	5.512	5.888
2.794	4.923	4.757	5.443	5.715	6.276	5.578	5.928
3.048	4.991	4.793	5.466	5.842	6.373	5.654	5.972
3.302	5.070	4.836	5.489	5.969	6.477	5.738	6.022
3.556	5.154	4.882	5.517	6.096	6.584	5.839	6.081
3.810	5.245	4.933	5.547	6.223	6.701	5.961	6.154
3.937	5.296	——	——	6.350	6.822	6.137	6.259
4.064	5.347	4.991	5.580	6.431	——	6.431	6.431
4.191	5.403	——	——				

Geometric parameters								
Configuration	l/d_m	d_e/d_m	d_b/d_m	R/d_m	t/d_m	S/d_m	β, deg	β_c, deg
1	1.00	0.60	0.61	2.662	0.500	0.462	22.07	11.03
2	1.50	.60	.61	5.867	.592	.536	14.81	7.41
3	1.00	.70	.71	3.521	.367	.507	16.50	8.25
4	1.50	.70	.71	7.831	.667	.507	11.04	5.52
5	2.00	.70	.71	13.866	.833	.507	8.29	4.15

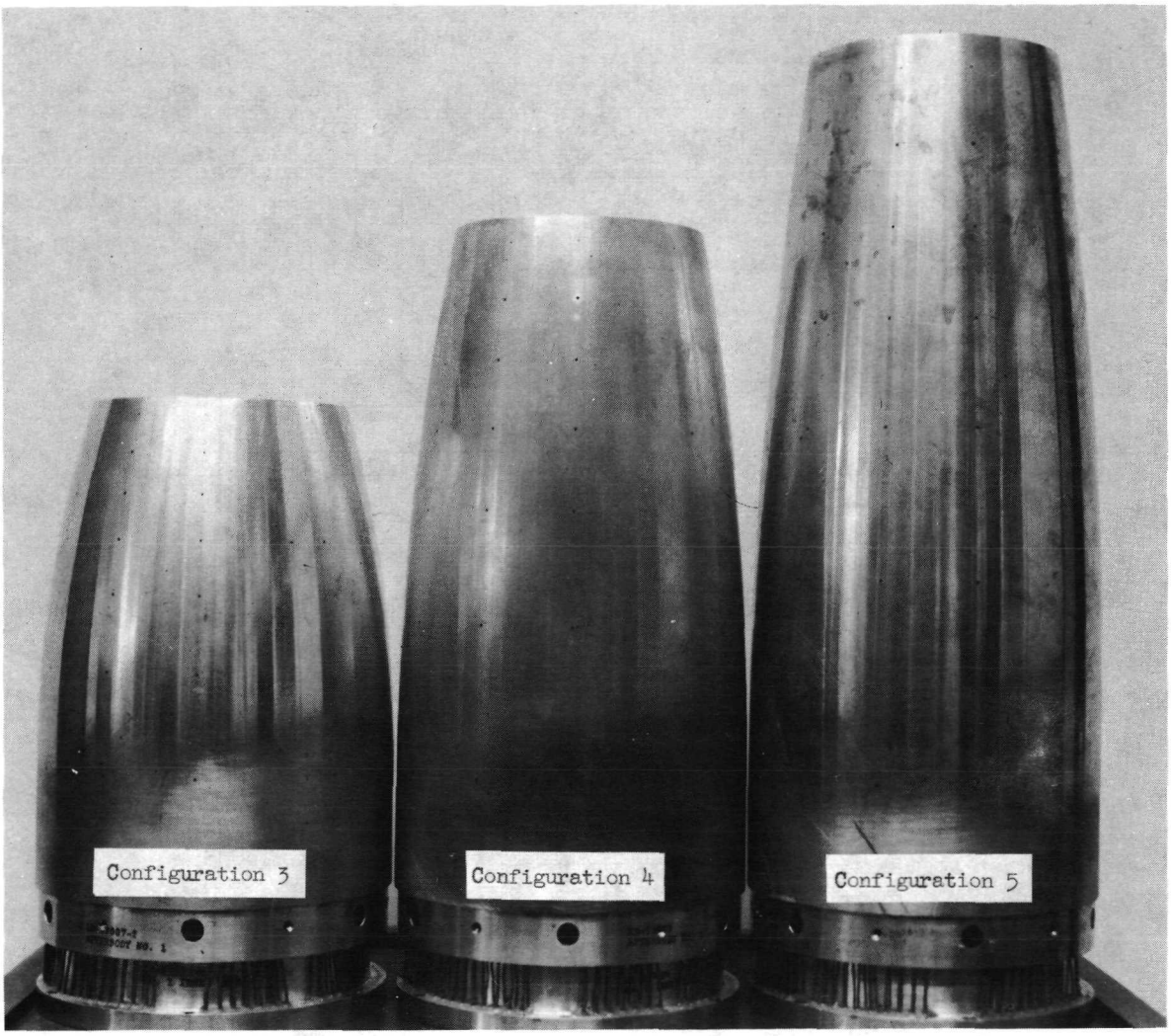
Figure 4.- Detailed sketch of typical nozzle model with tables of geometric parameters and internal coordinates. All dimensions are in centimeters unless otherwise noted.



L-72-5521

(a) Models with $d_e/d_m = 0.6$ $\left(l/d_m = 1.0 \text{ and } 1.5\right)$.

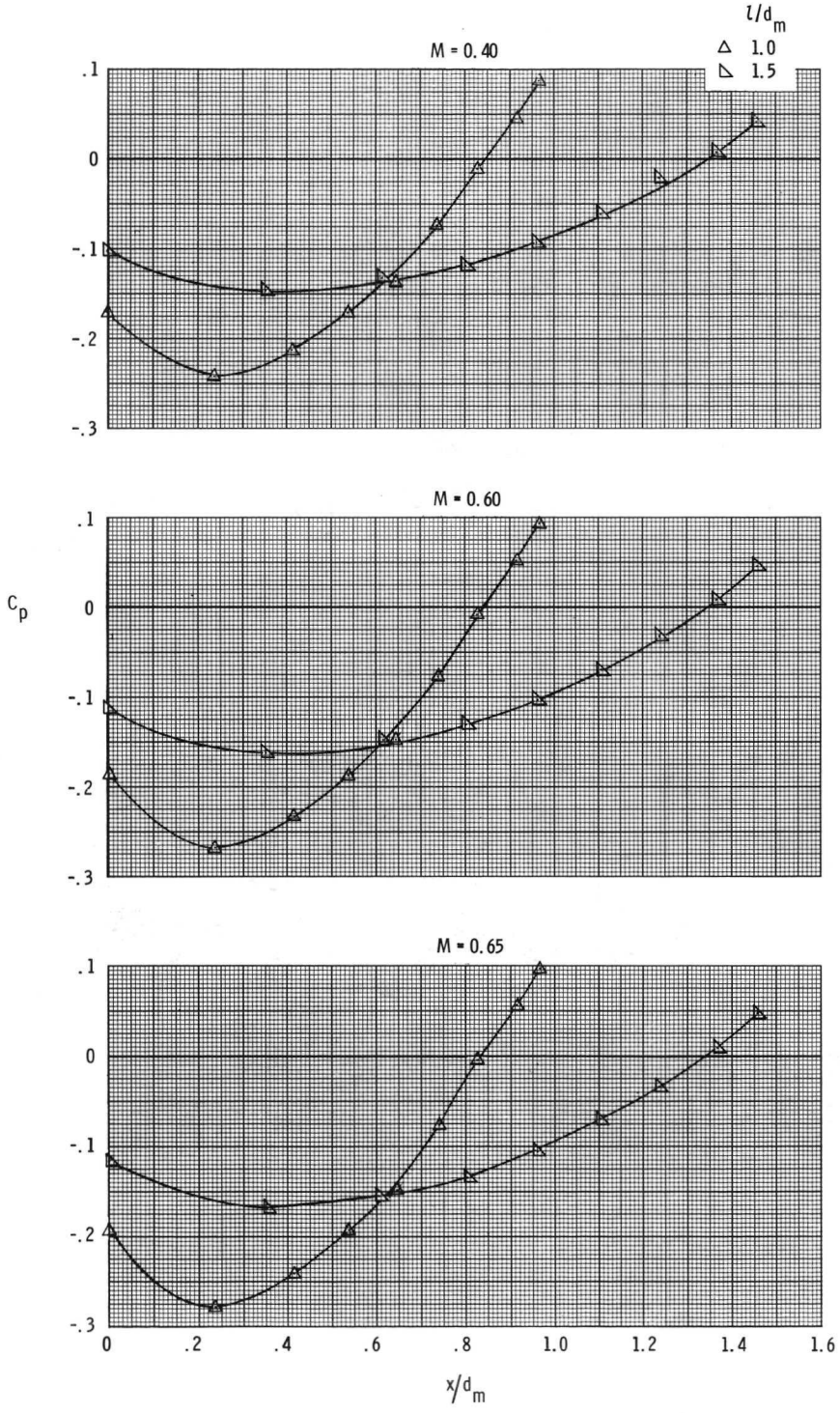
Figure 5.- Afterbody models.



L-72-5520

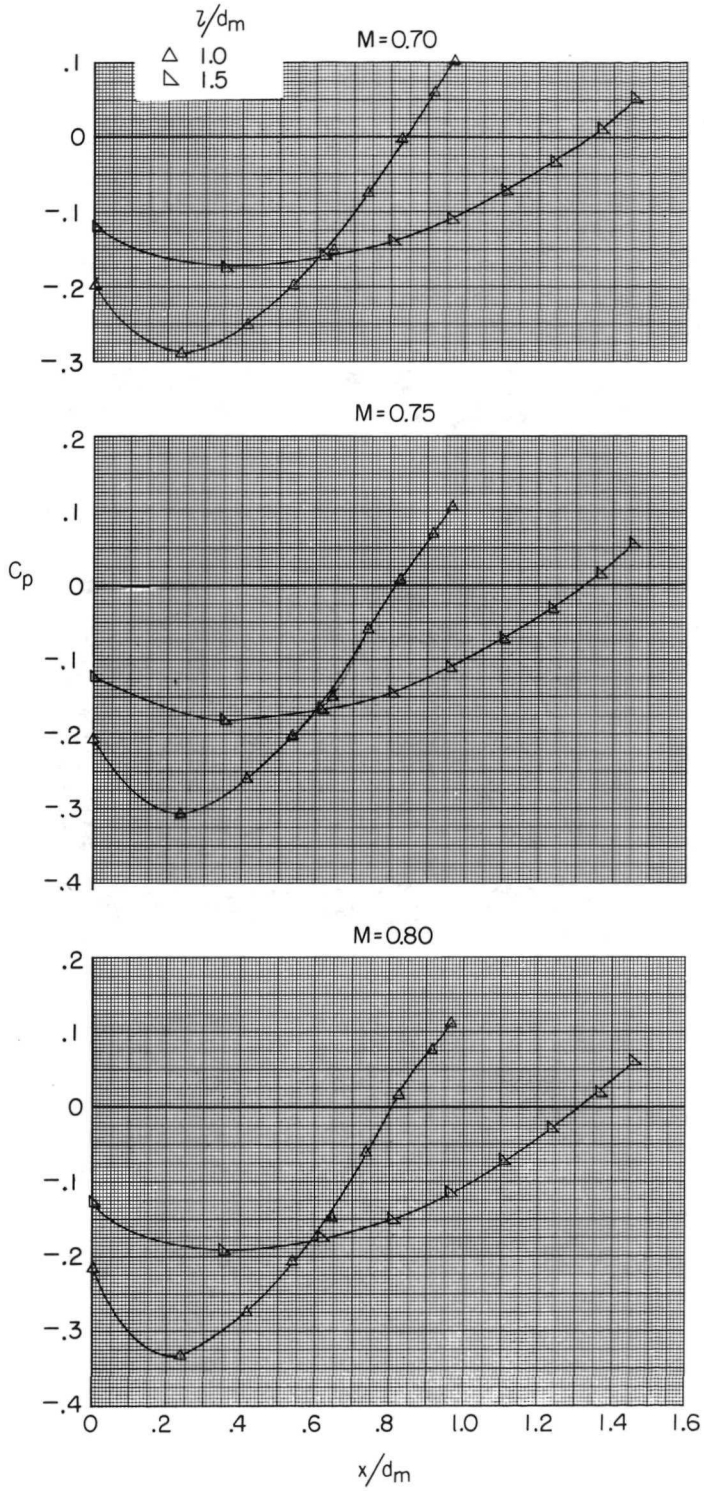
(b) Models with $d_e/d_m = 0.7$ $\left(l/d_m = 1.0, 1.5, \text{and } 2.0\right)$.

Figure 5.- Concluded.



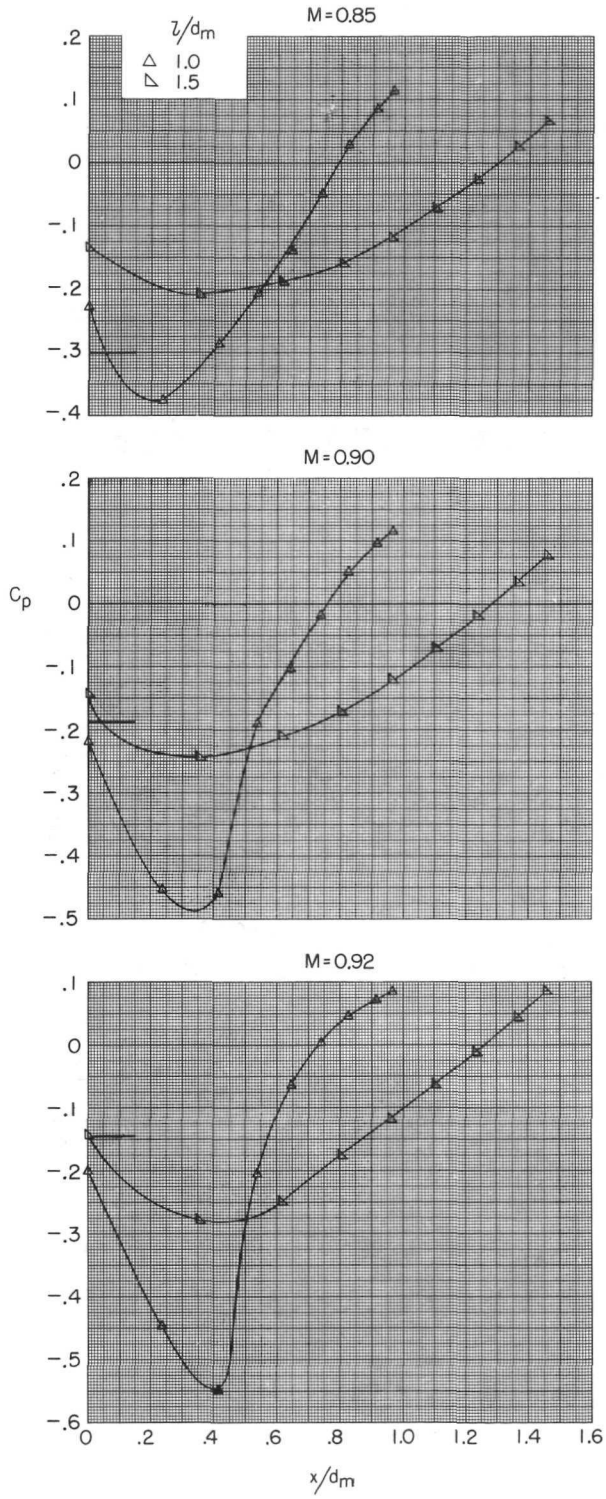
(a) M = 0.40, 0.60, and 0.65.

Figure 6.- Jet-off boattail pressure-coefficient distributions for configurations with $d_e/d_m = 0.6$ $(l/d_m = 1.0$ and $1.5)$. Tick marks indicate critical pressure coefficients.



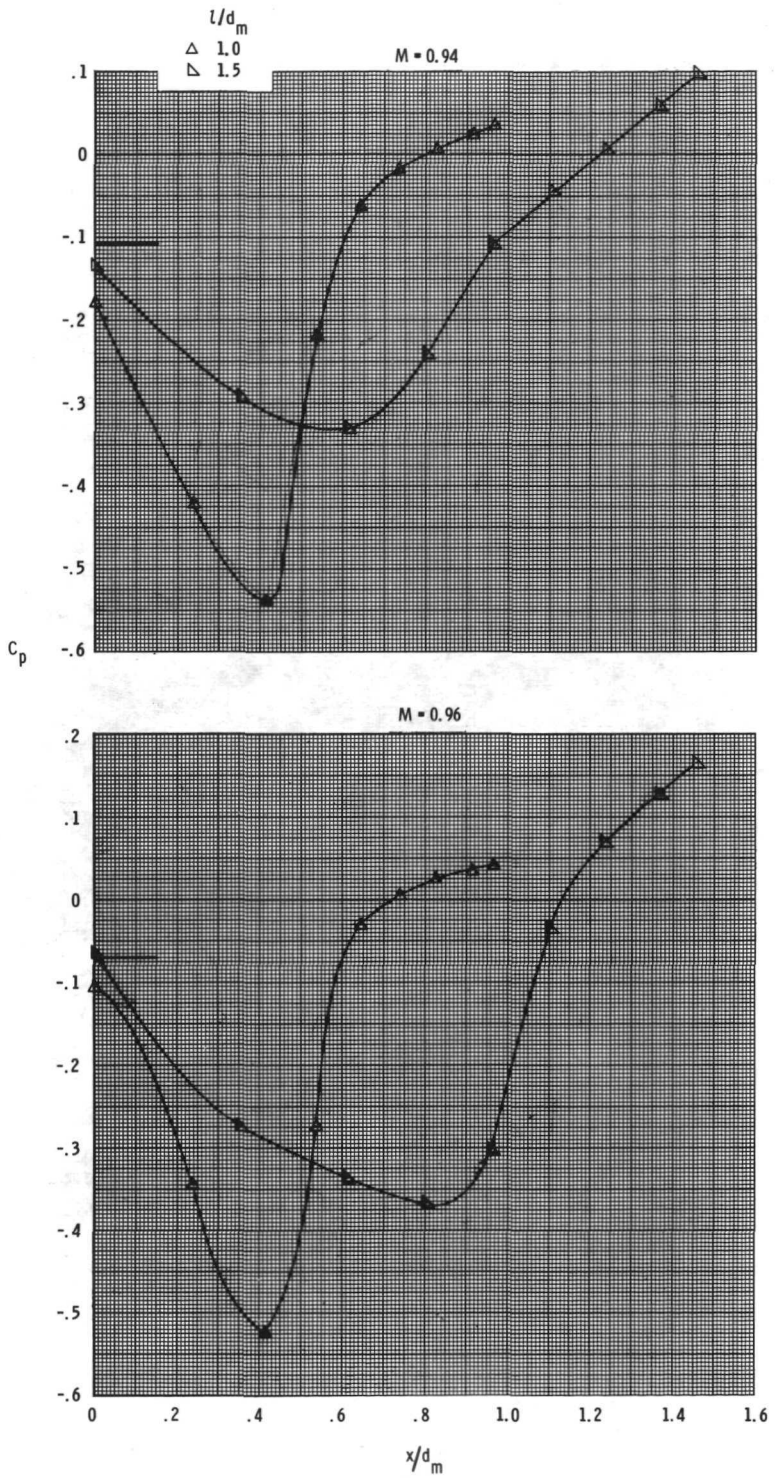
(b) M = 0.70, 0.75, and 0.80.

Figure 6.- Continued.



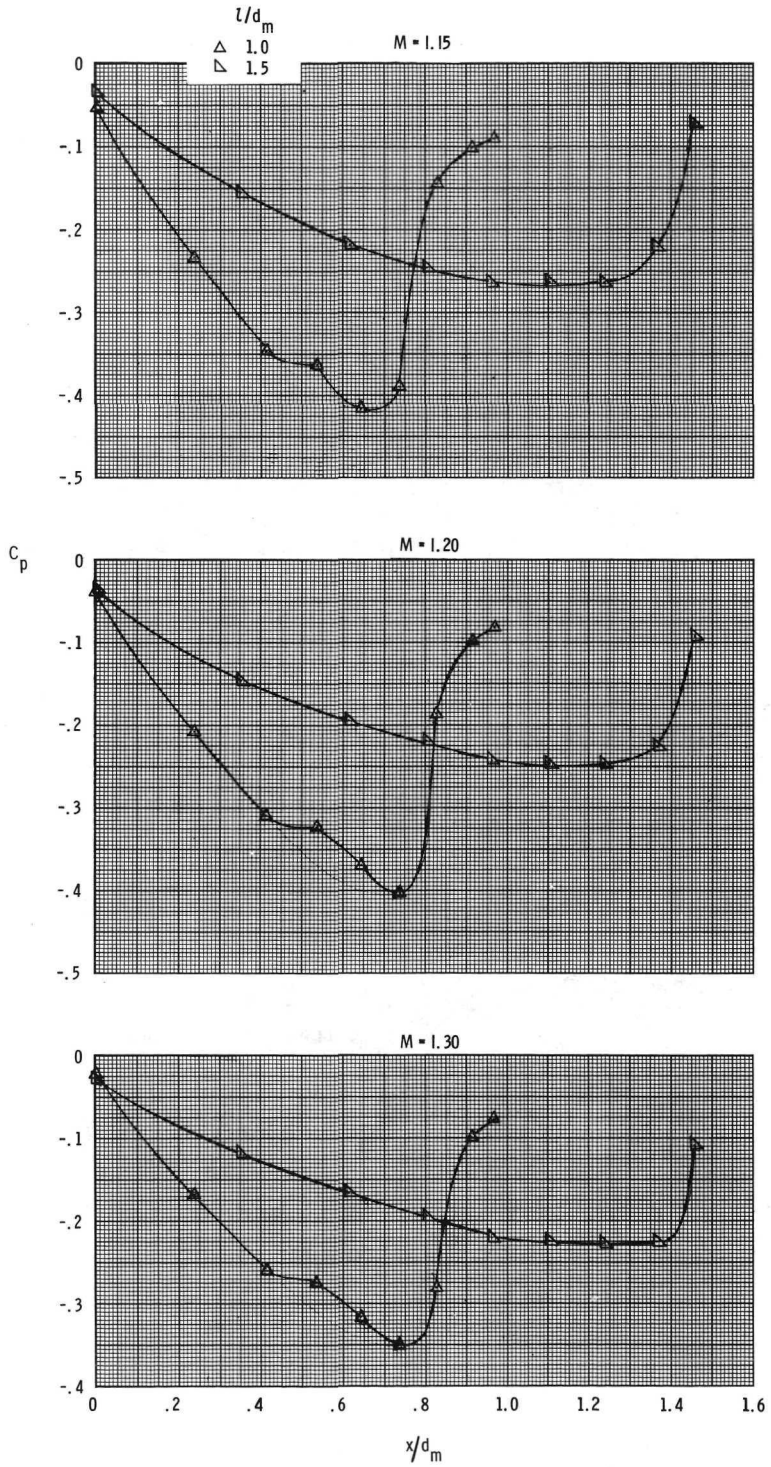
(c) M = 0.85, 0.90, and 0.92.

Figure 6.- Continued.



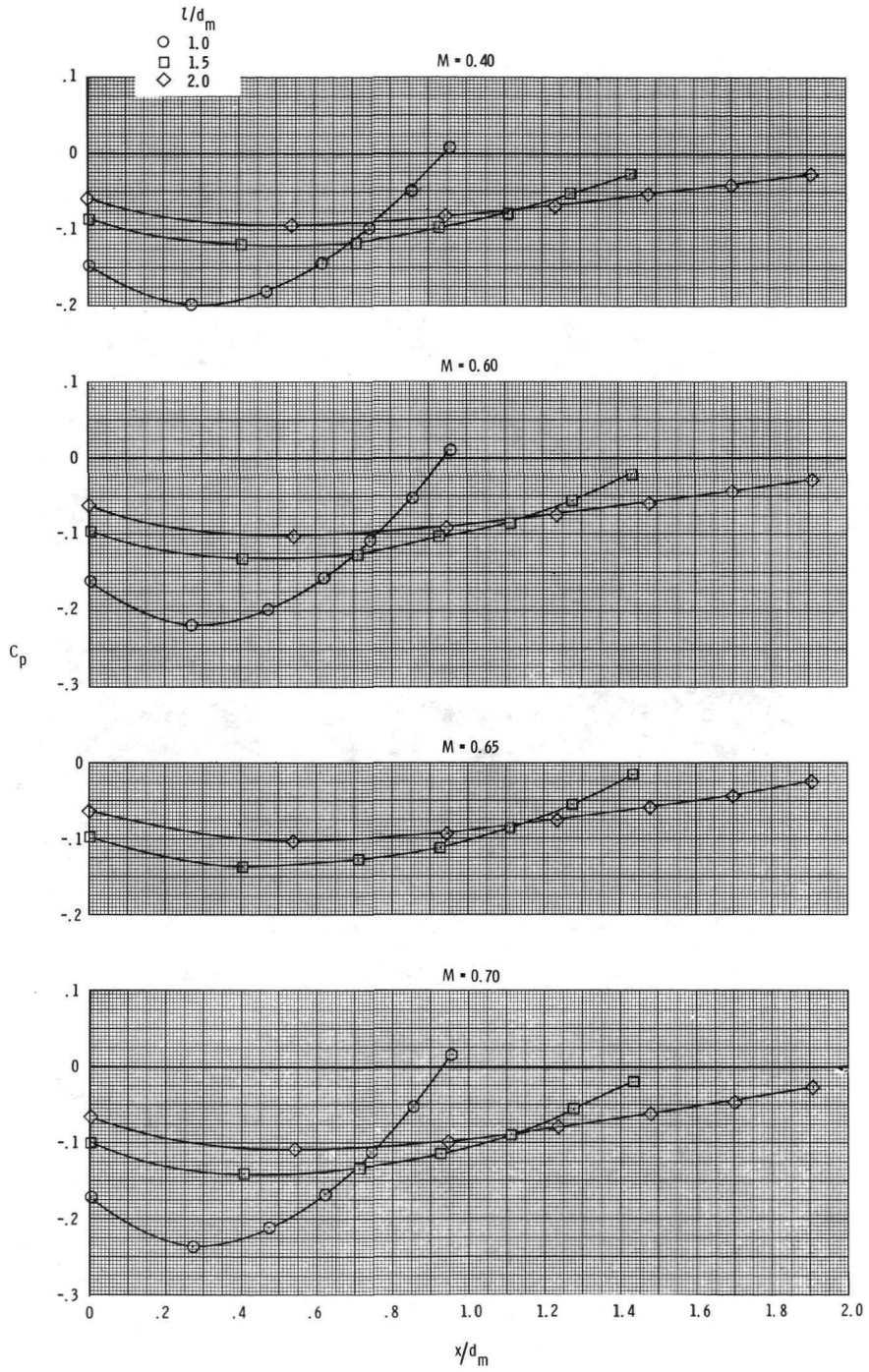
(d) M = 0.94 and 0.96.

Figure 6.- Continued.



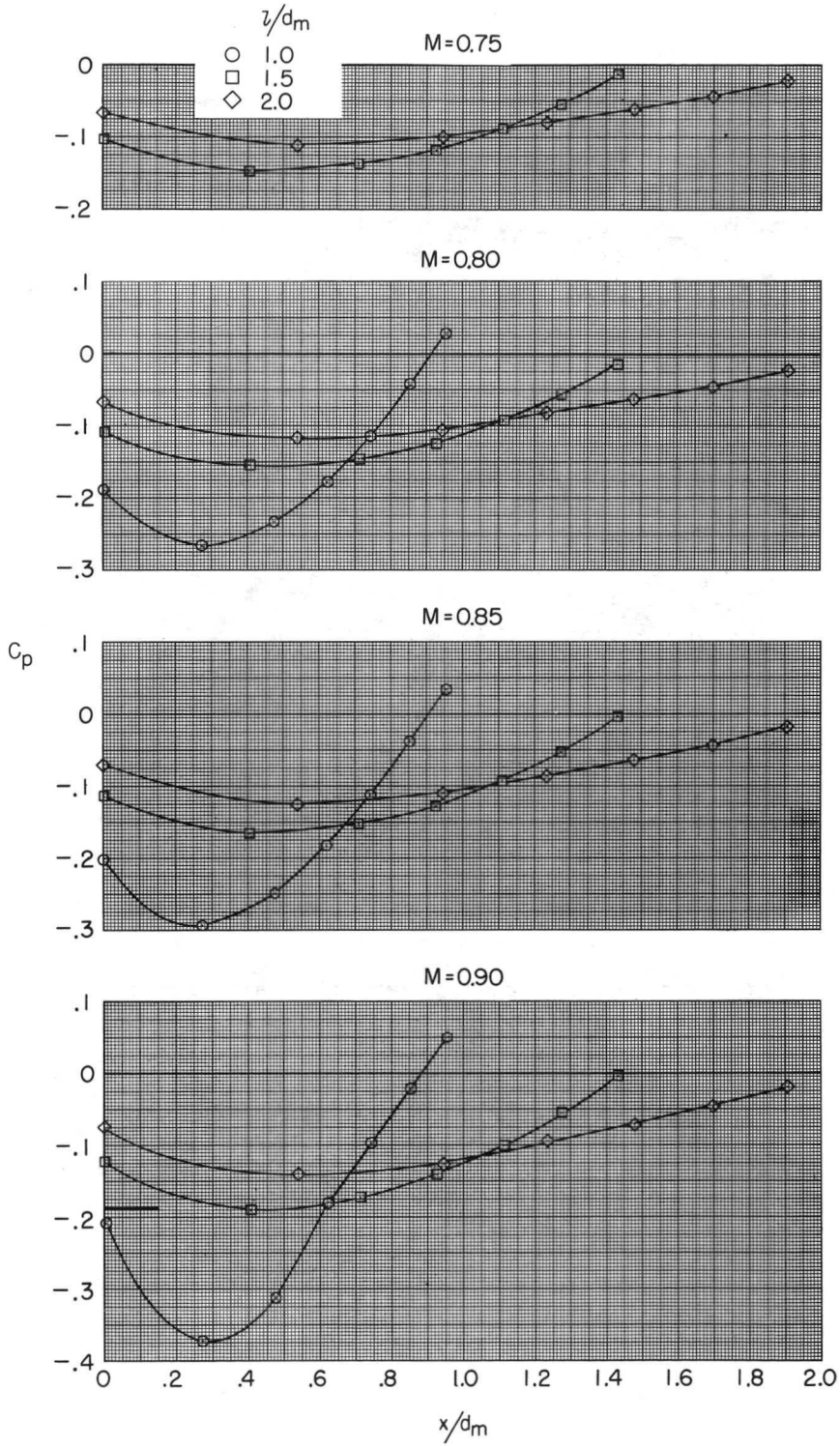
(e) M = 1.15, 1.20, and 1.30.

Figure 6.- Concluded.



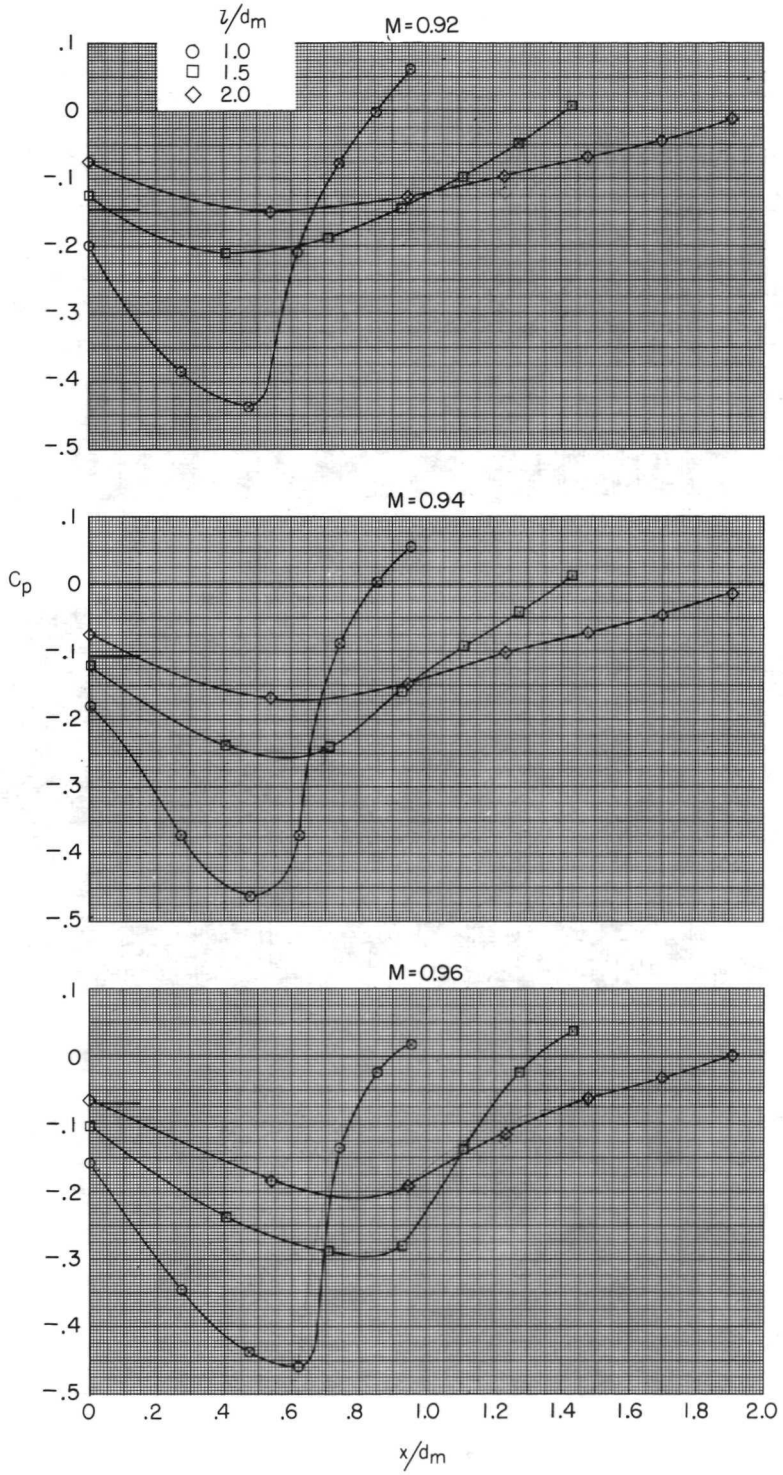
(a) M = 0.40, 0.60, 0.65, and 0.70.

Figure 7.- Jet-off boattail pressure-coefficient distributions for configurations with $d_e/d_m = 0.7$ $(l/d_m = 1.0, 1.5, \text{and } 2.0)$. Tick marks indicate critical pressure coefficients.



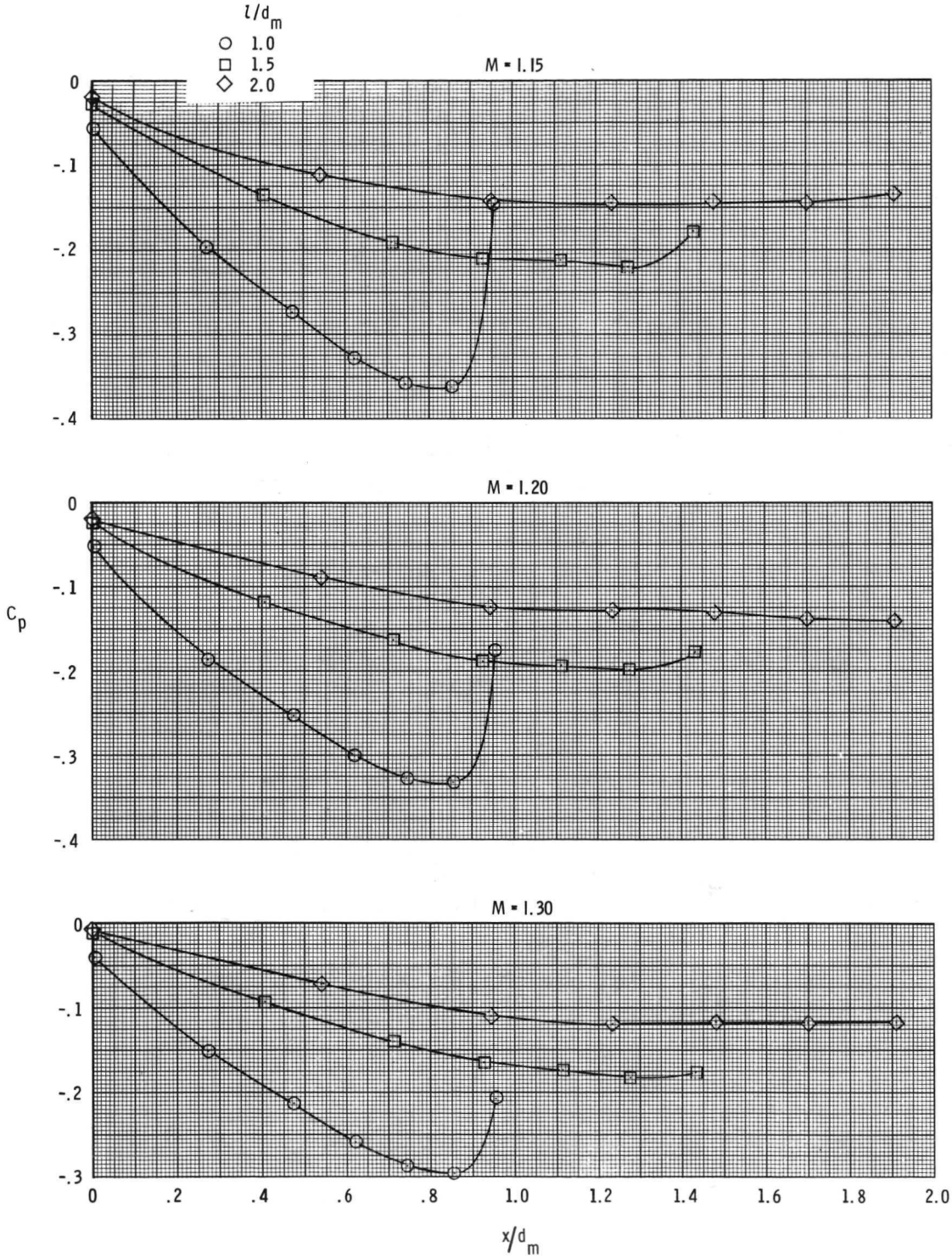
(b) M = 0.75, 0.80, 0.85, and 0.90.

Figure 7.- Continued.



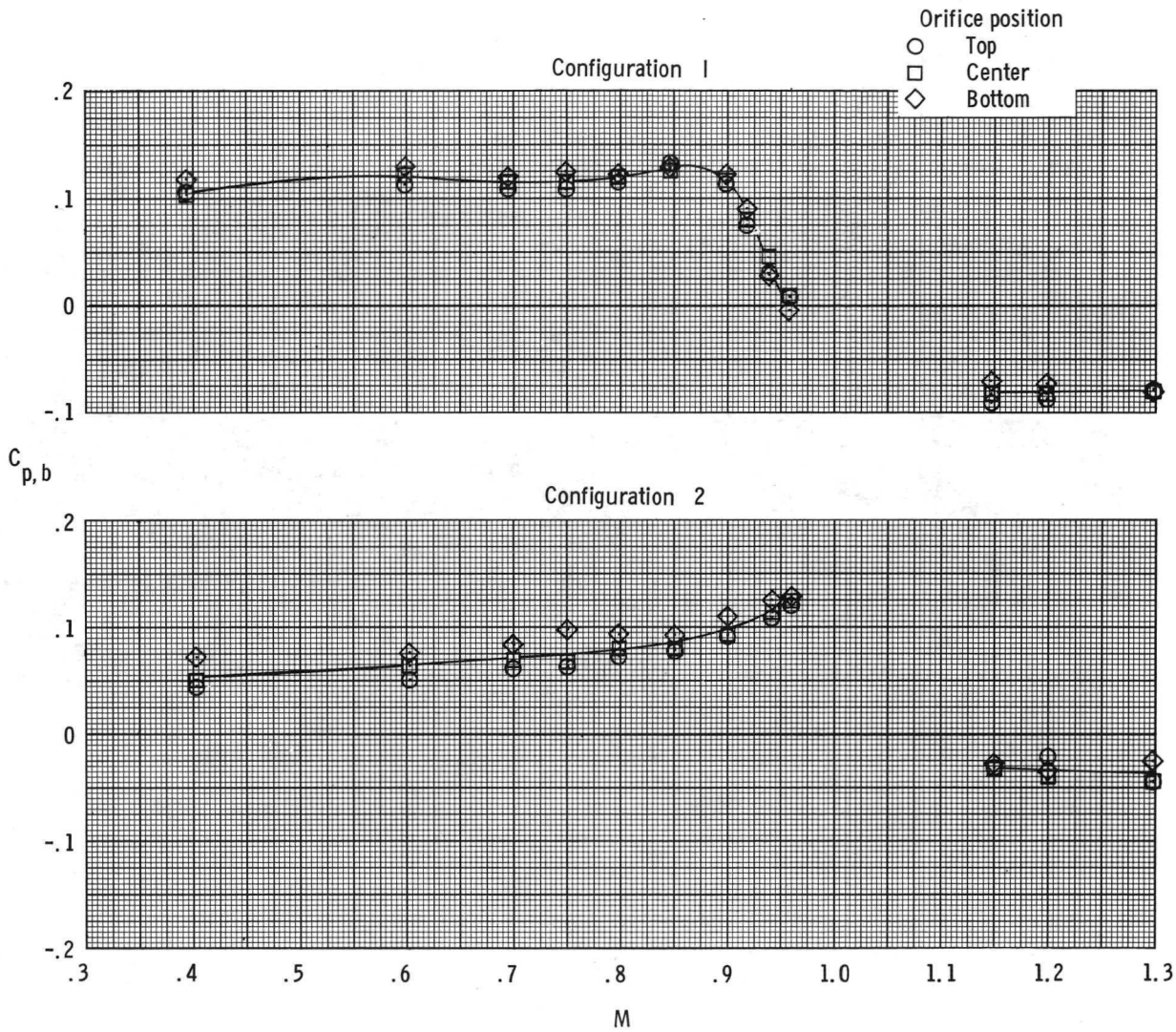
(c) M = 0.92, 0.94, and 0.96.

Figure 7.- Continued.



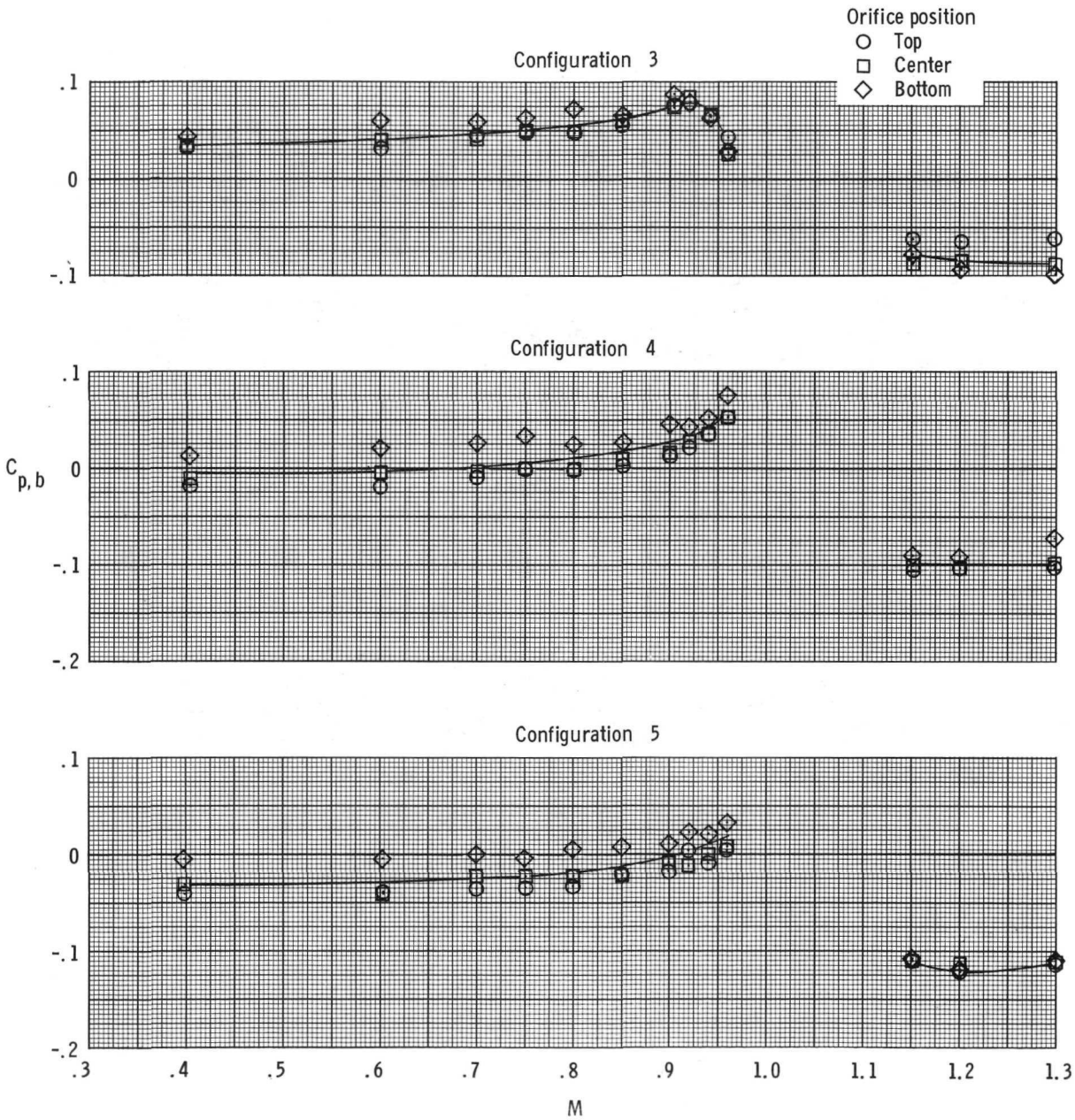
(d) M = 1.15, 1.20, and 1.30.

Figure 7.- Concluded.



(a) Configurations 1 and 2; $d_e/d_m = 0.6$.

Figure 8.- Variation of jet-off base pressure coefficients with Mach number.



(b) Configurations 3, 4, and 5; $d_e/d_m = 0.7$.

Figure 8.- Concluded.

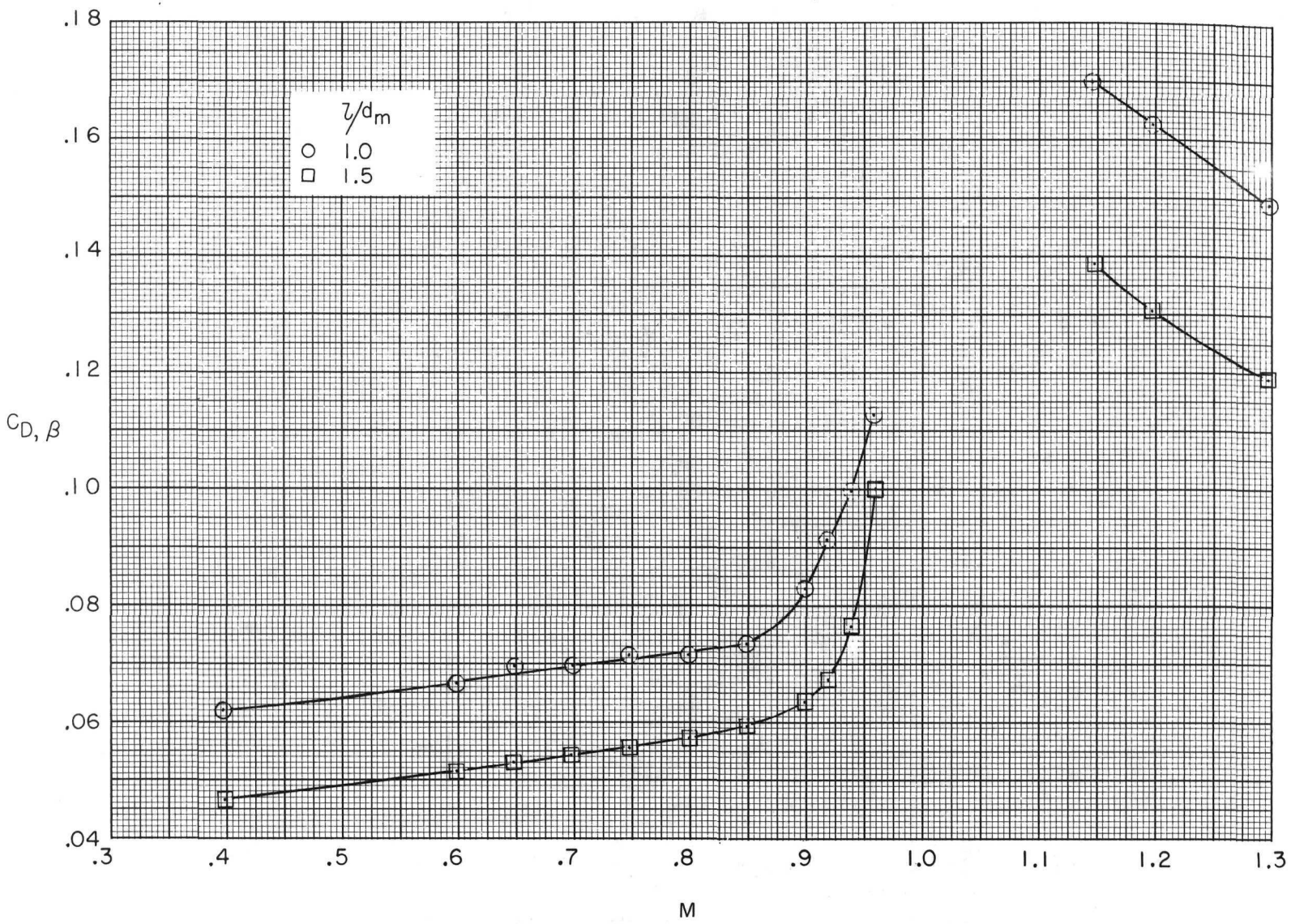


Figure 9.- Variation of jet-off boattail drag with free-stream Mach number for configurations with $d_e/d_m = 0.6$.

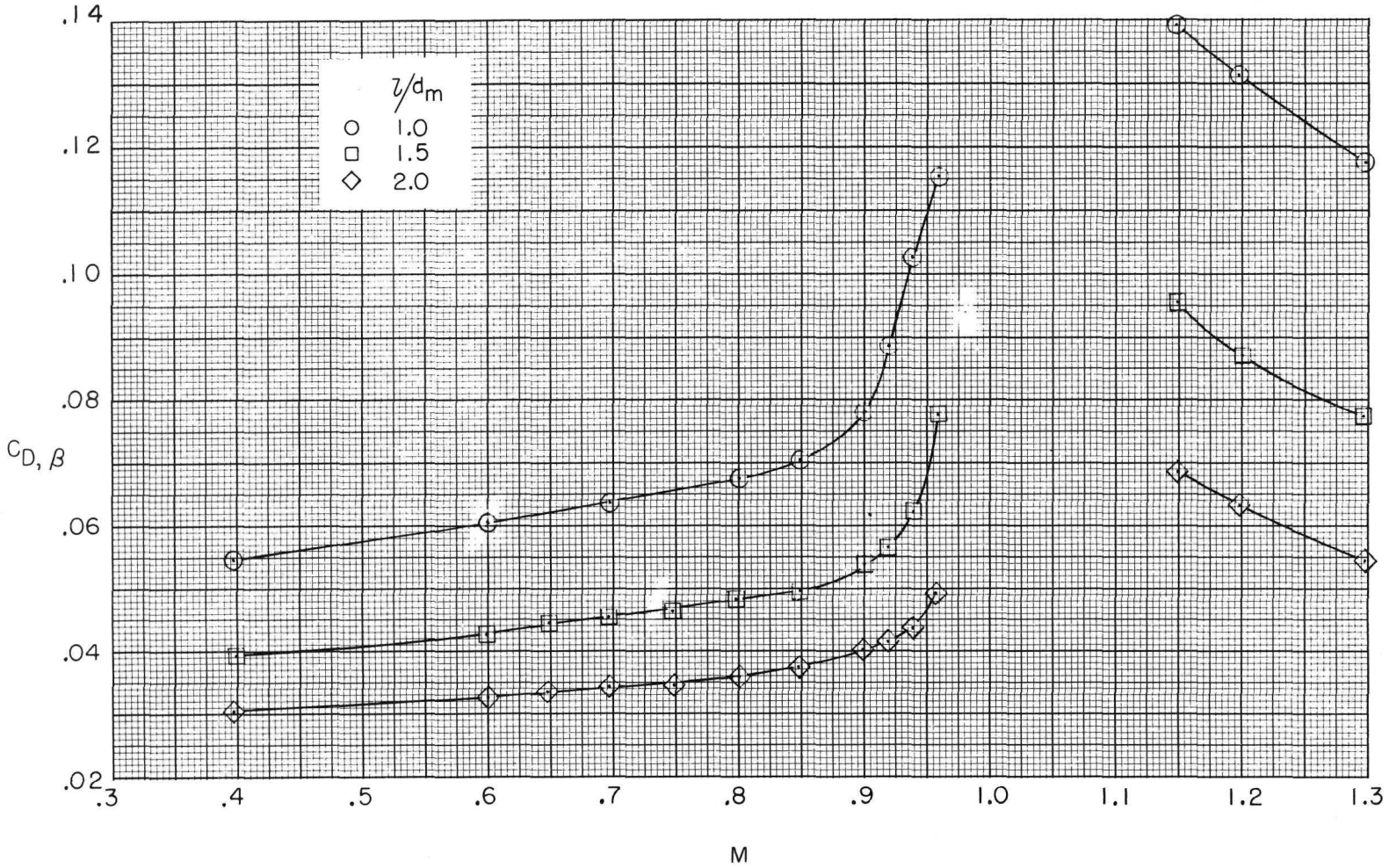


Figure 10.- Variation of jet-off boattail drag with free-stream Mach number for configurations with $d_e/d_m = 0.7$.

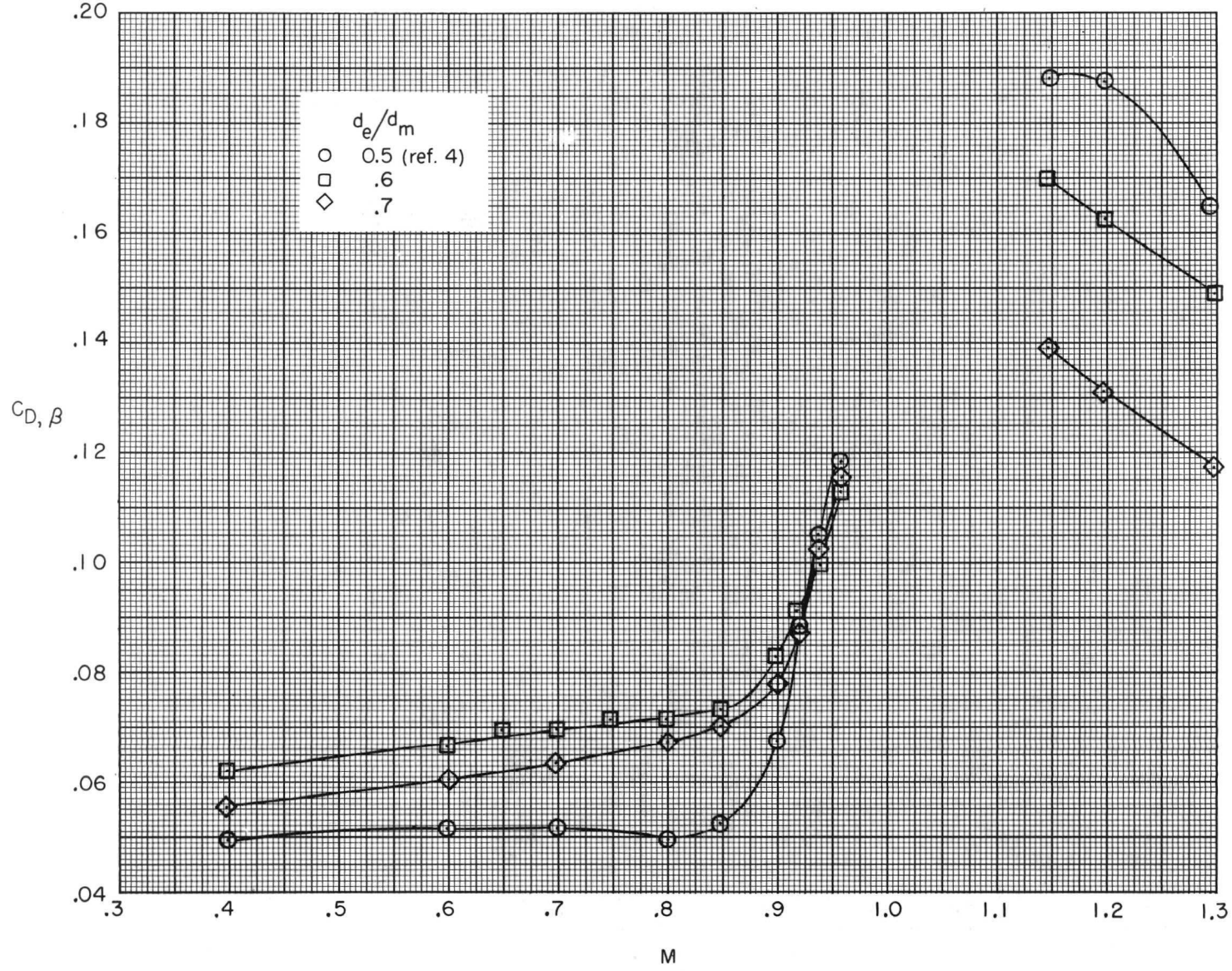


Figure 11.- Variation of jet-off boattail drag coefficients with Mach number for configurations with $l/d_m = 1.0$.

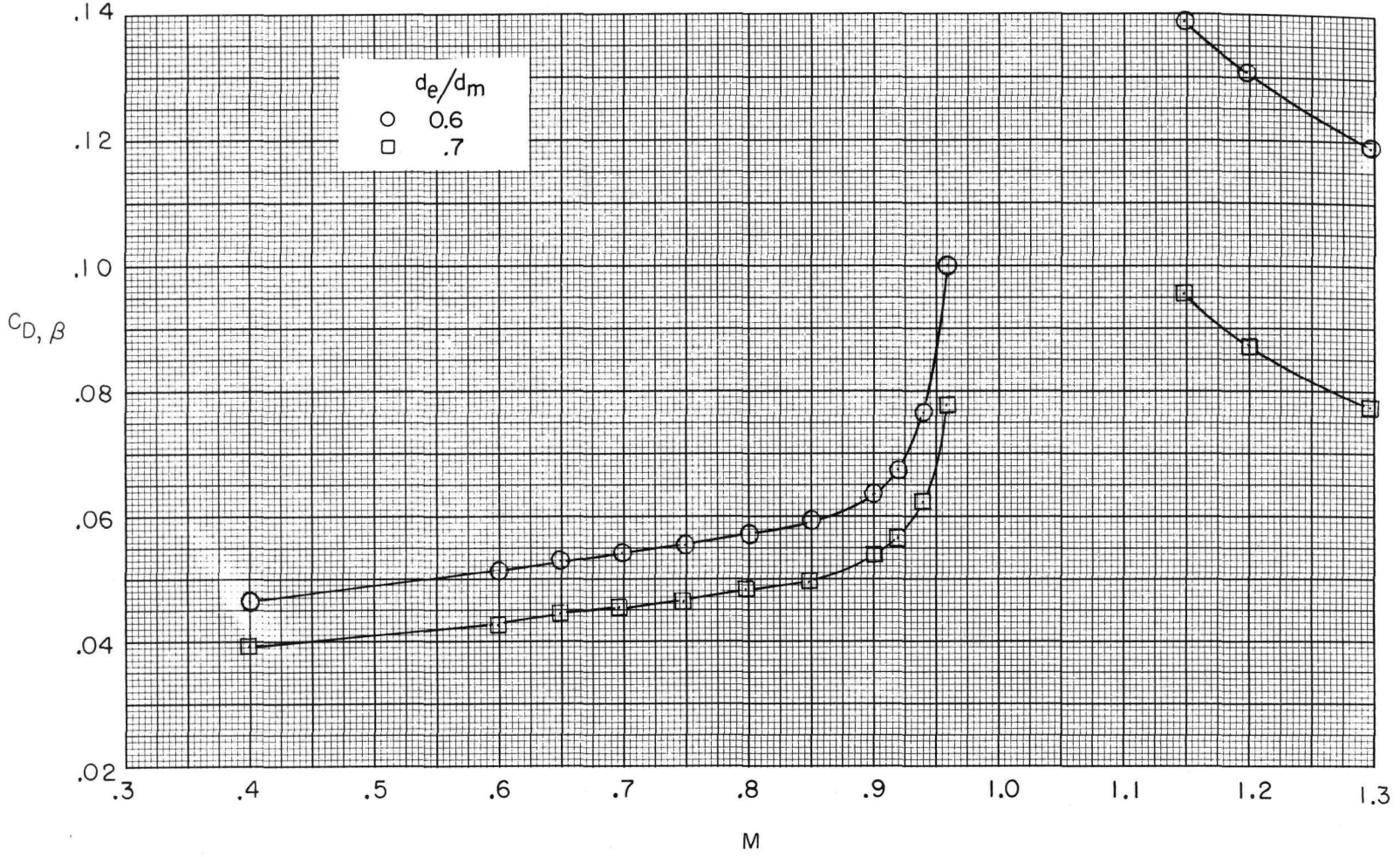
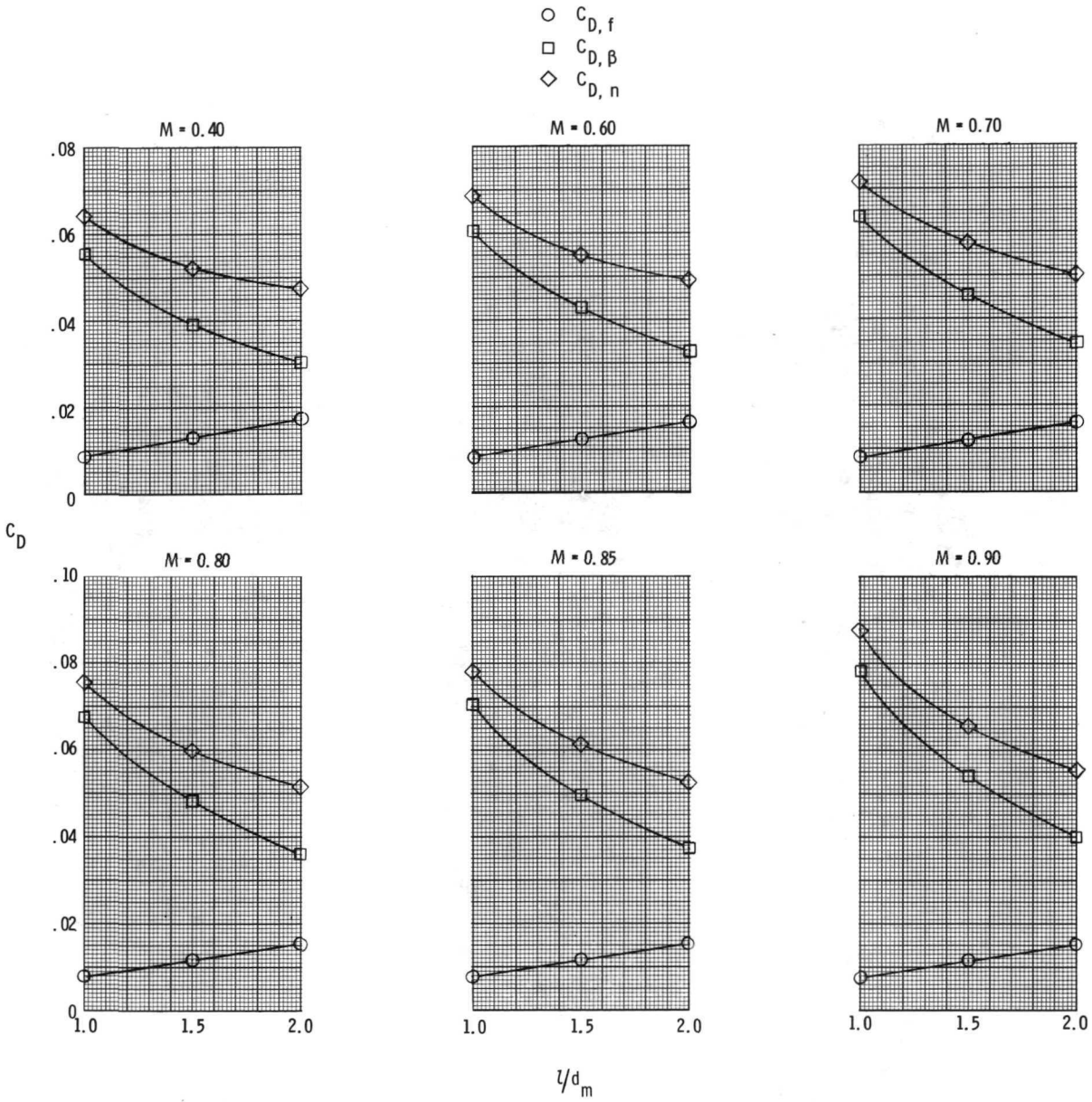
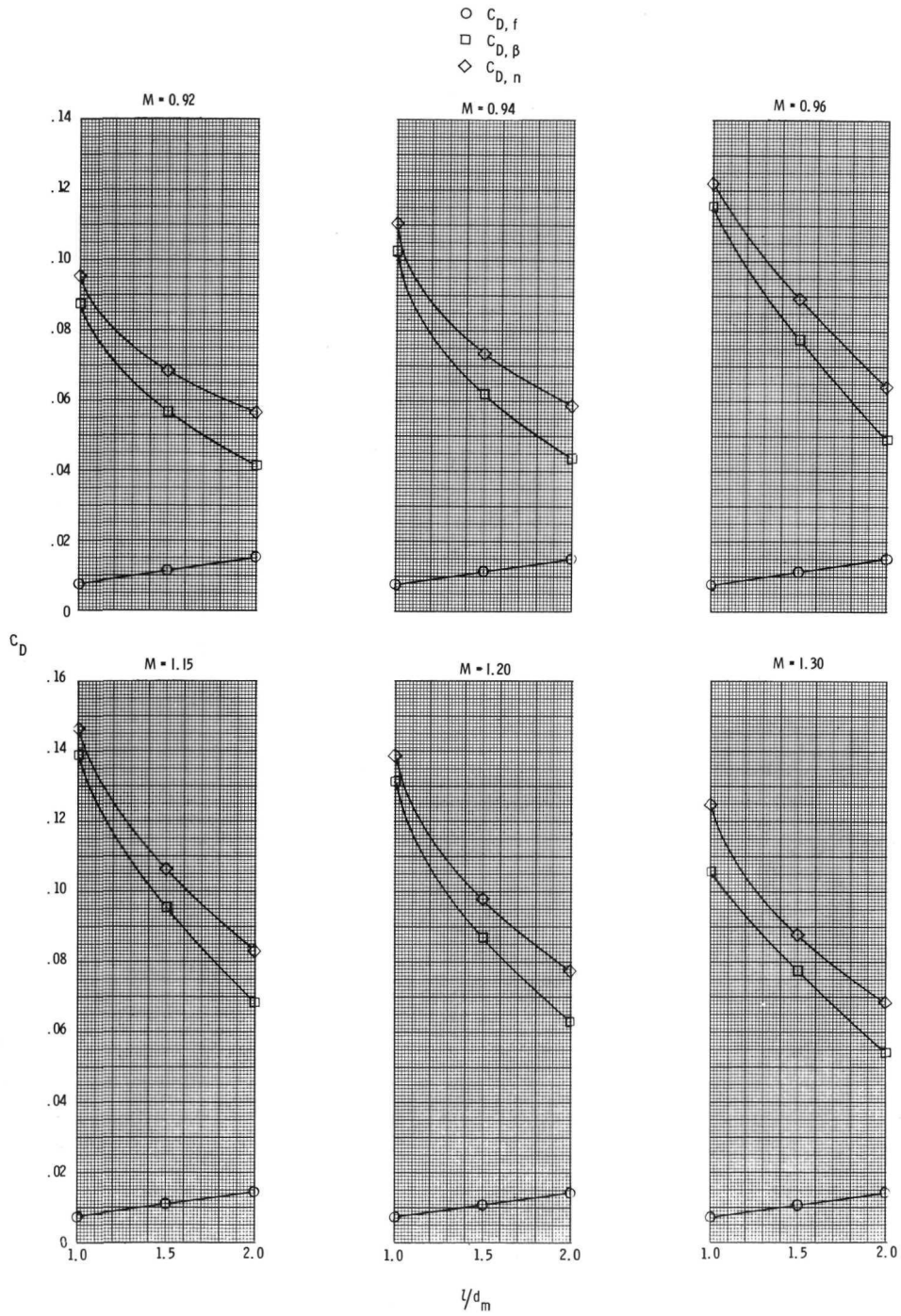


Figure 12.- Variation of jet-off boattail drag coefficients with Mach number for configurations with $l/d_m = 1.5$.



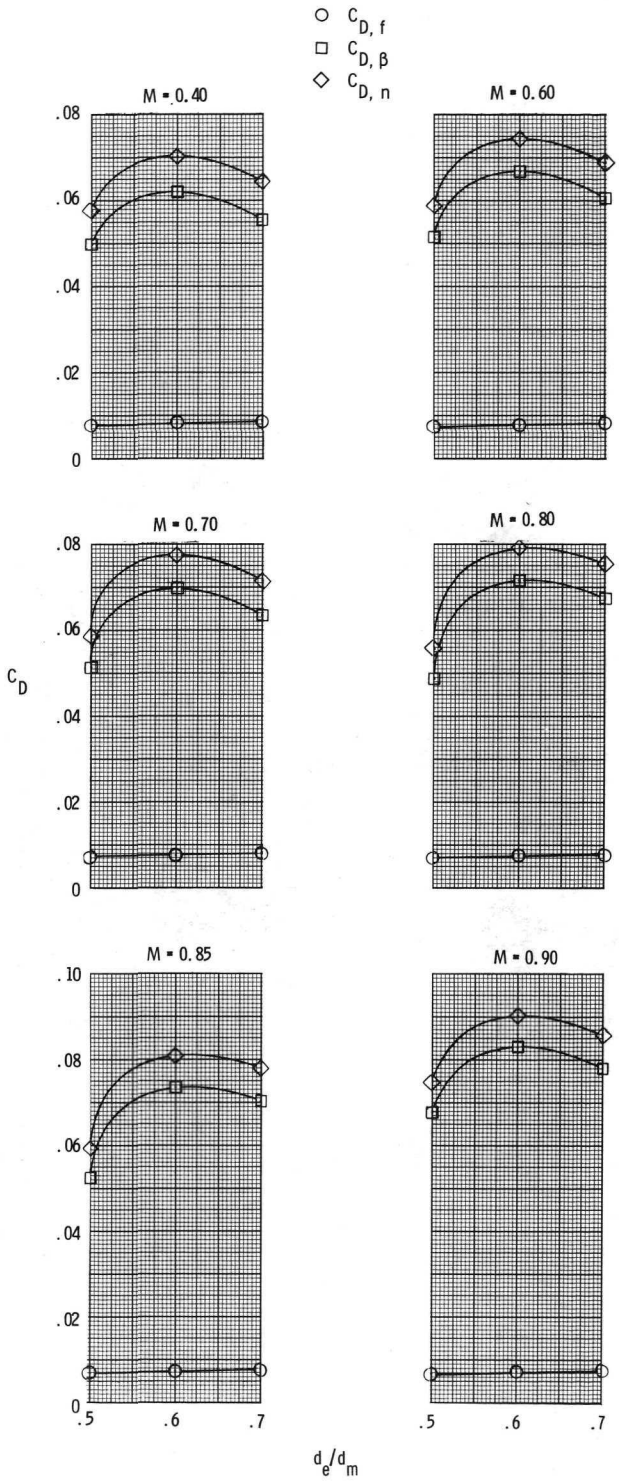
(a) M = 0.40, 0.60, 0.70, 0.80, 0.85, and 0.90.

Figure 13.- Variation of jet-off drag with boattail fineness ratio for configurations with $d_e/d_m = 0.7$.



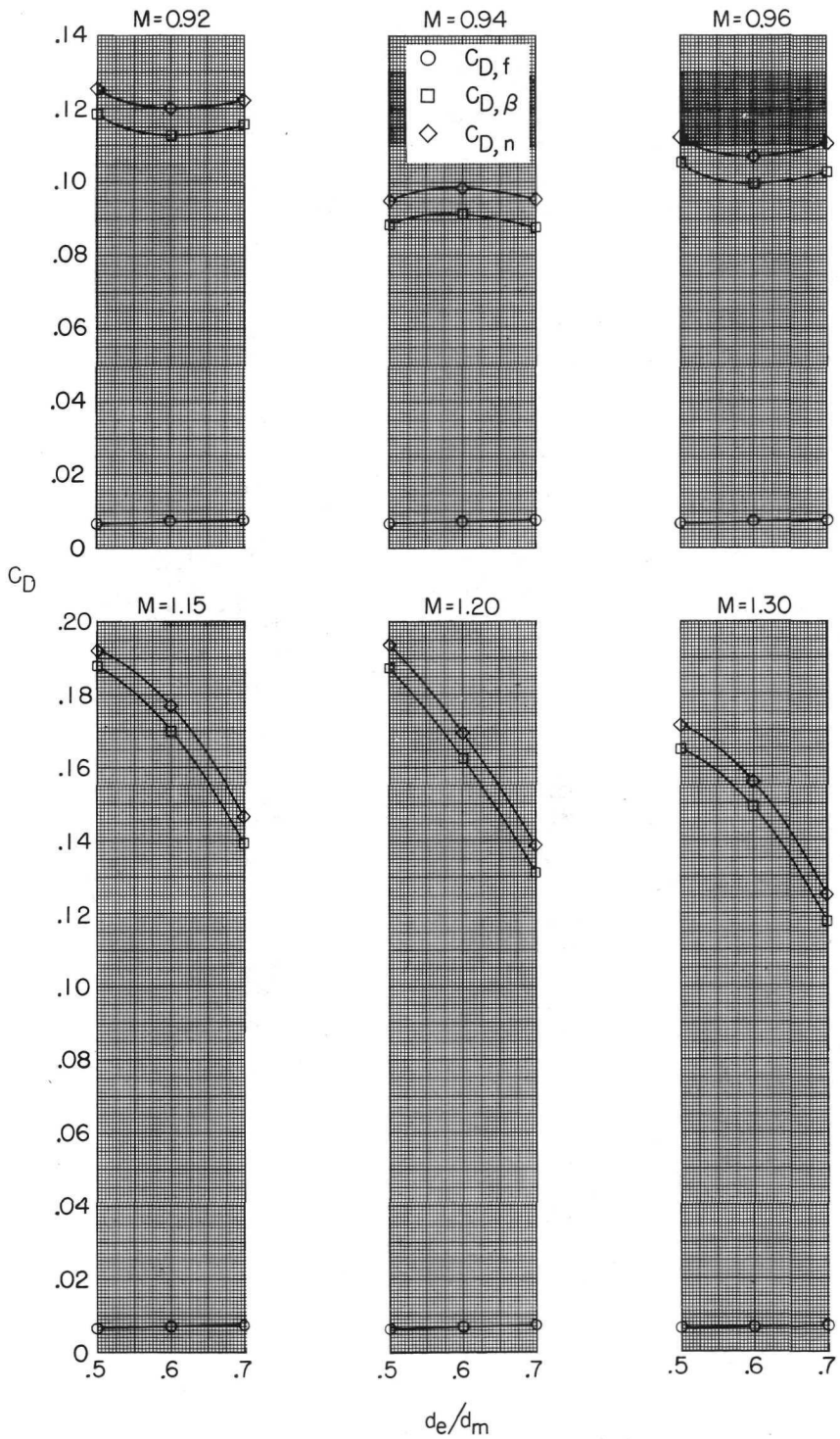
(b) M = 0.92, 0.94, 0.96, 1.15, 1.20, and 1.30.

Figure 13.- Concluded.



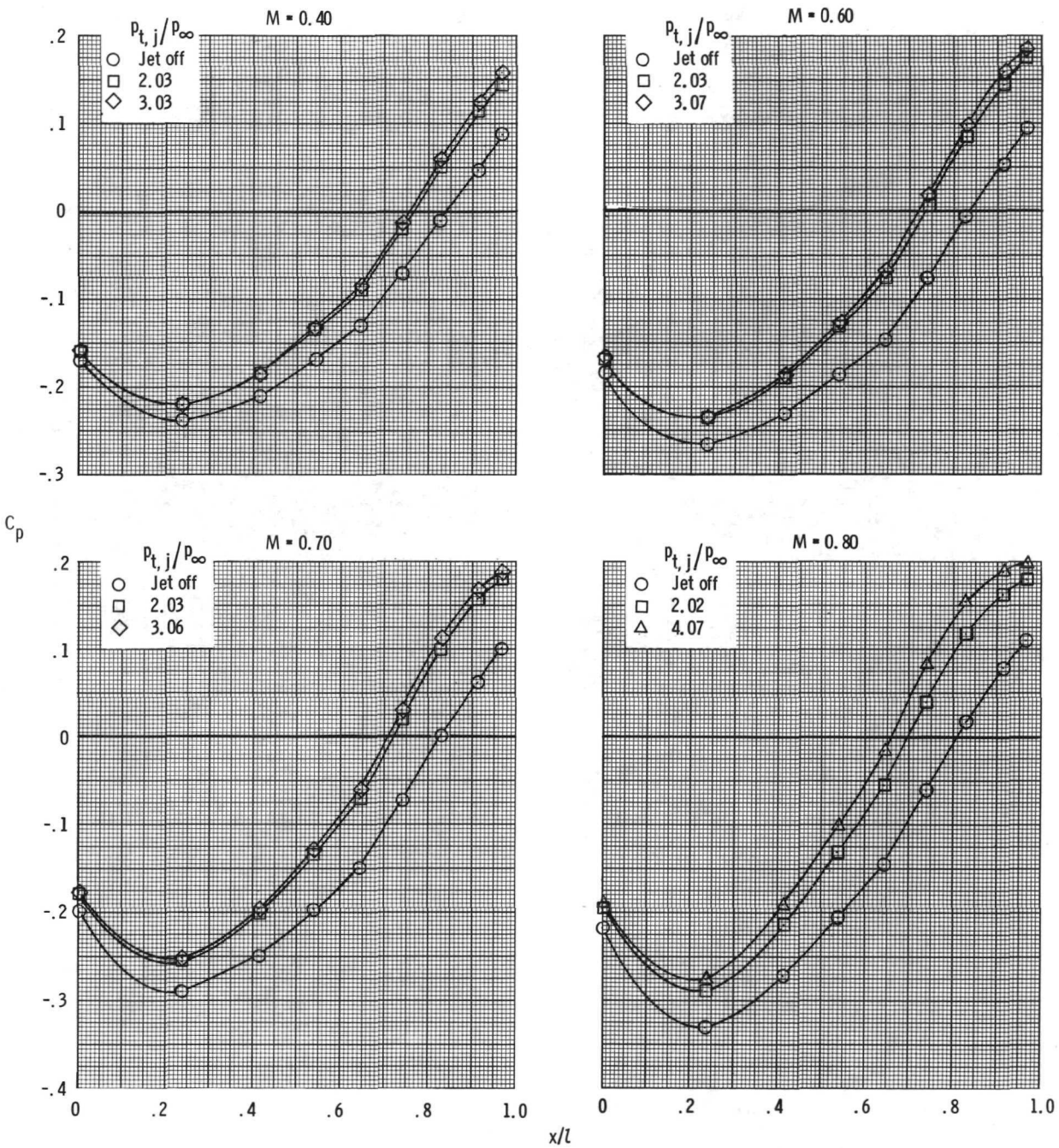
(a) M = 0.40, 0.60, 0.70, 0.80, 0.85, and 0.90.

Figure 14.- Variation of jet-off drag with closure ratio for configurations with $l/d_m = 1.0$.



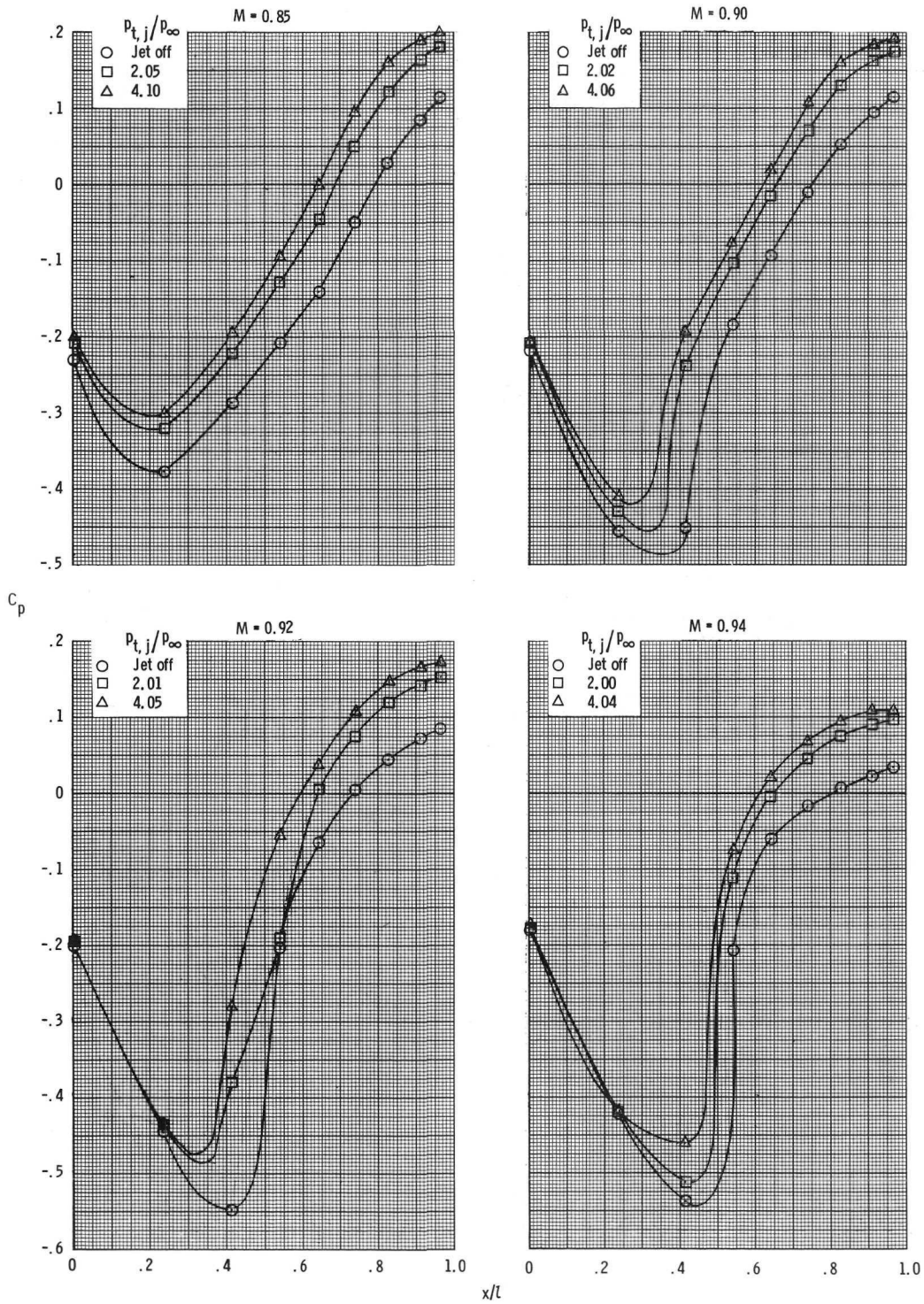
(b) M = 0.92, 0.94, 0.96, 1.15, 1.20, and 1.30.

Figure 14.- Concluded.



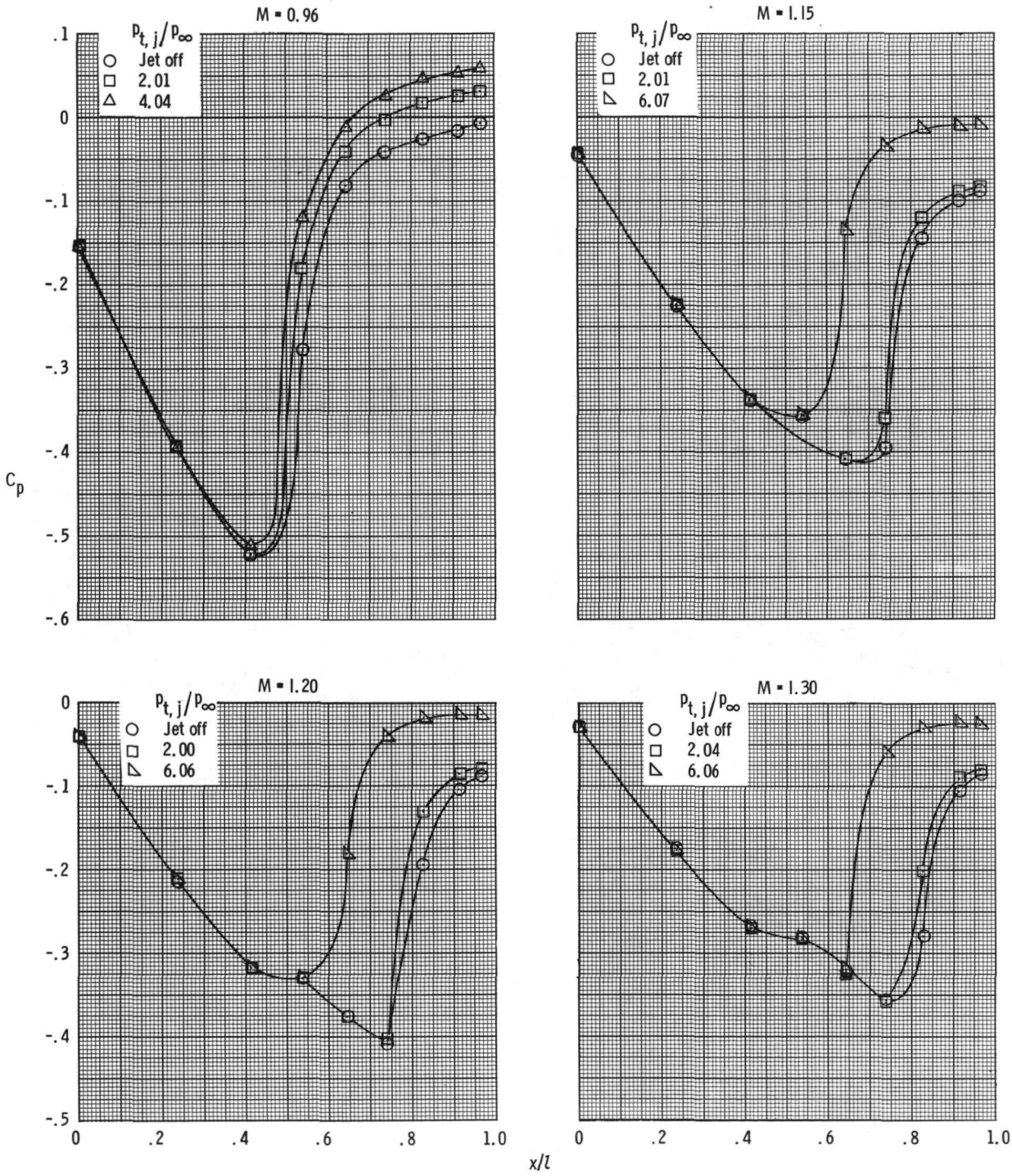
(a) M = 0.40, 0.60, 0.70, and 0.80.

Figure 15.- Boattail pressure-coefficient distributions on configuration 1 $(l/d_m = 1.0;$ $d_e/d_m = 0.6)$ at various Mach numbers and three values of jet total-pressure ratio.



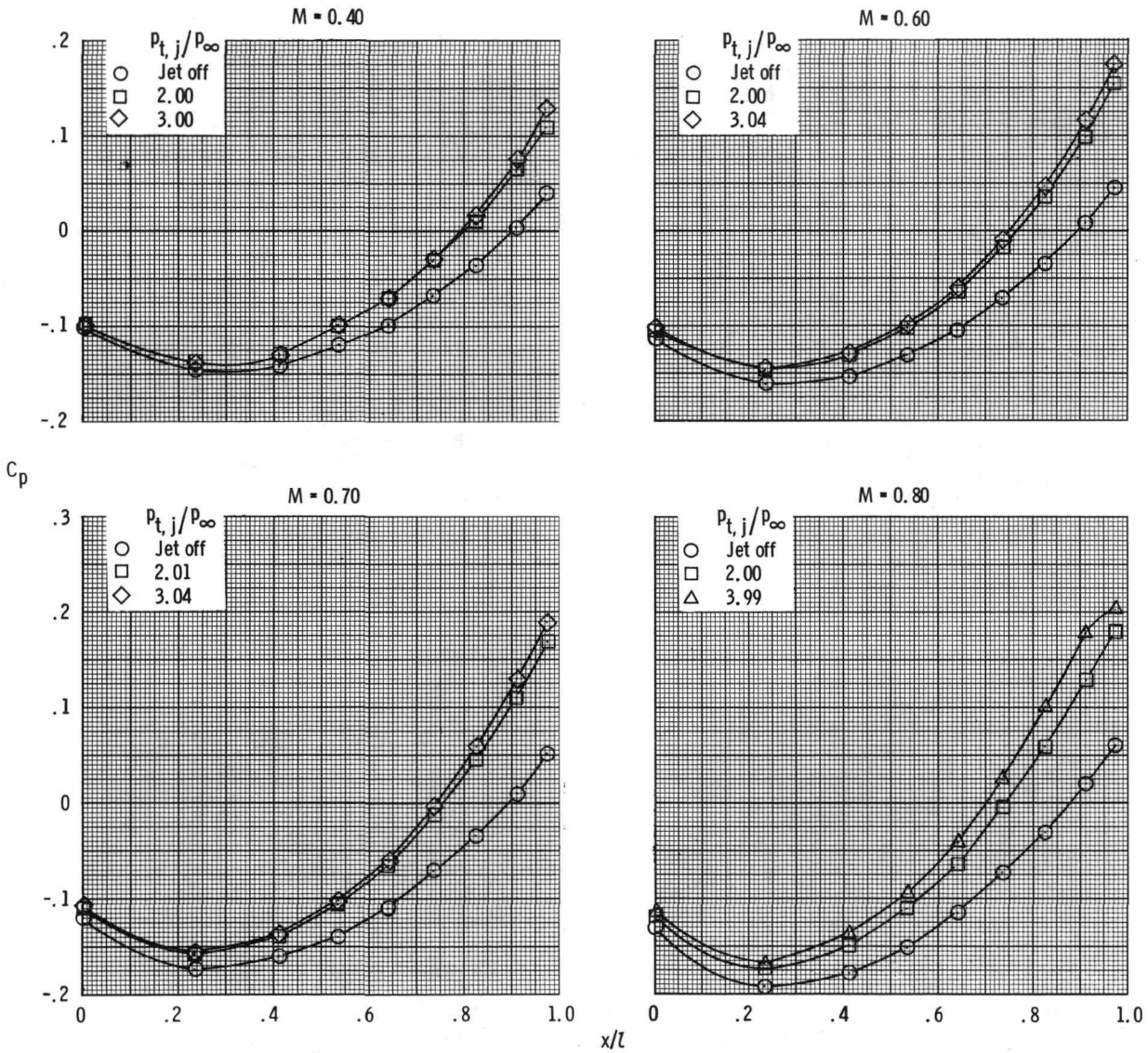
(b) M = 0.85, 0.90, 0.92, and 0.94.

Figure 15.- Continued.



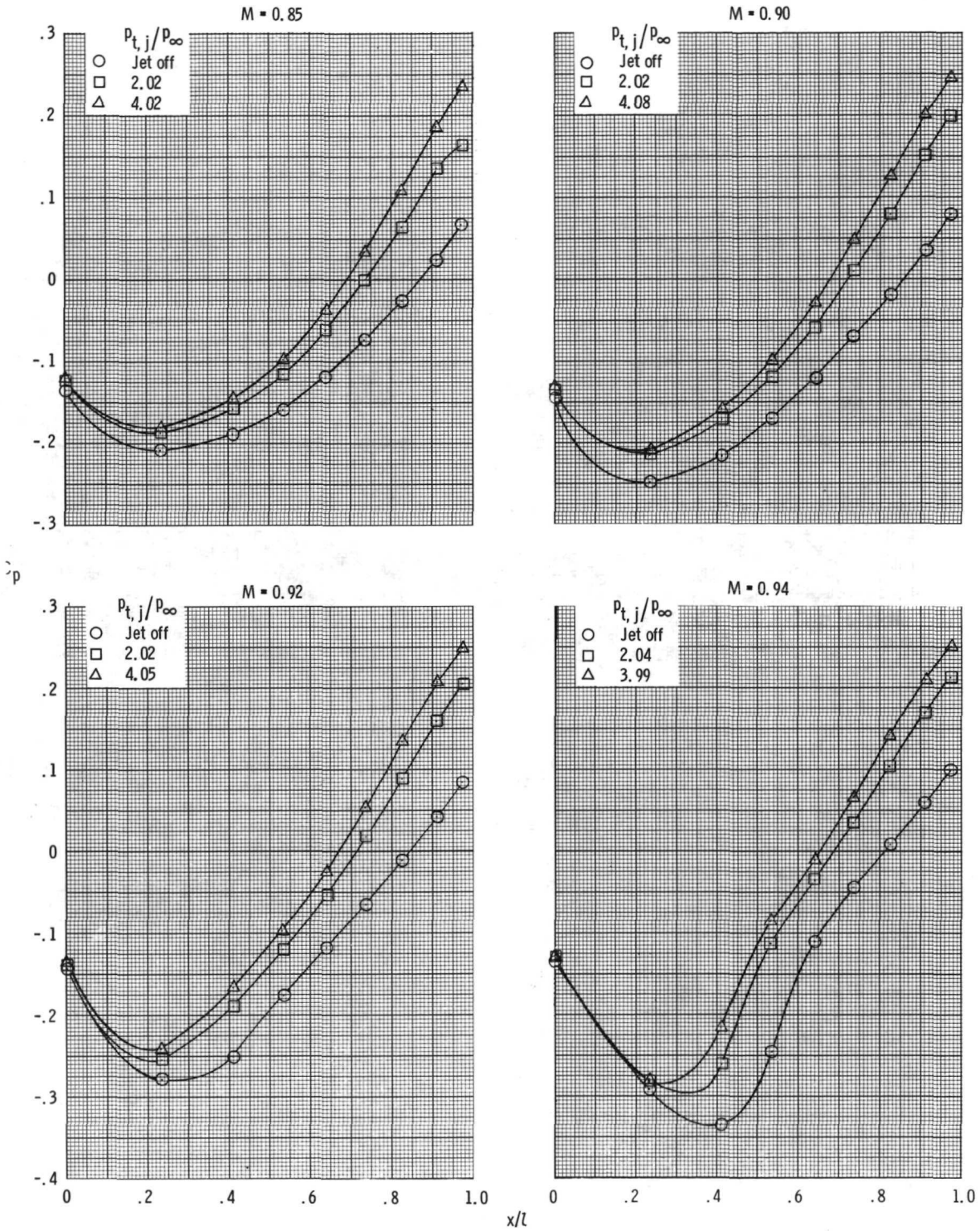
(c) M = 0.96, 1.15, 1.20, and 1.30.

Figure 15.- Concluded.



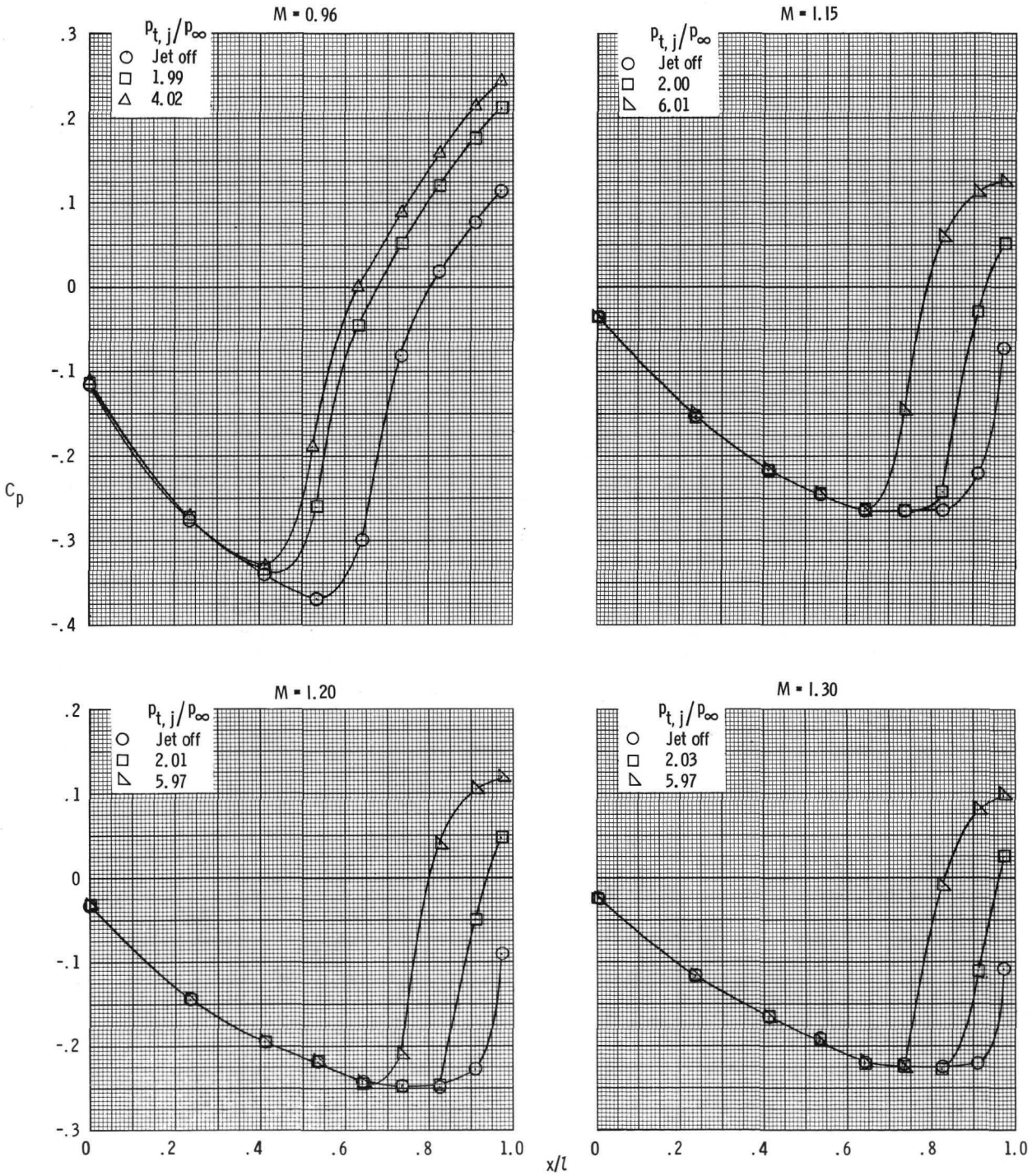
(a) M = 0.40, 0.60, 0.70, and 0.80.

Figure 16.- Boattail pressure-coefficient distributions on configuration 2 $\left(l/d_m = 1.5;\ d_e/d_m = 0.6\right)$ at various Mach numbers and three values of jet total-pressure ratio.



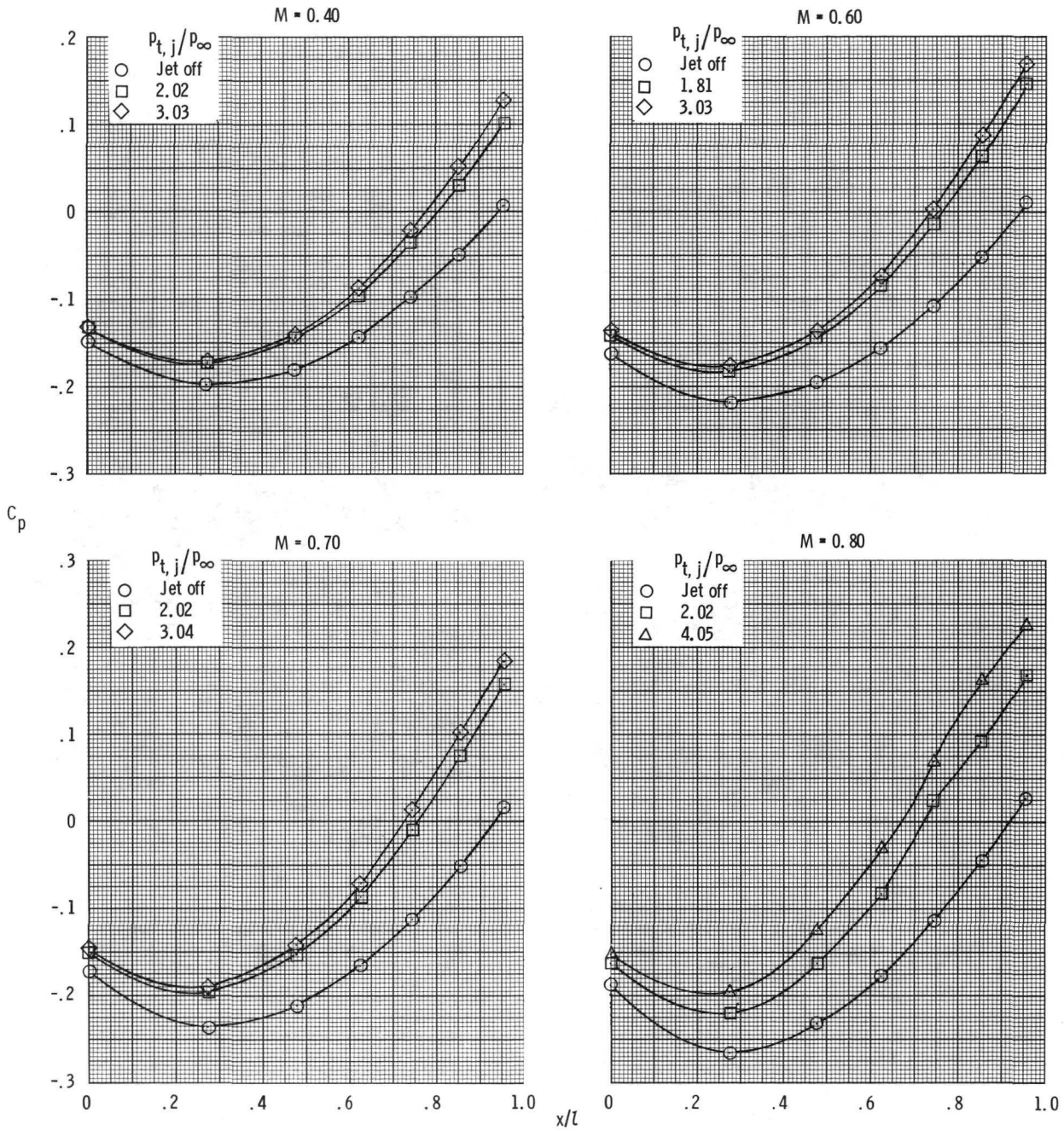
(b) M = 0.85, 0.90, 0.92, and 0.94.

Figure 16.- Continued.



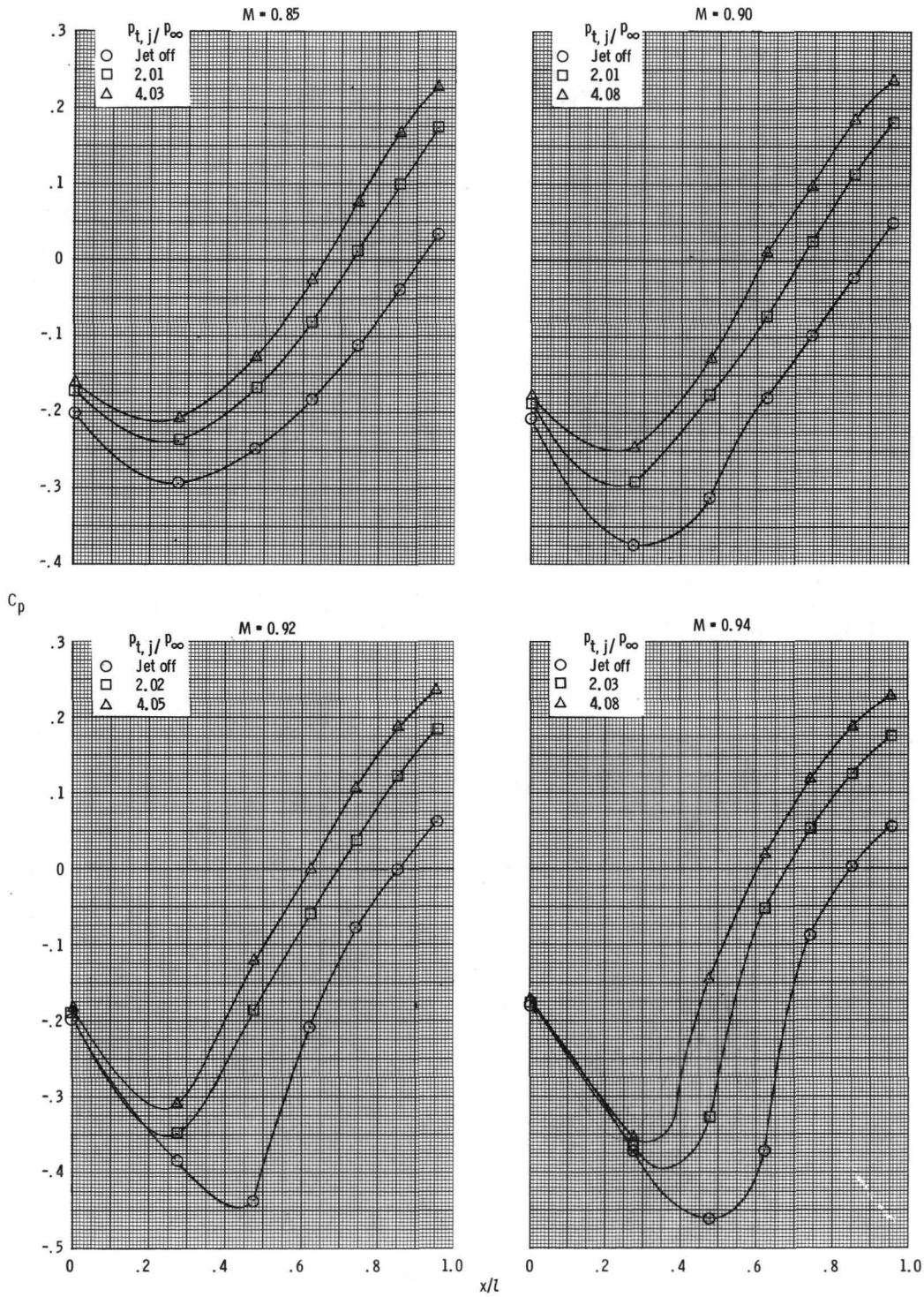
(c) M = 0.96, 1.15, 1.20, and 1.30.

Figure 16.- Concluded.



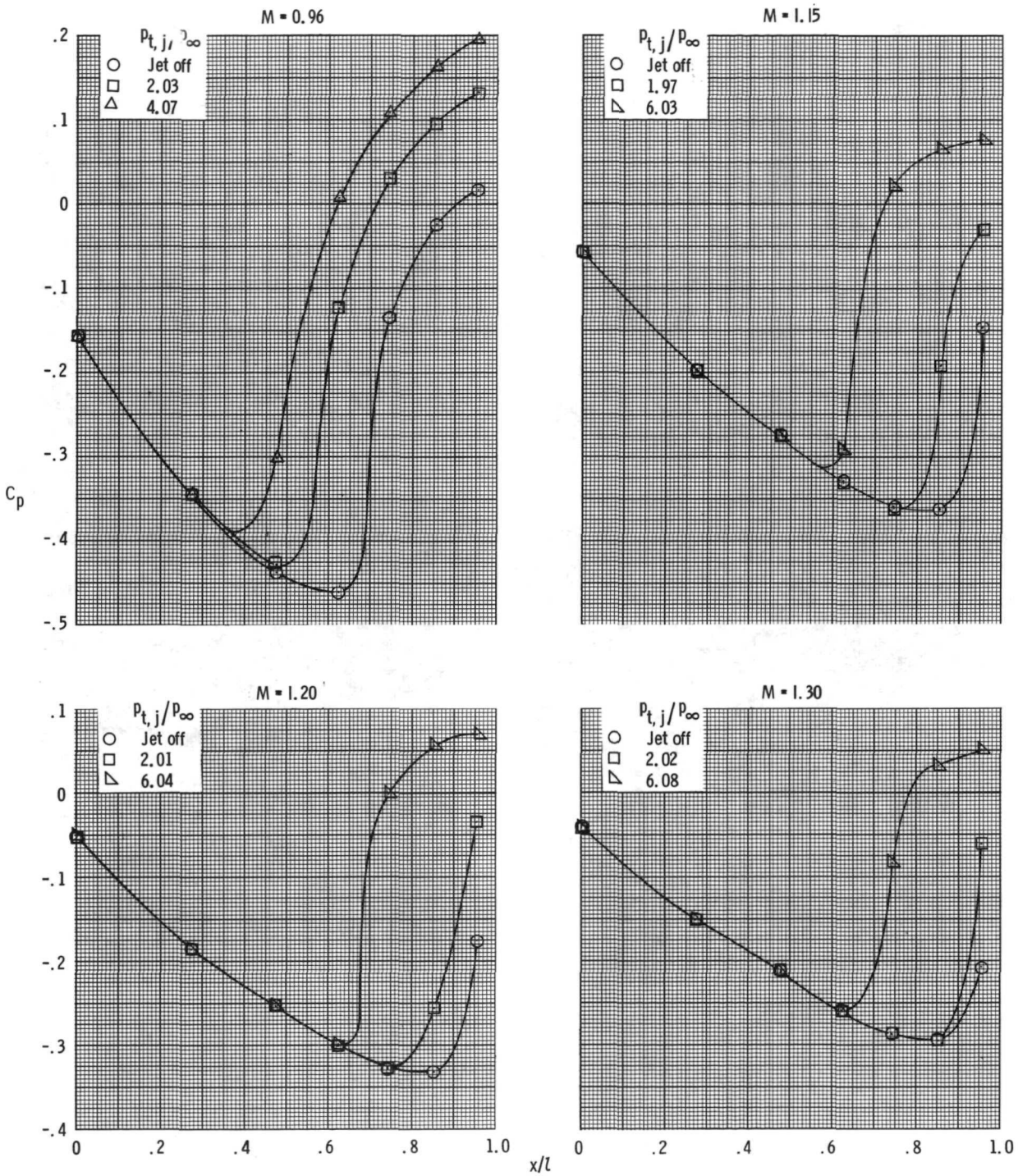
(a) M = 0.40, 0.60, 0.70, and 0.80.

Figure 17.- Boattail pressure-coefficient distributions on configuration 3 $\left(l/d_m = 1.0;\ d_e/d_m = 0.7\right)$ at various Mach numbers and three values of jet total-pressure ratio.



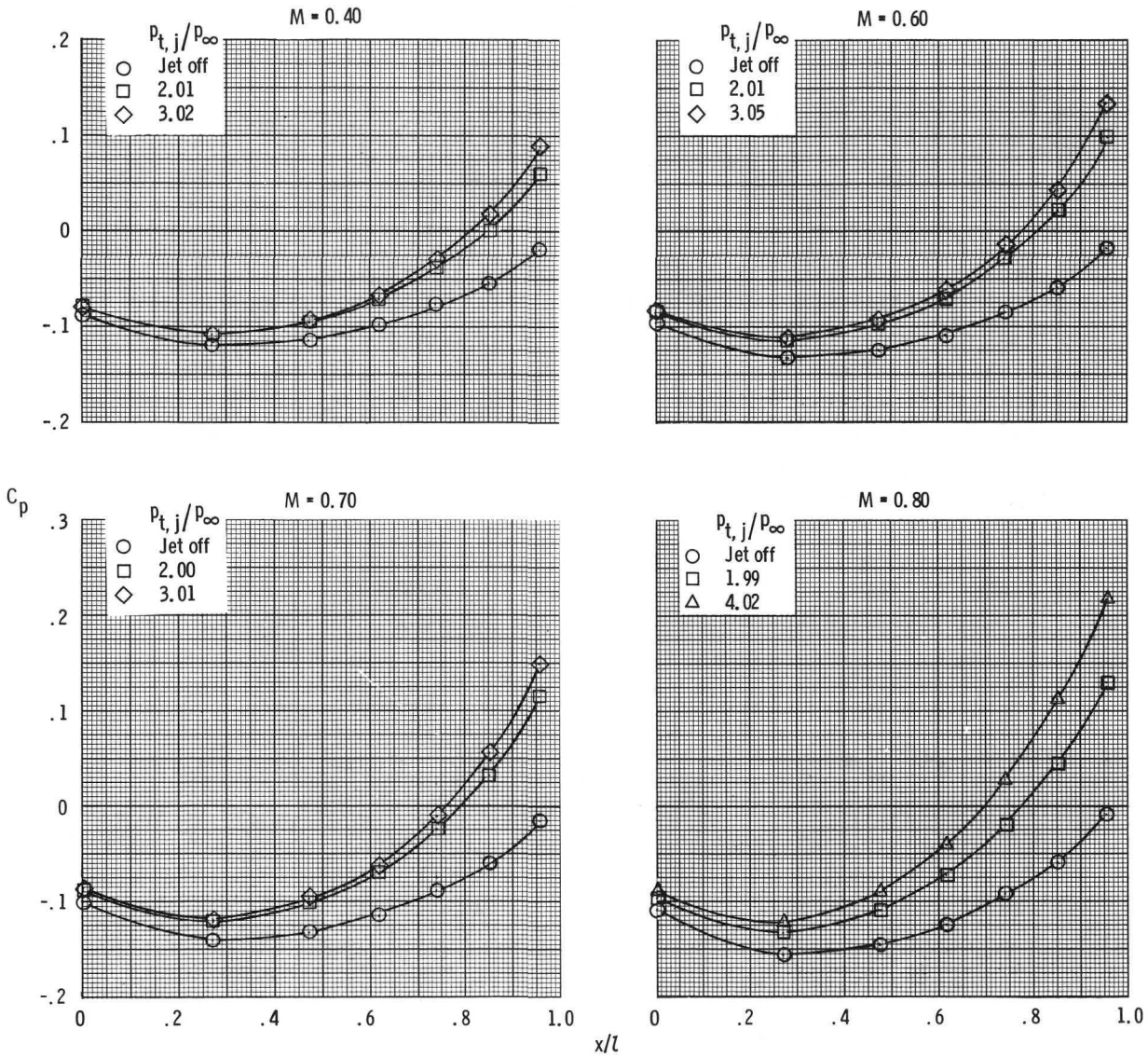
(b) M = 0.85, 0.90, 0.92, and 0.94.

Figure 17.- Continued.



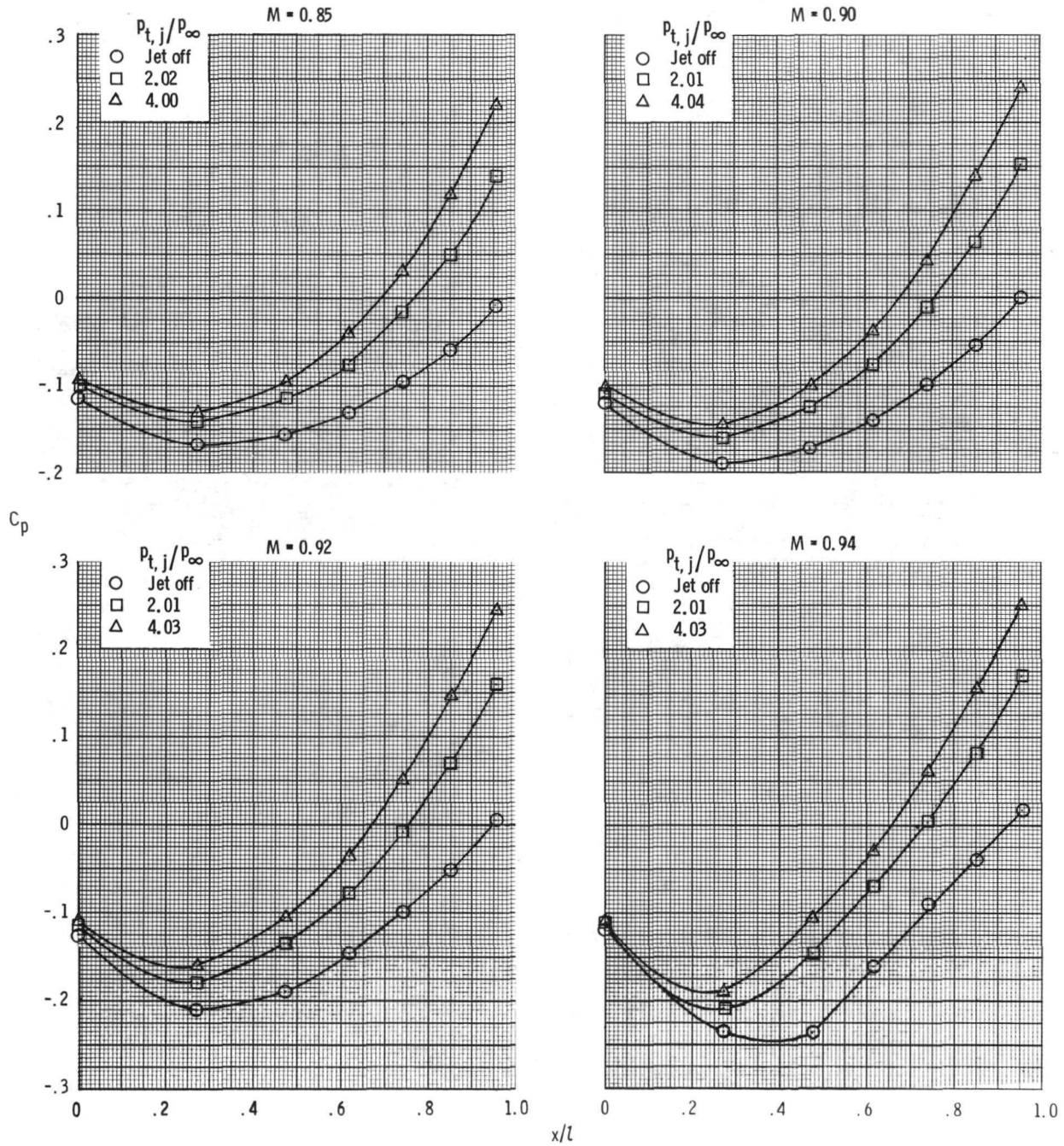
(c) M = 0.96, 1.15, 1.20, and 1.30.

Figure 17.- Concluded.



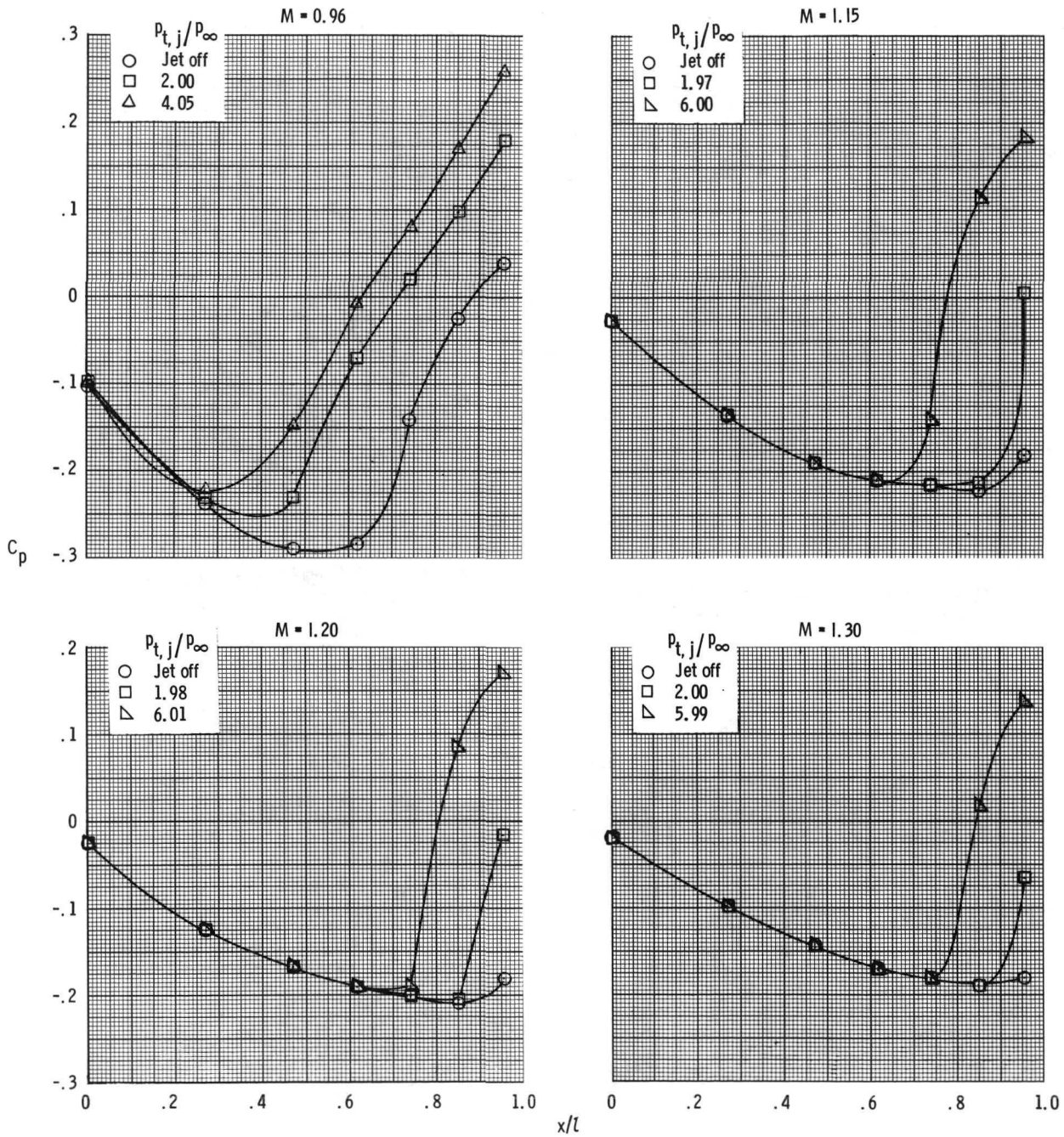
(a) M = 0.40, 0.60, 0.70, and 0.80.

Figure 18.- Boattail pressure-coefficient distributions on configuration 4 $(l/d_m = 1.5;$ $d_e/d_m = 0.7)$ at various Mach numbers and three values of jet total-pressure ratio.



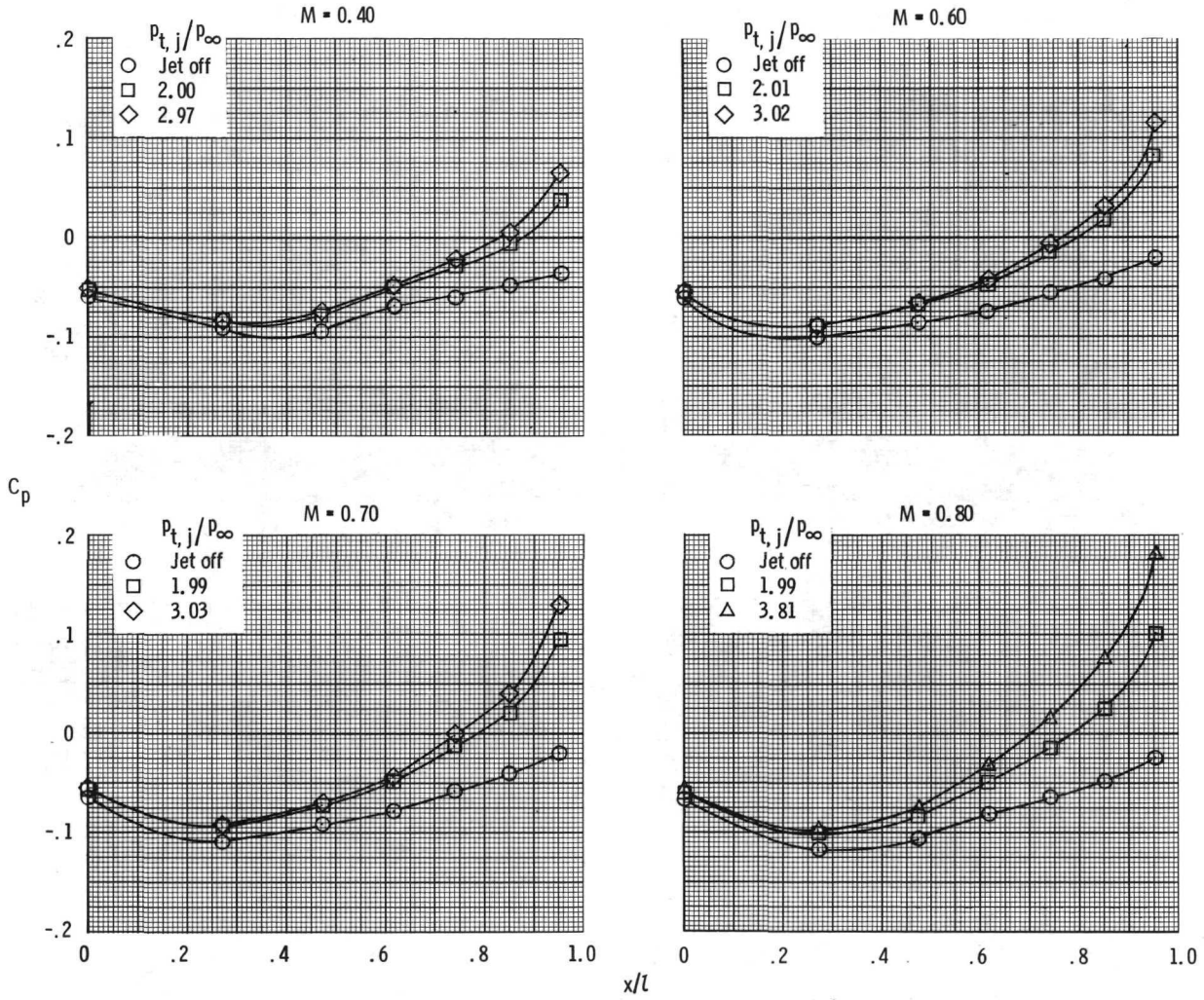
(b) M = 0.85, 0.90, 0.92, and 0.94.

Figure 18.- Continued.



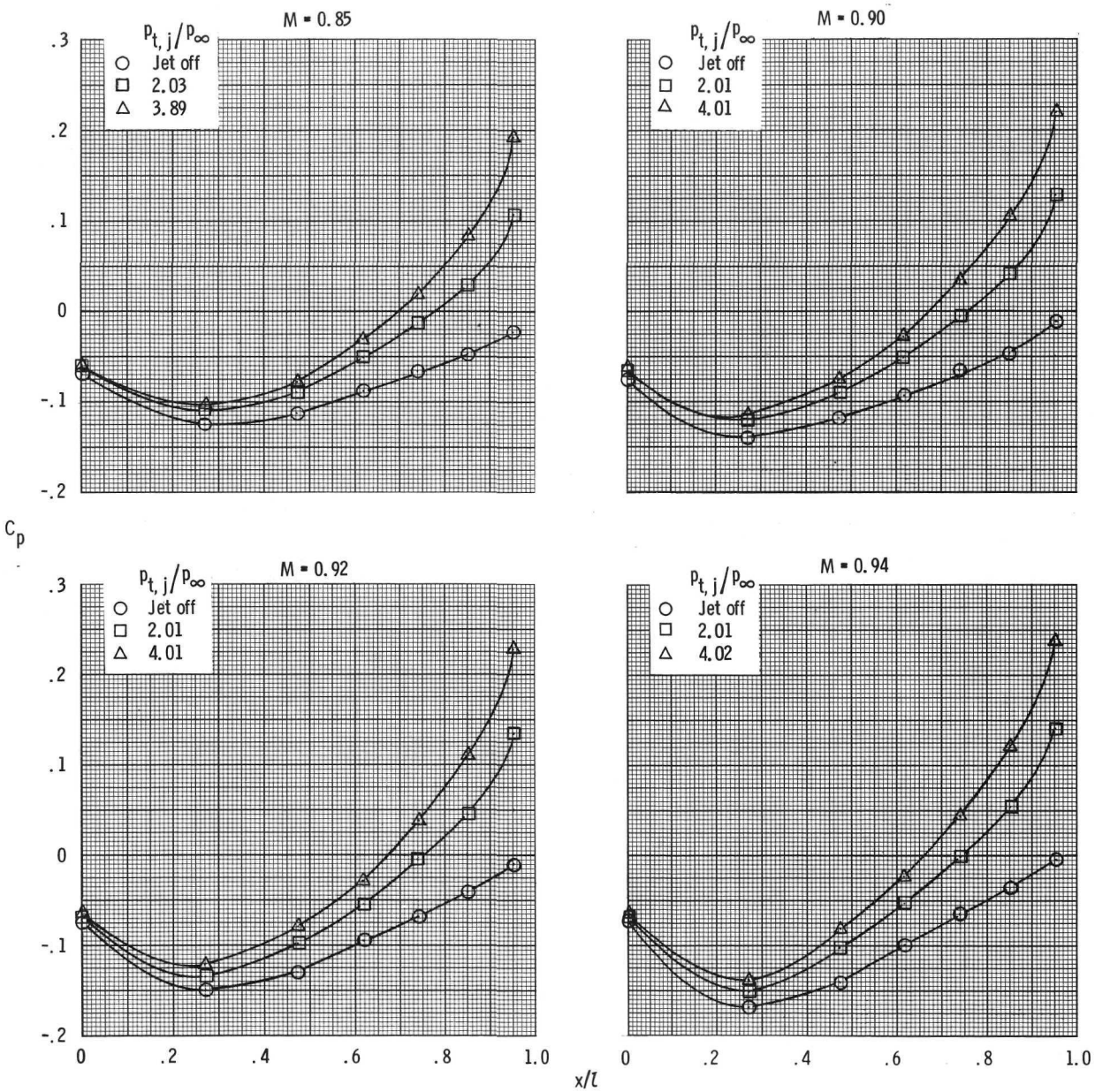
(c) M = 0.96, 1.15, 1.20, and 1.30.

Figure 18.- Concluded.



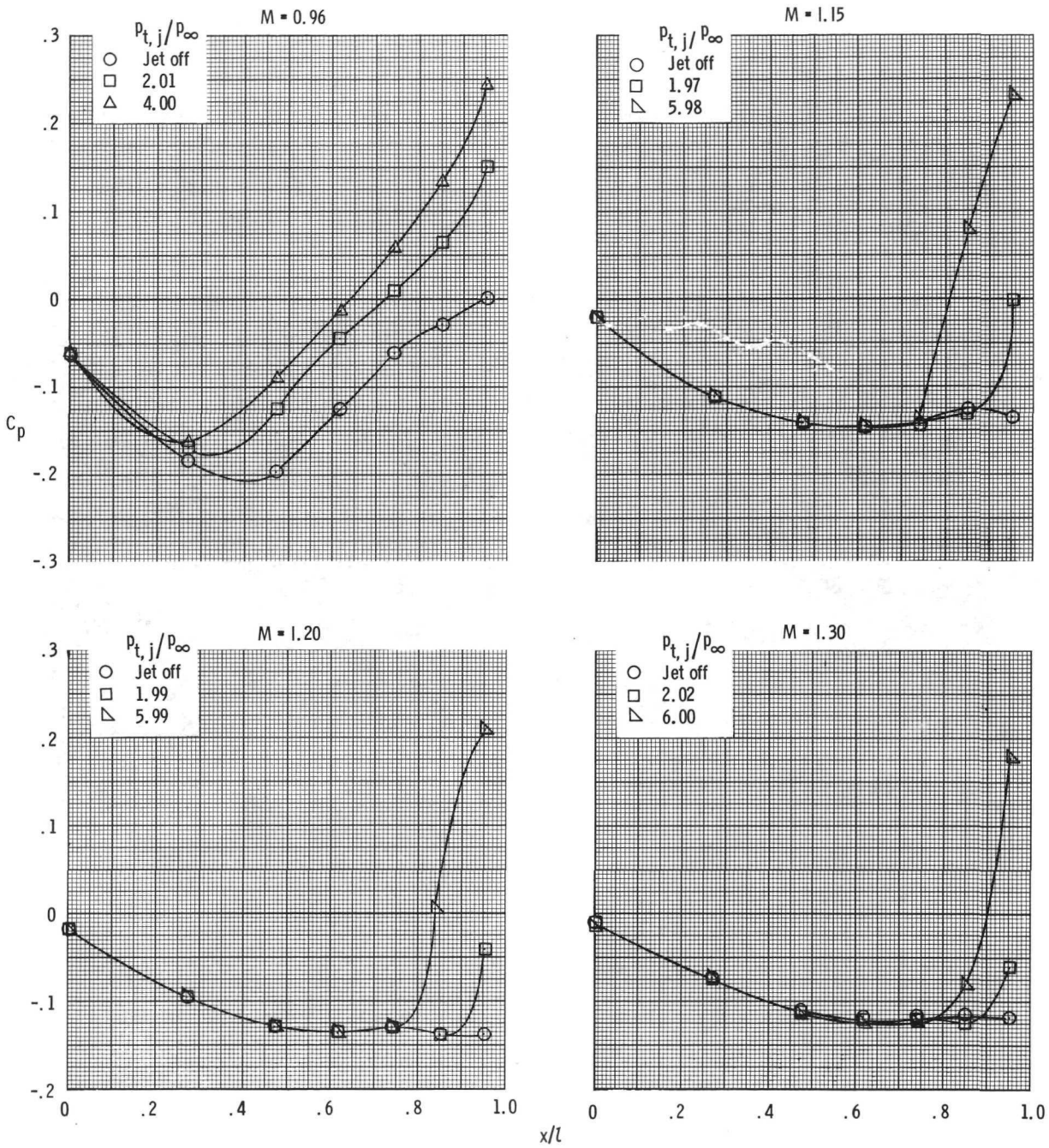
(a) M = 0.40, 0.60, 0.70, and 0.80.

Figure 19.- Boattail pressure-coefficient distributions on configuration 5 $\left(l/d_m = 2.0;\ d_e/d_m = 0.7\right)$ at various Mach numbers and three values of jet total-pressure ratio.



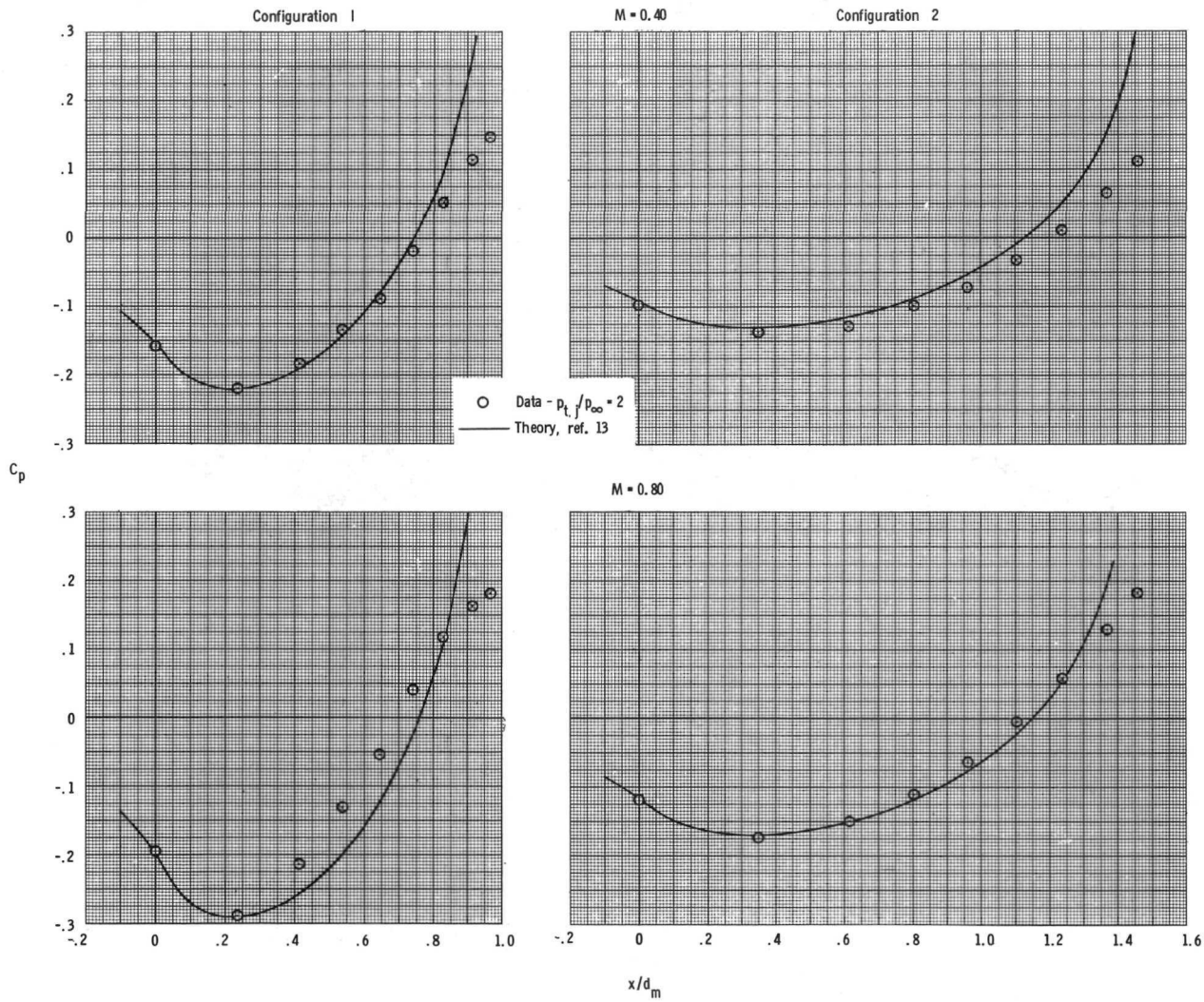
(b) M = 0.85, 0.90, 0.92, and 0.94.

Figure 19.- Continued.



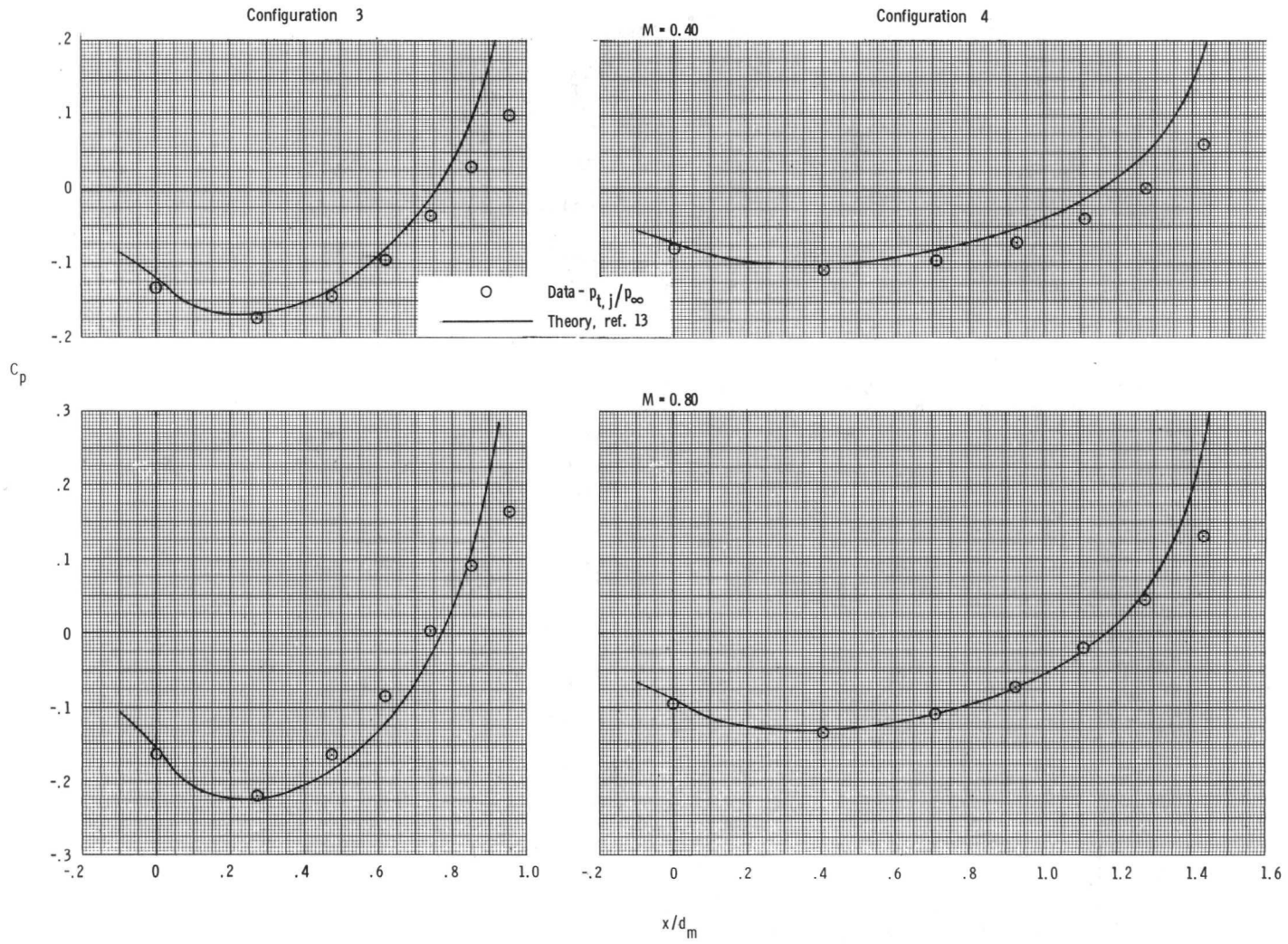
(c) M = 0.96, 1.15, 1.20, and 1.30.

Figure 19.- Concluded.



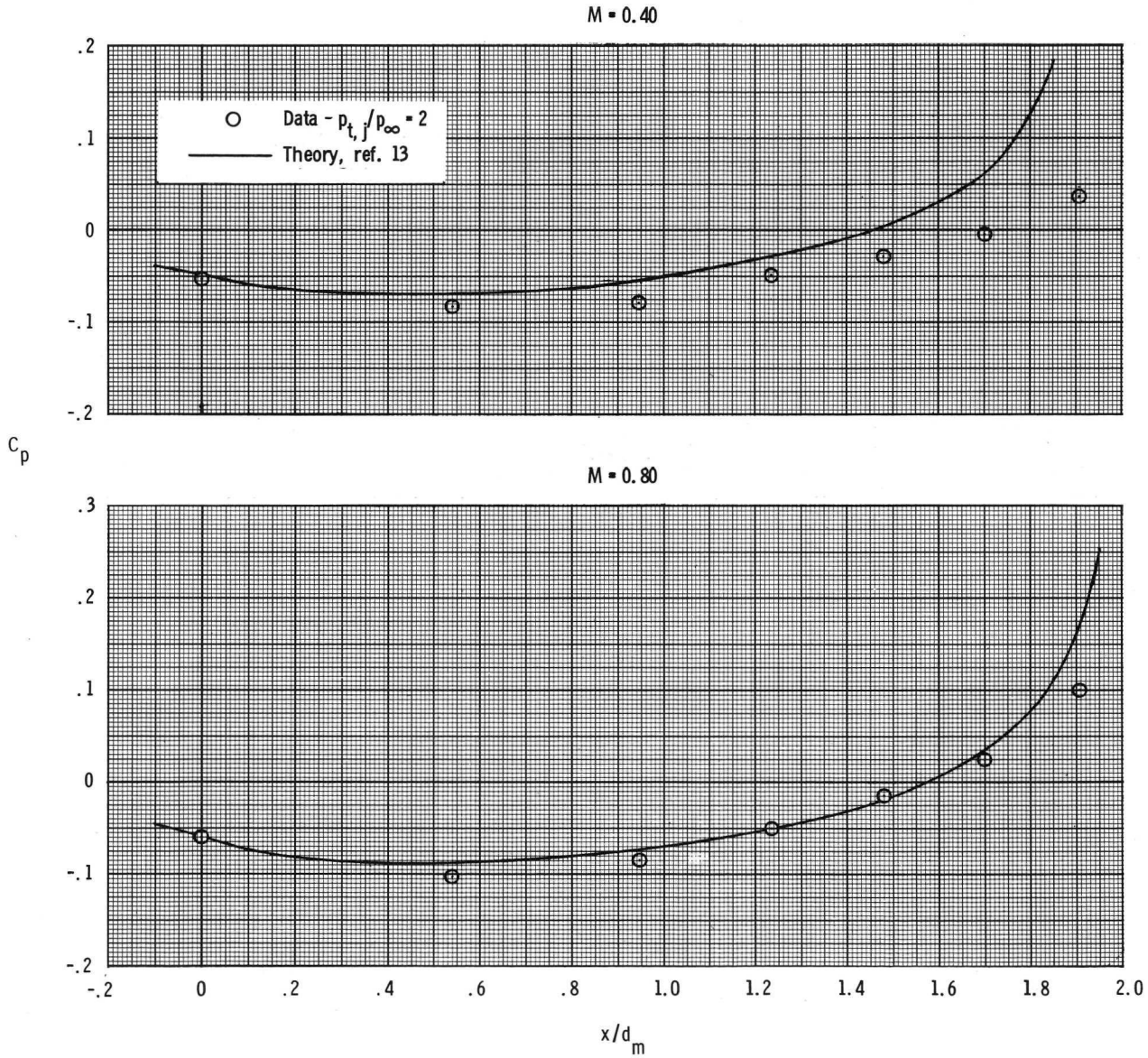
(a) Configuration 1 $\left(l/d_m = 1.0;\quad d_e/d_m = 0.6\right)$ and configuration 2 $\left(l/d_m = 1.5;\quad d_e/d_m = 0.6\right)$.

Figure 20.- Comparison of measured boattail pressure-coefficient distributions with those predicted by the theory of reference 13.



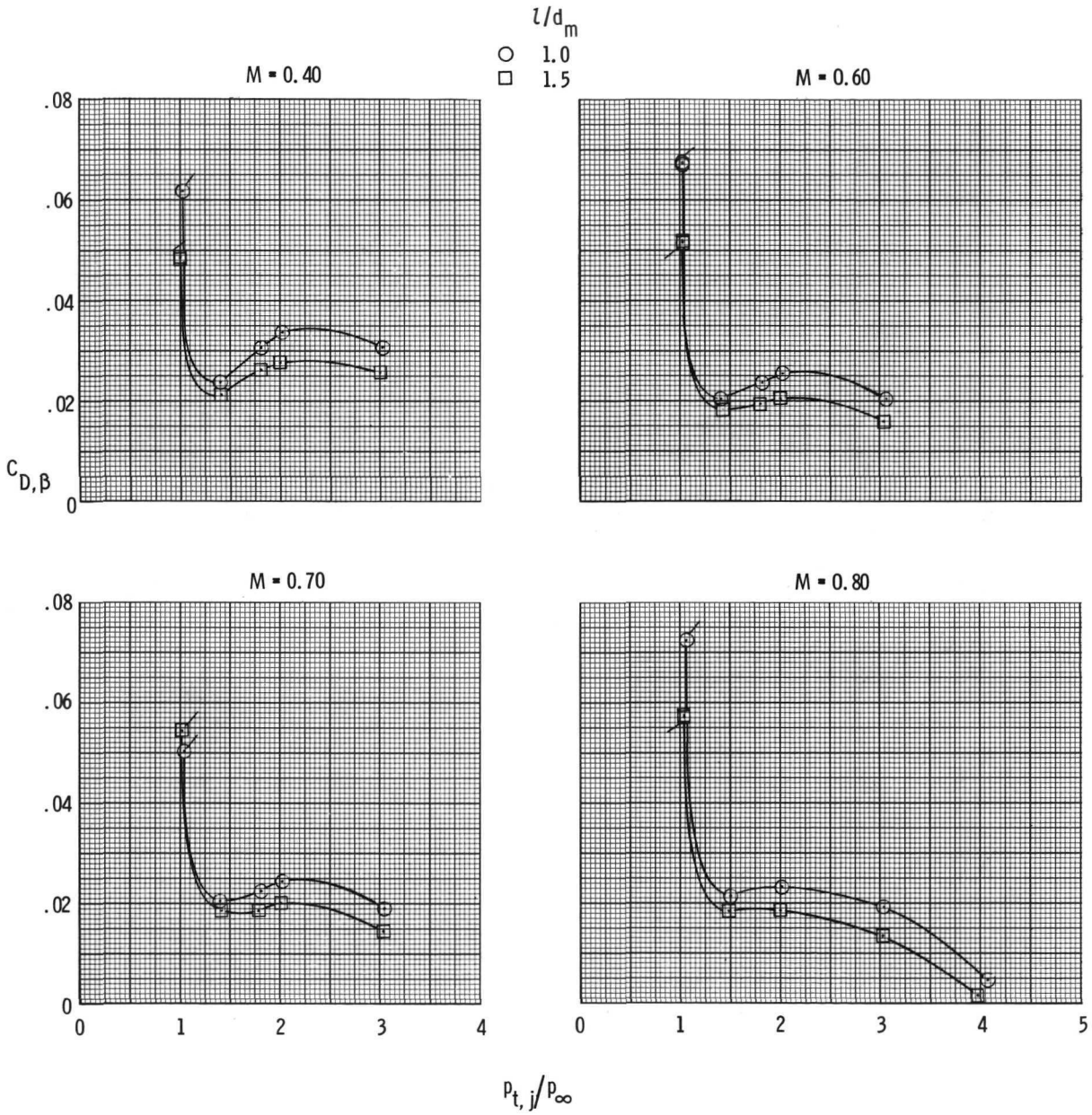
(b) Configuration 3 $\left(l/d_m = 1.0;\quad d_e/d_m = 0.7\right)$ and configuration 4 $\left(l/d_m = 1.5;\quad d_e/d_m = 0.7\right)$.

Figure 20.- Continued.



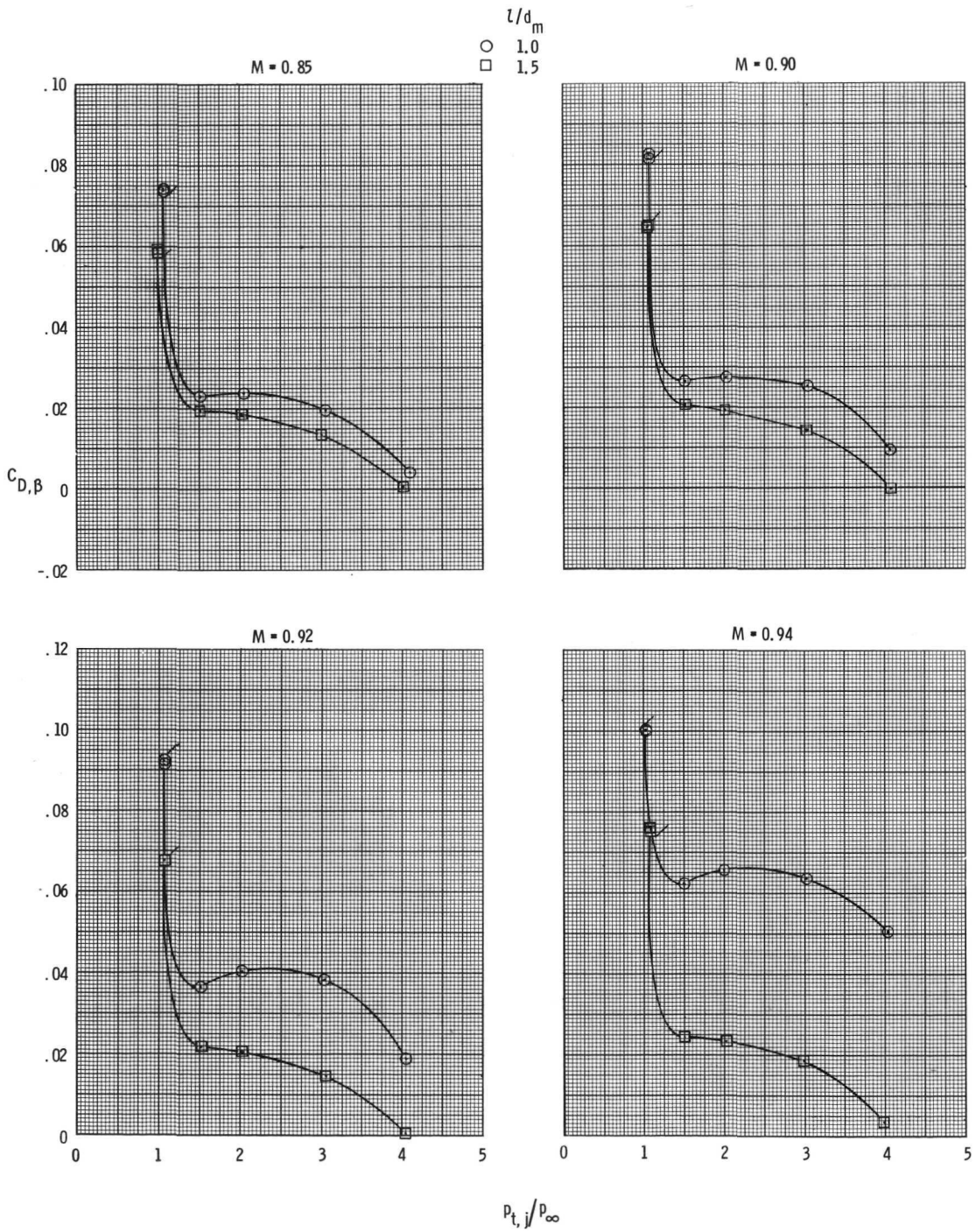
(c) Configuration 5 $(l/d_m = 2.0;\ \ d_e/d_m = 0.7)$.

Figure 20.- Concluded.



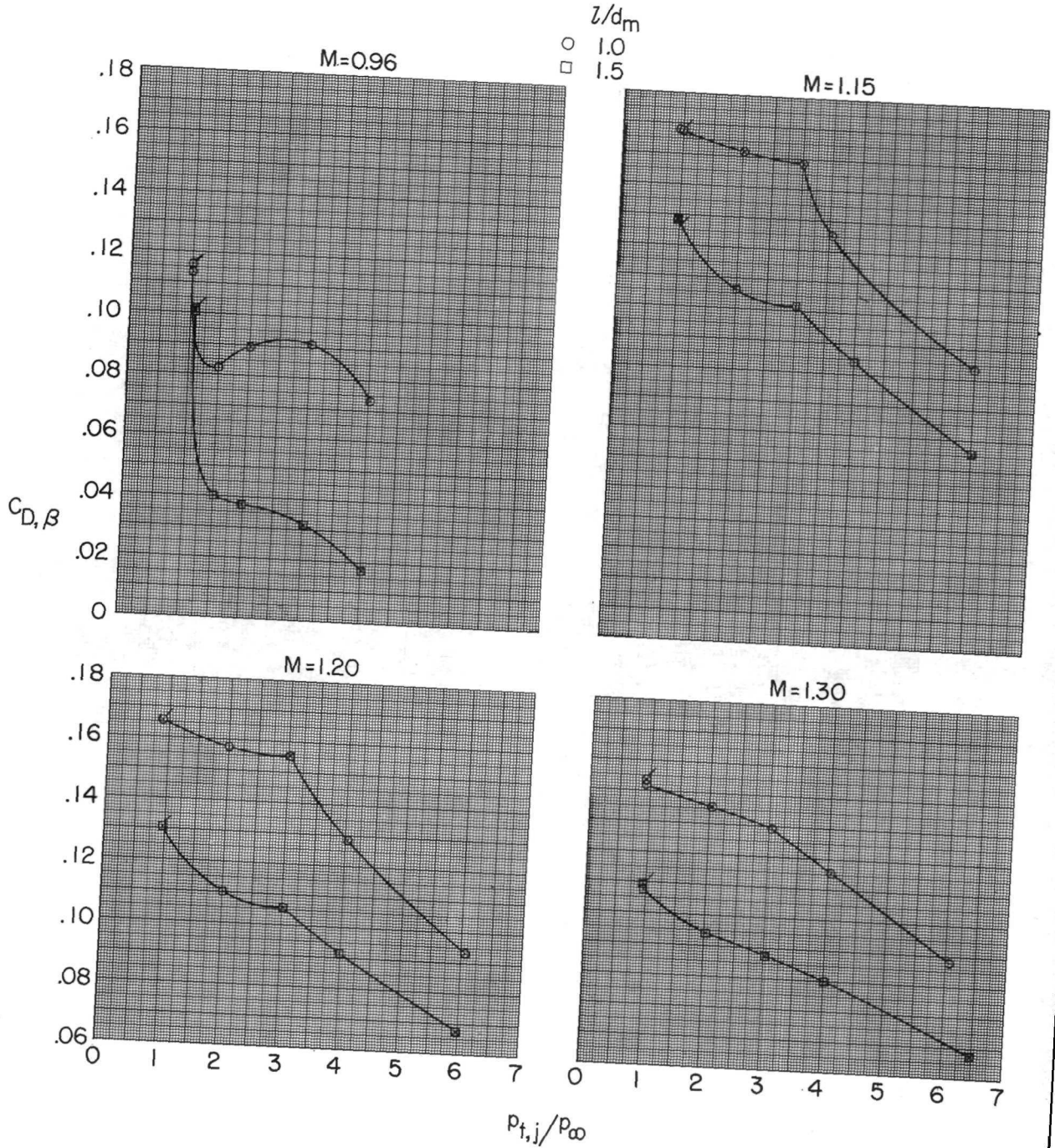
(a) M = 0.40, 0.60, 0.70, and 0.80.

Figure 21.- Effect of jet total-pressure ratio on boattail drag coefficients for configurations with $d_e/d_m = 0.6$.



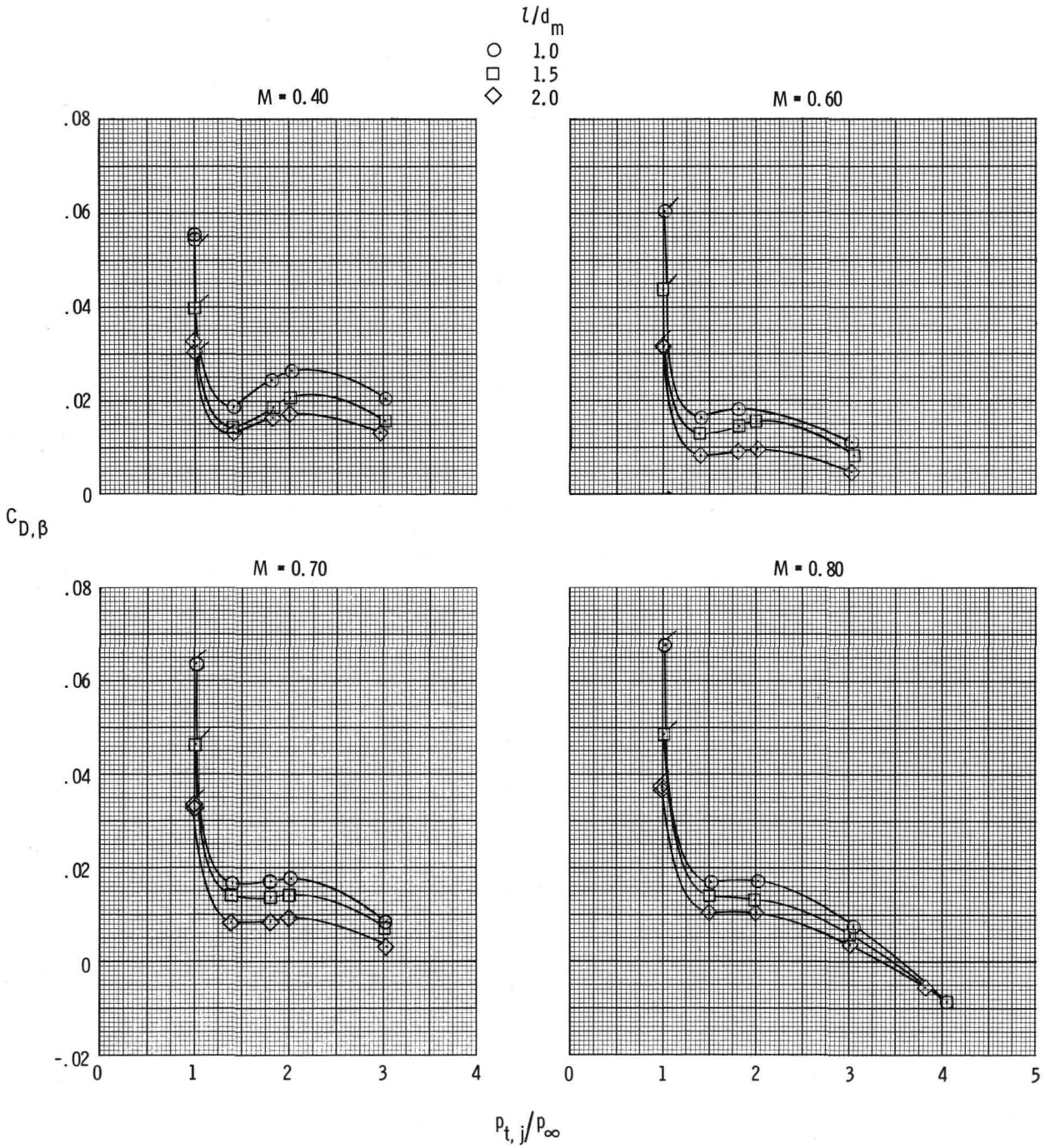
(b) M = 0.85, 0.90, 0.92, and 0.94.

Figure 21.- Continued.



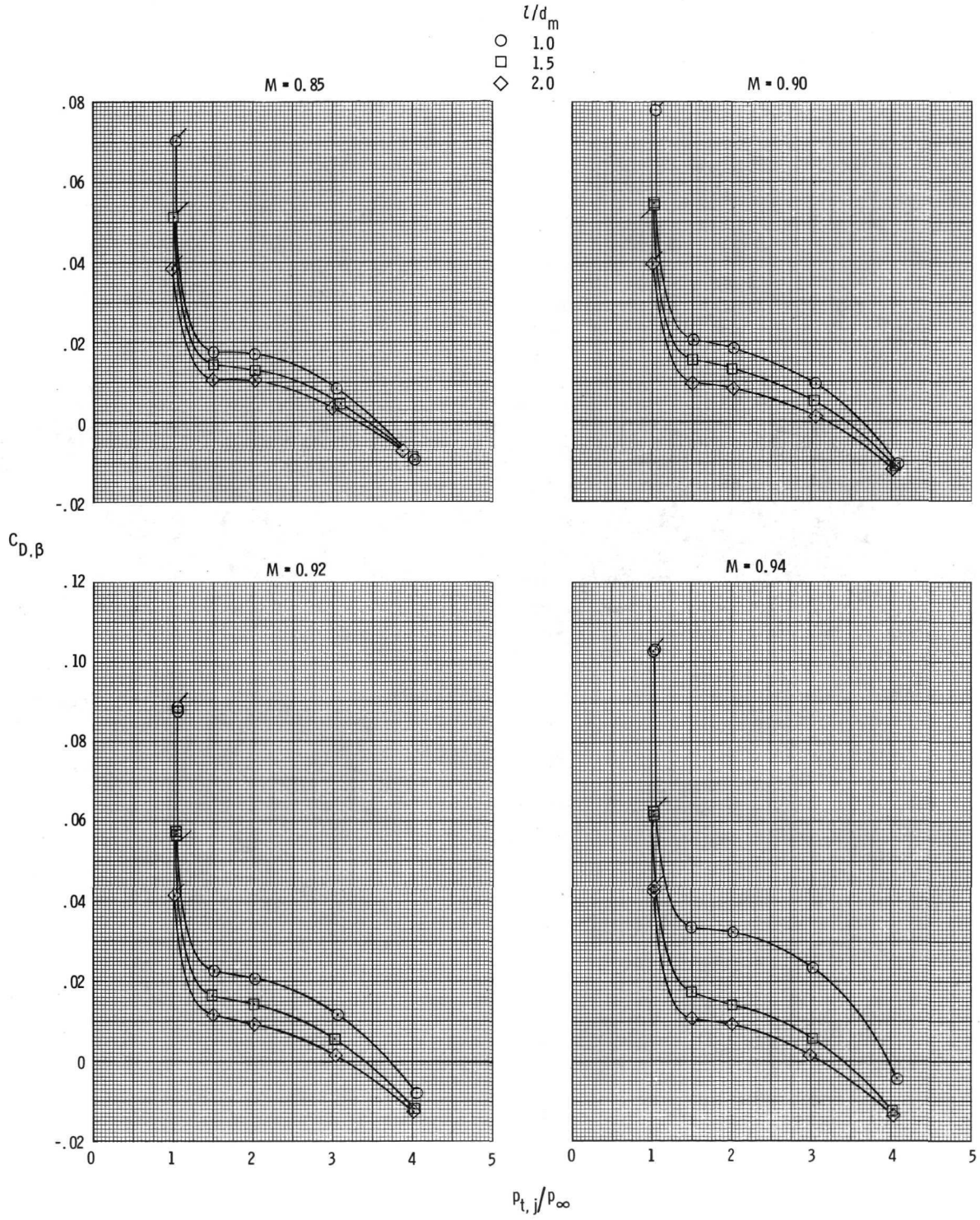
(c) M = 0.96, 1.15, 1.20, and 1.30.

Figure 21.- Concluded.



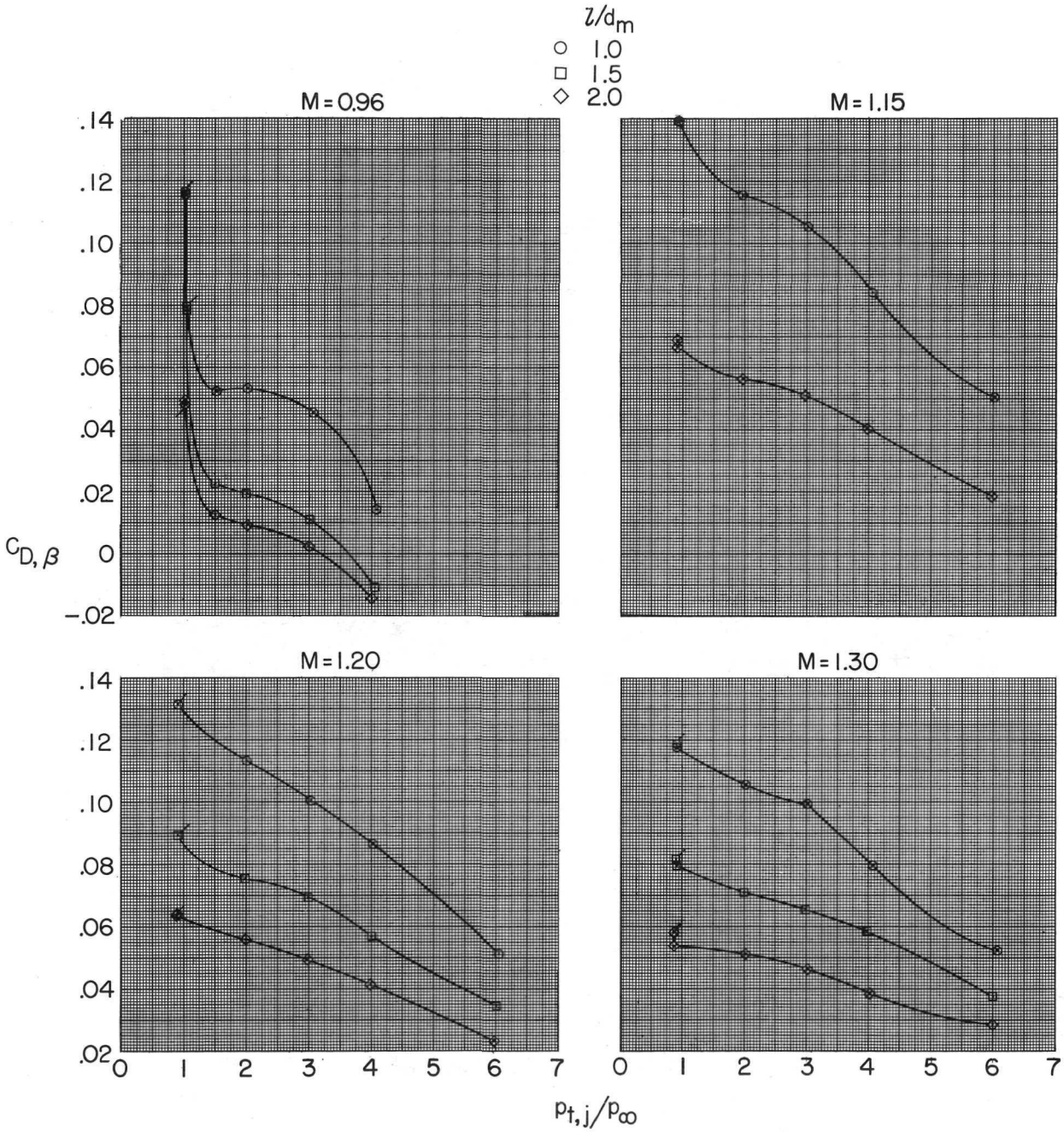
(a) M = 0.40, 0.60, 0.70, and 0.80.

Figure 22.- Effect of jet total-pressure ratio on boattail drag coefficients for configurations with $d_e/d_m = 0.7$.



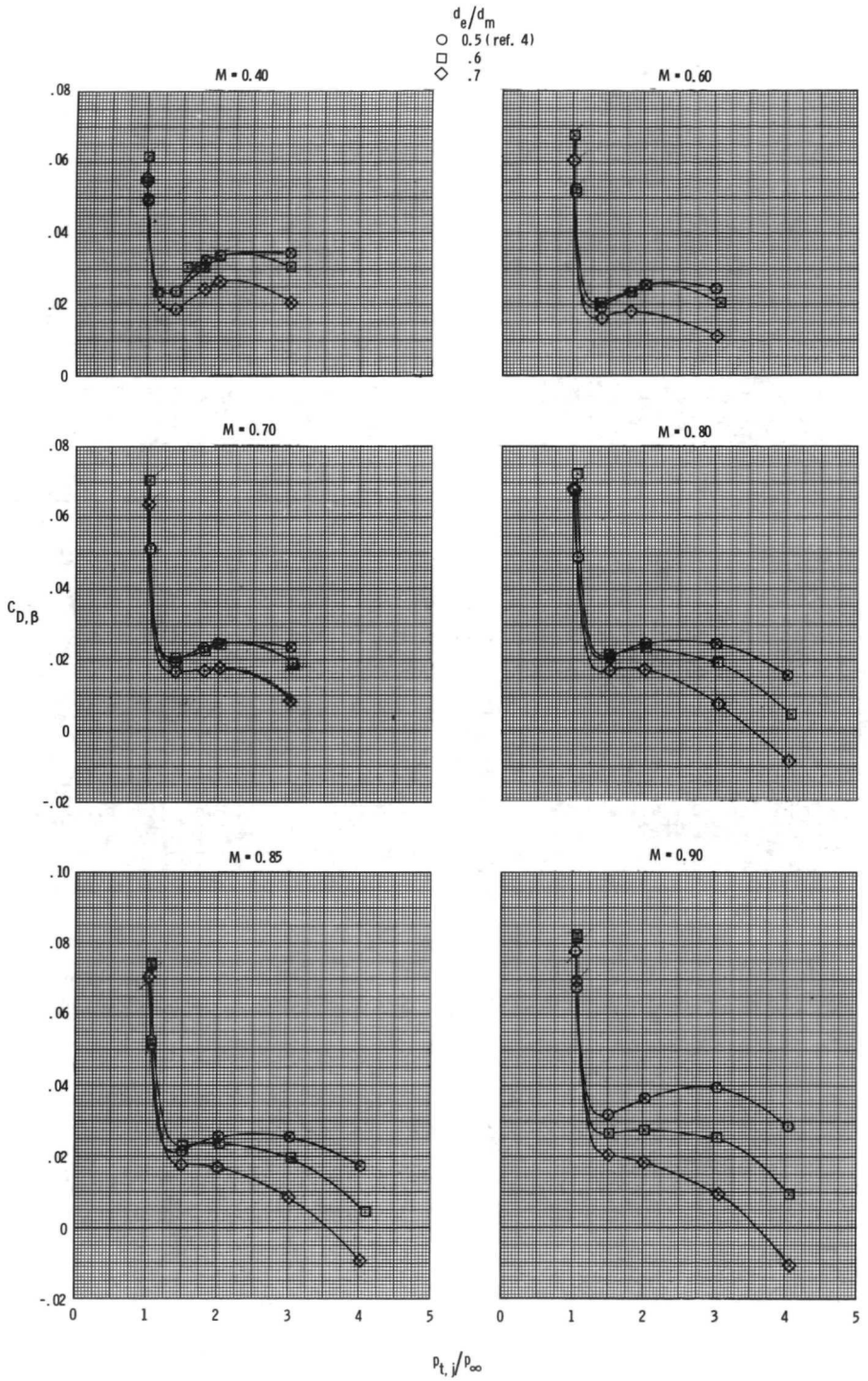
(b) M = 0.85, 0.90, 0.92, and 0.94.

Figure 22.- Continued.



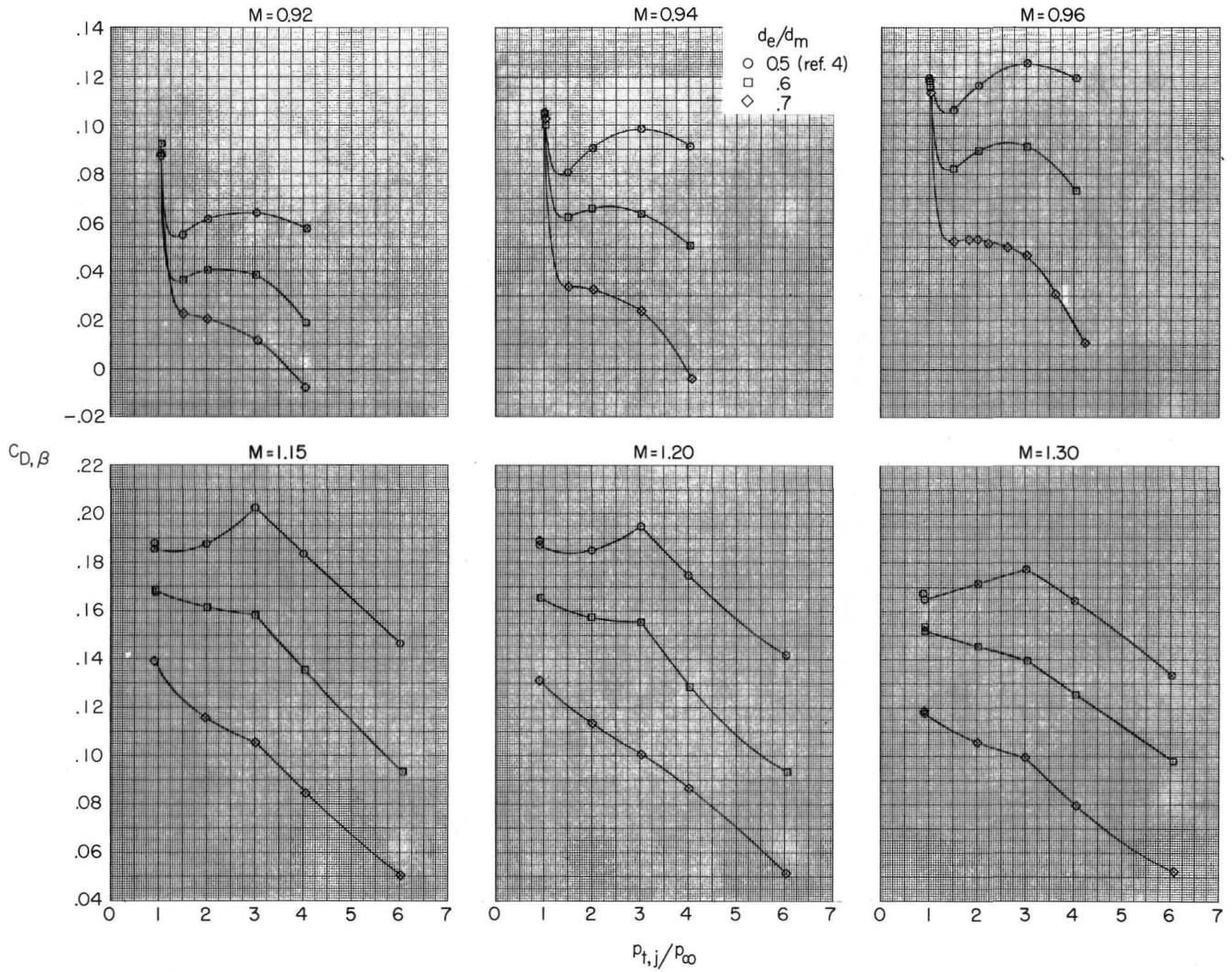
(c) M = 0.96, 1.15, 1.20, and 1.30.

Figure 22.- Concluded.



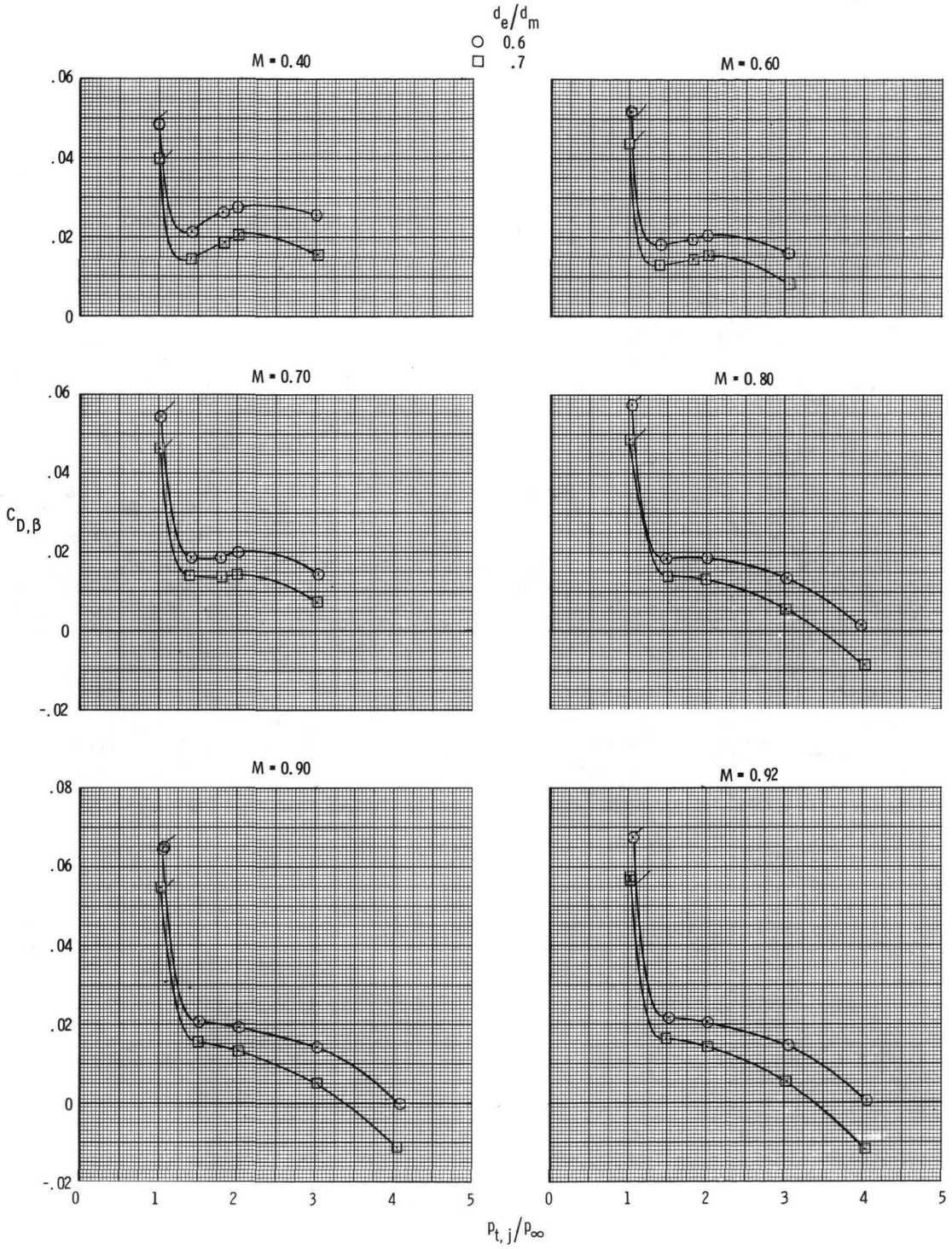
(a) M = 0.40, 0.60, 0.70, 0.80, 0.85, and 0.90.

Figure 23.- Effect of jet total-pressure ratio on boattail drag coefficients for configurations with $l/d_m = 1.0$.



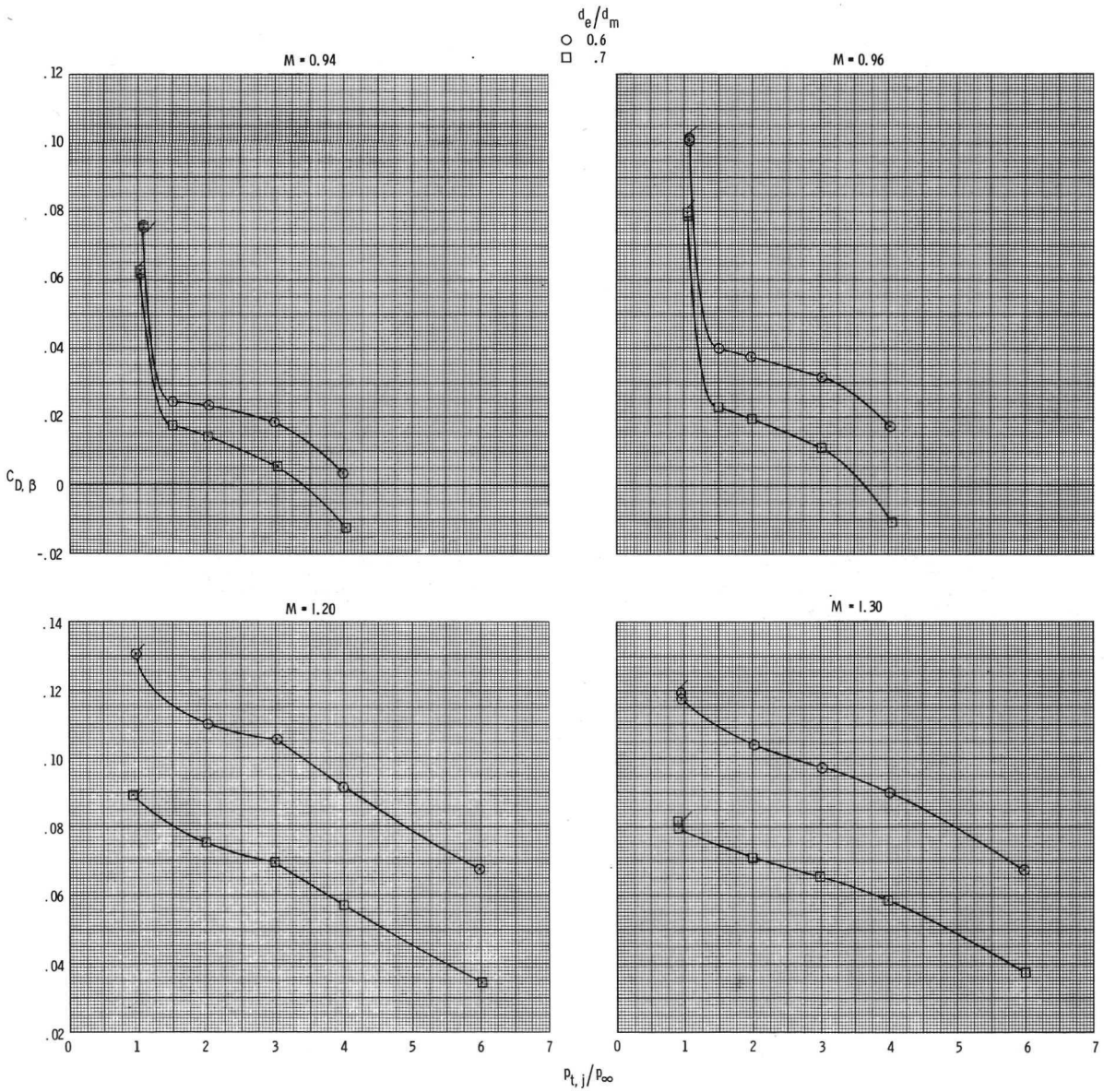
(b) M = 0.92, 0.94, 0.96, 1.15, 1.20, and 1.30.

Figure 23.- Concluded.



(a) M = 0.40, 0.60, 0.70, 0.80, 0.90, and 0.92.

Figure 24.- Effect of jet total-pressure ratio on boattail drag coefficients for configurations with $l/d_m = 1.5$.



(b) M = 0.94, 0.96, 1.20, and 1.30.

Figure 24.- Concluded.

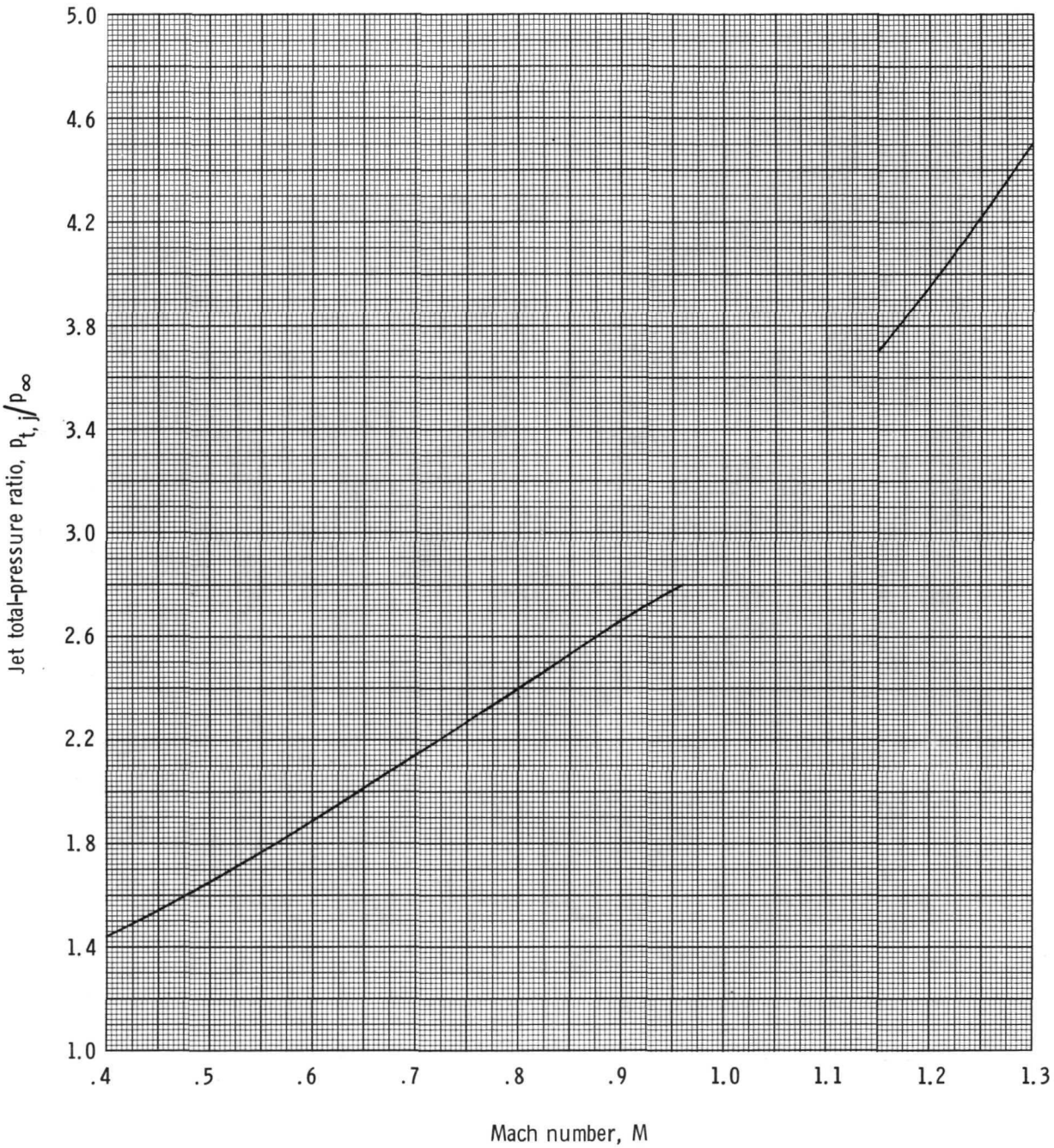


Figure 25.- Jet total-pressure ratio variation with Mach number for a typical turbofan engine.

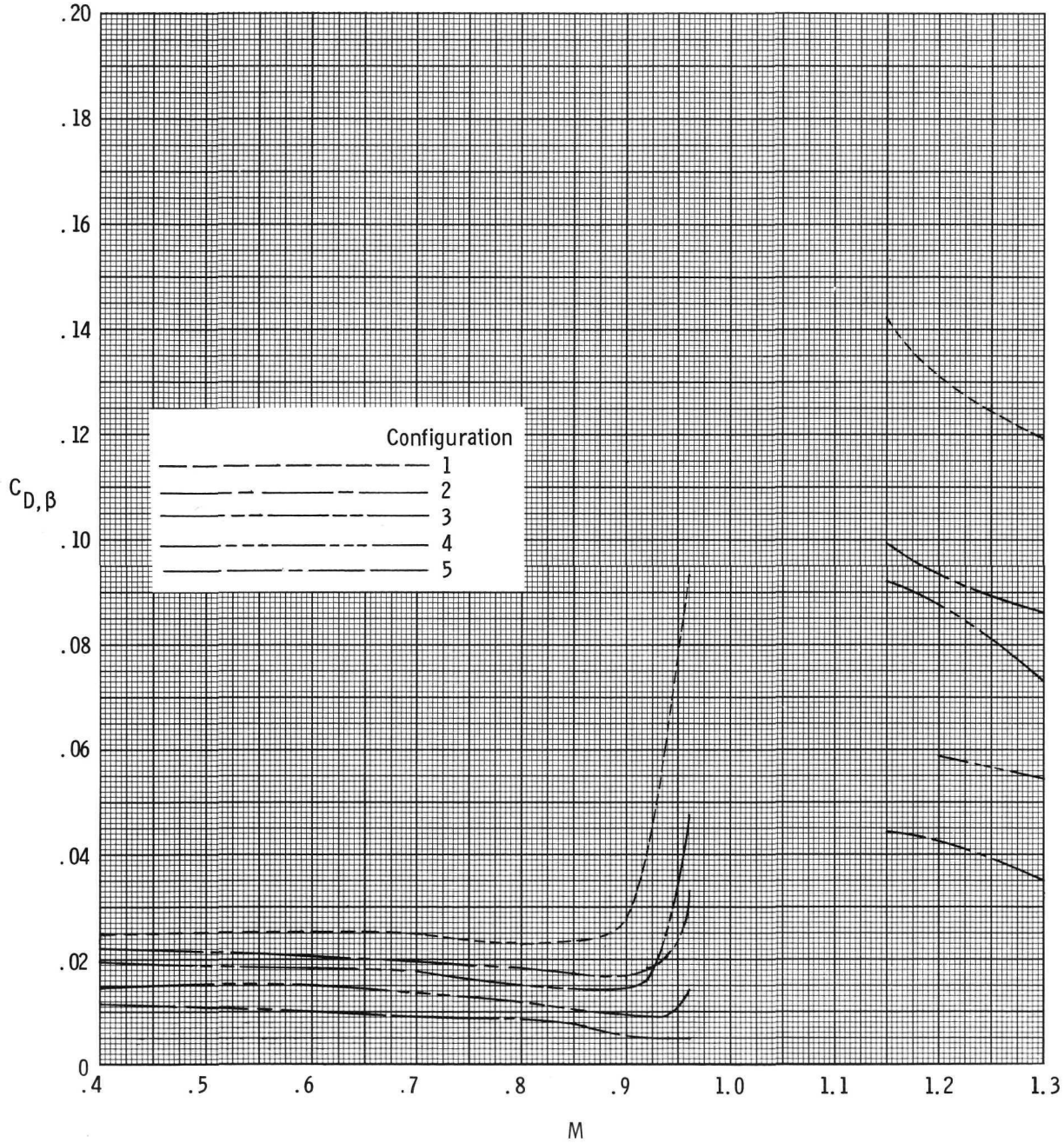


Figure 26.- Variation of boattail pressure-drag coefficients with Mach number for all configurations at the jet-total-pressure-ratio schedule of figure 25.

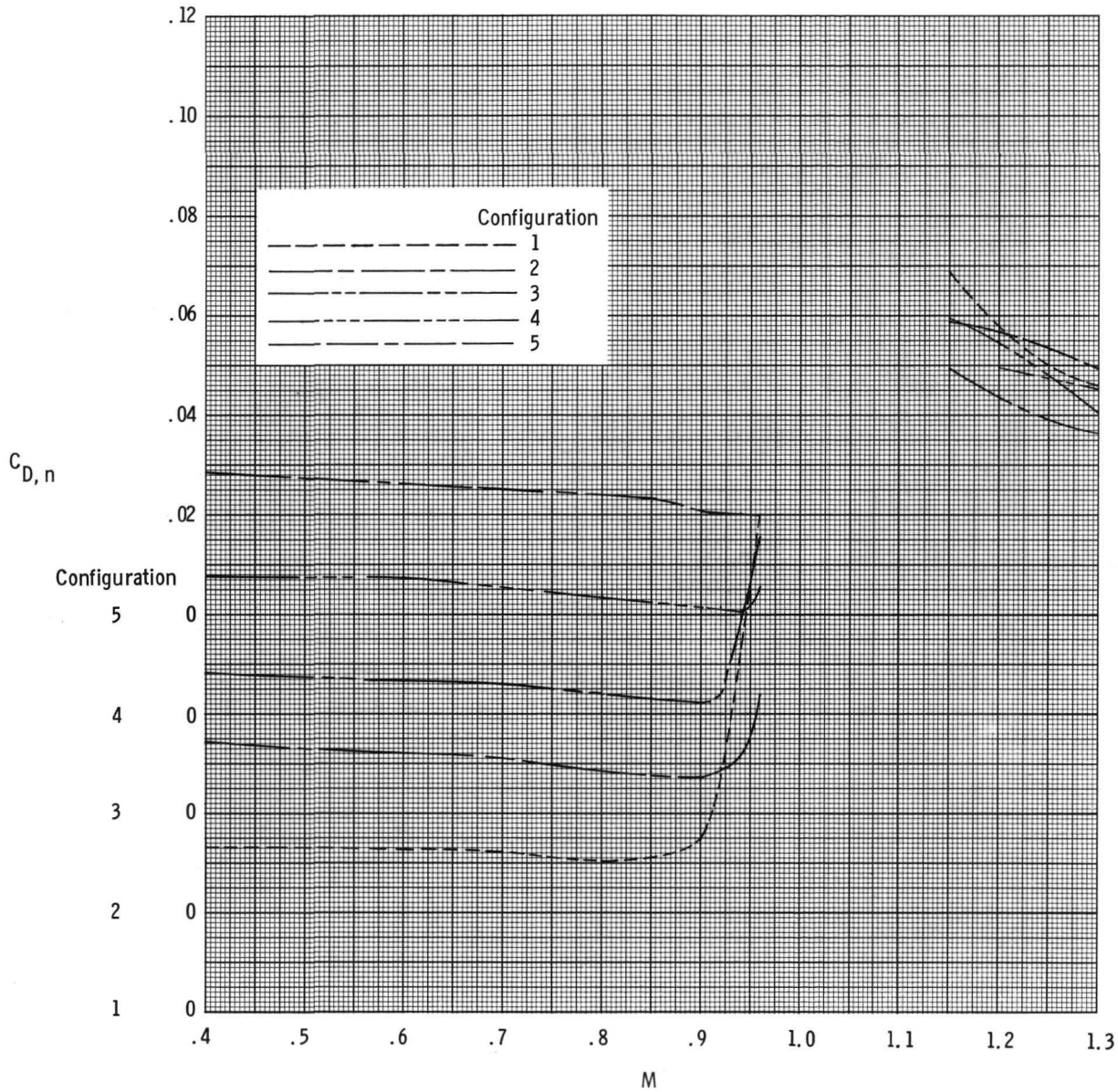
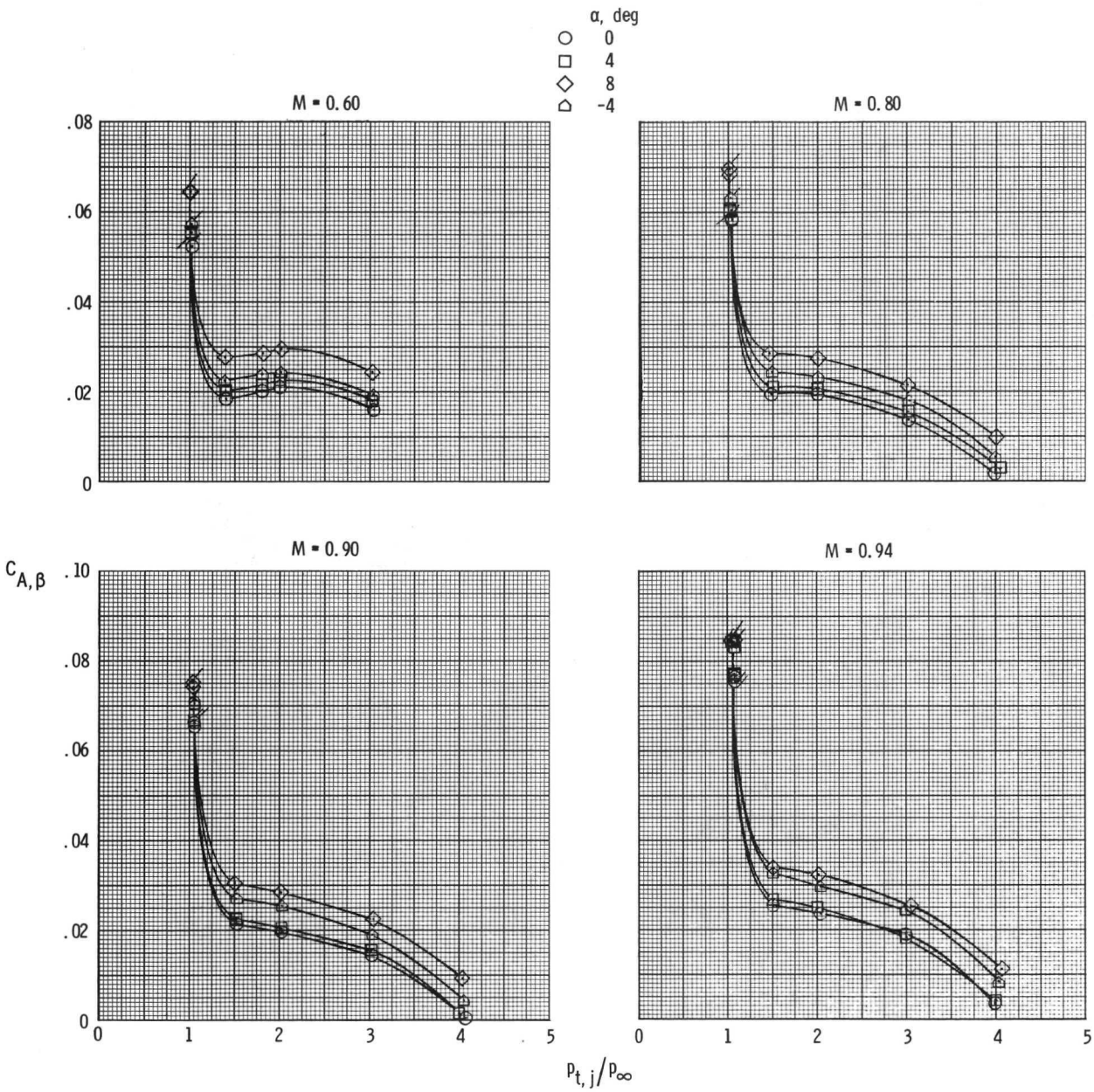
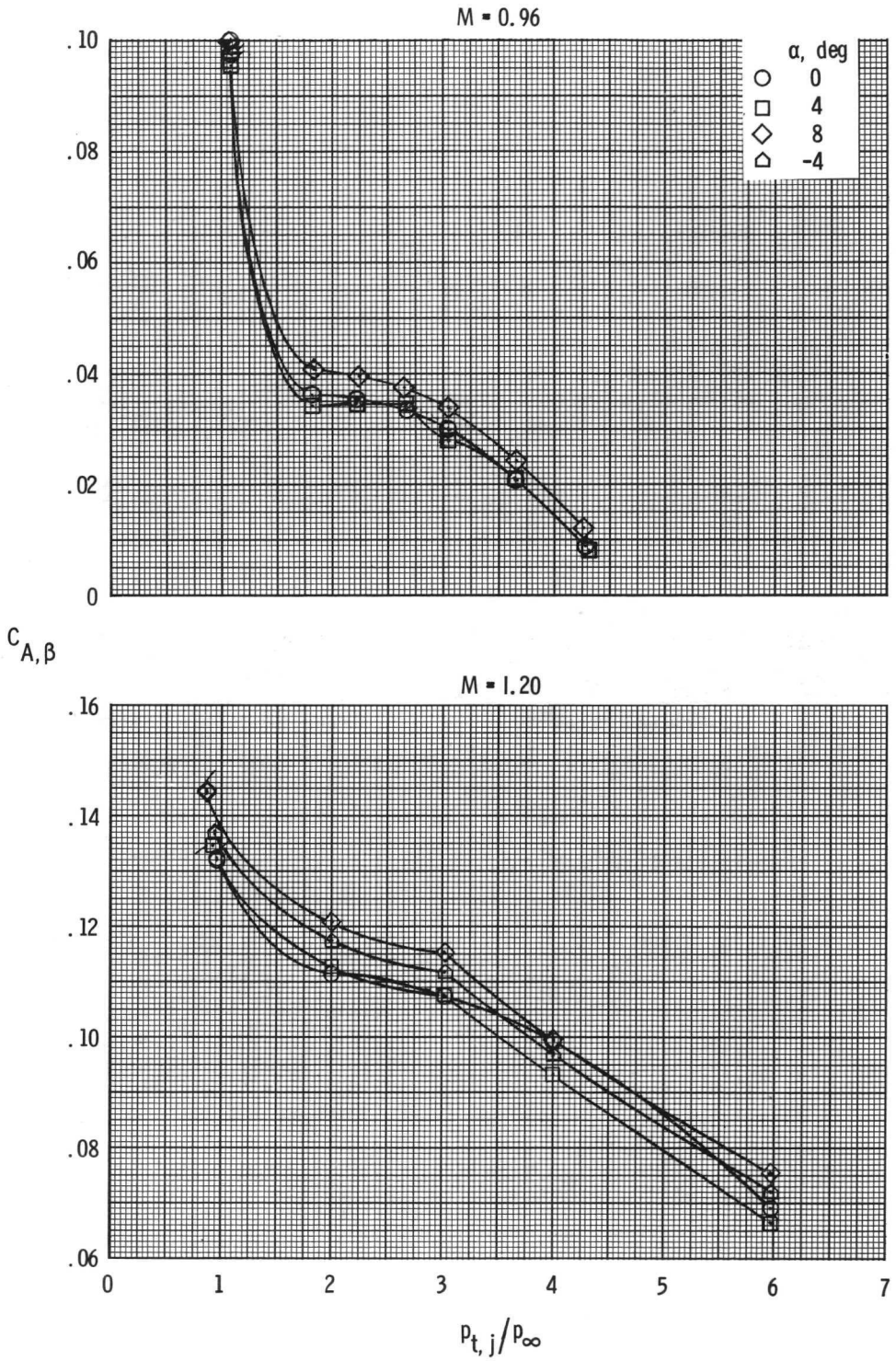


Figure 27.- Variation of afterbody total-drag coefficients with Mach number for all configurations at the jet-total-pressure-ratio schedule of figure 25.



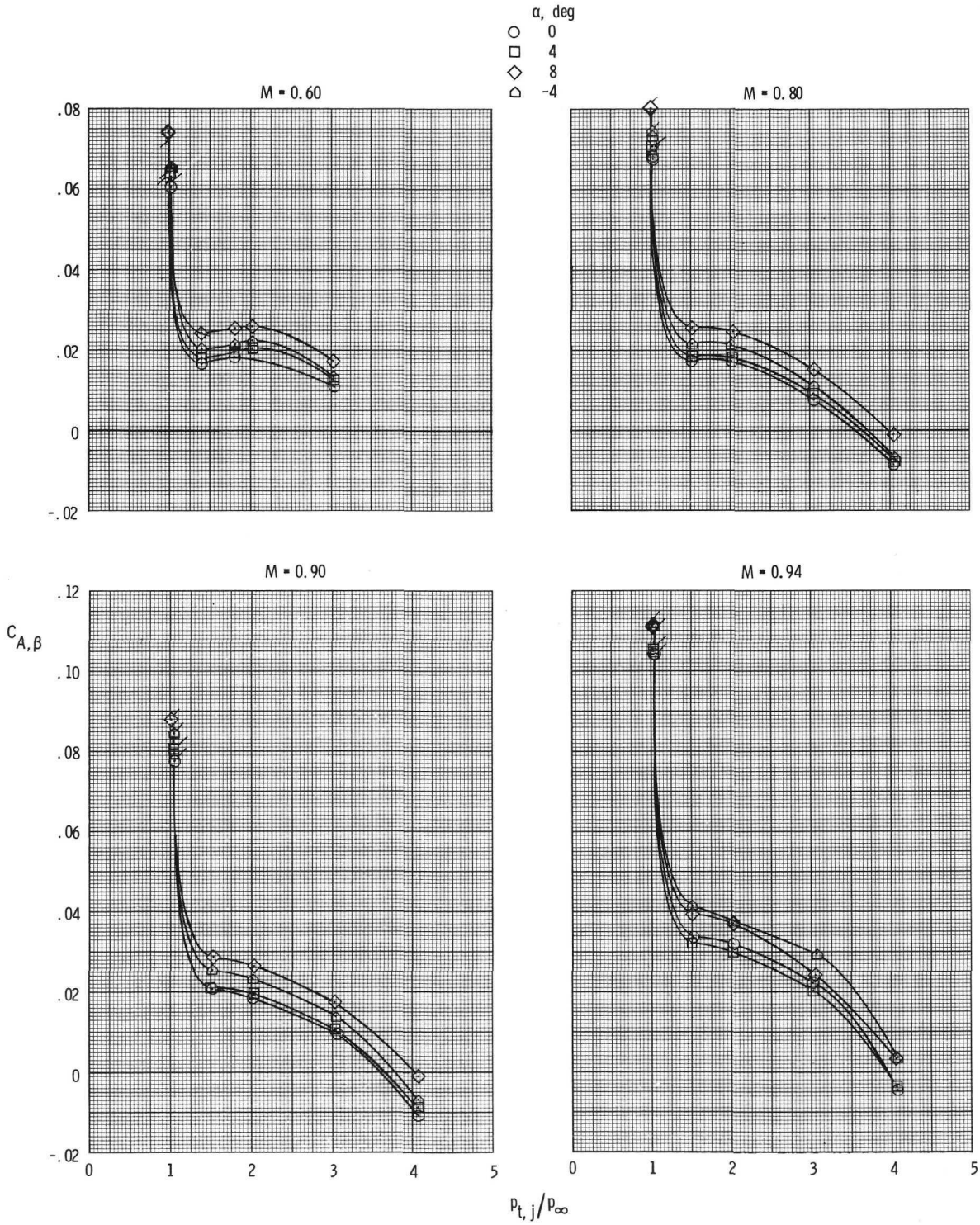
(a) M = 0.60, 0.80, 0.90, and 0.94.

Figure 28.- Effects of jet total-pressure ratio and angle of attack on the boattail axial-force coefficients of configuration 2 $\left(l/d_m = 1.5;\ d_e/d_m = 0.6\right)$.



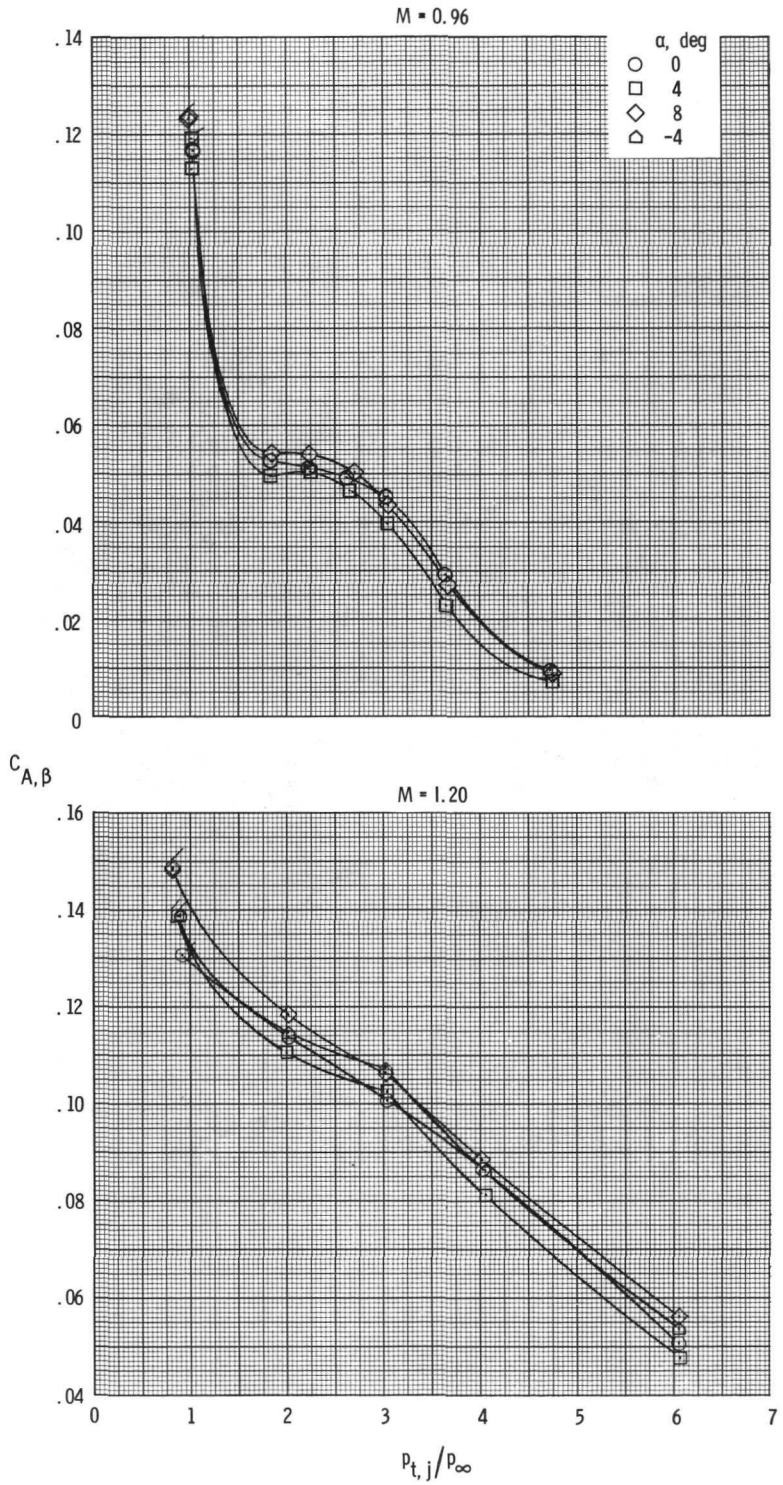
(b) M = 0.96 and 1.20.

Figure 28.- Concluded.



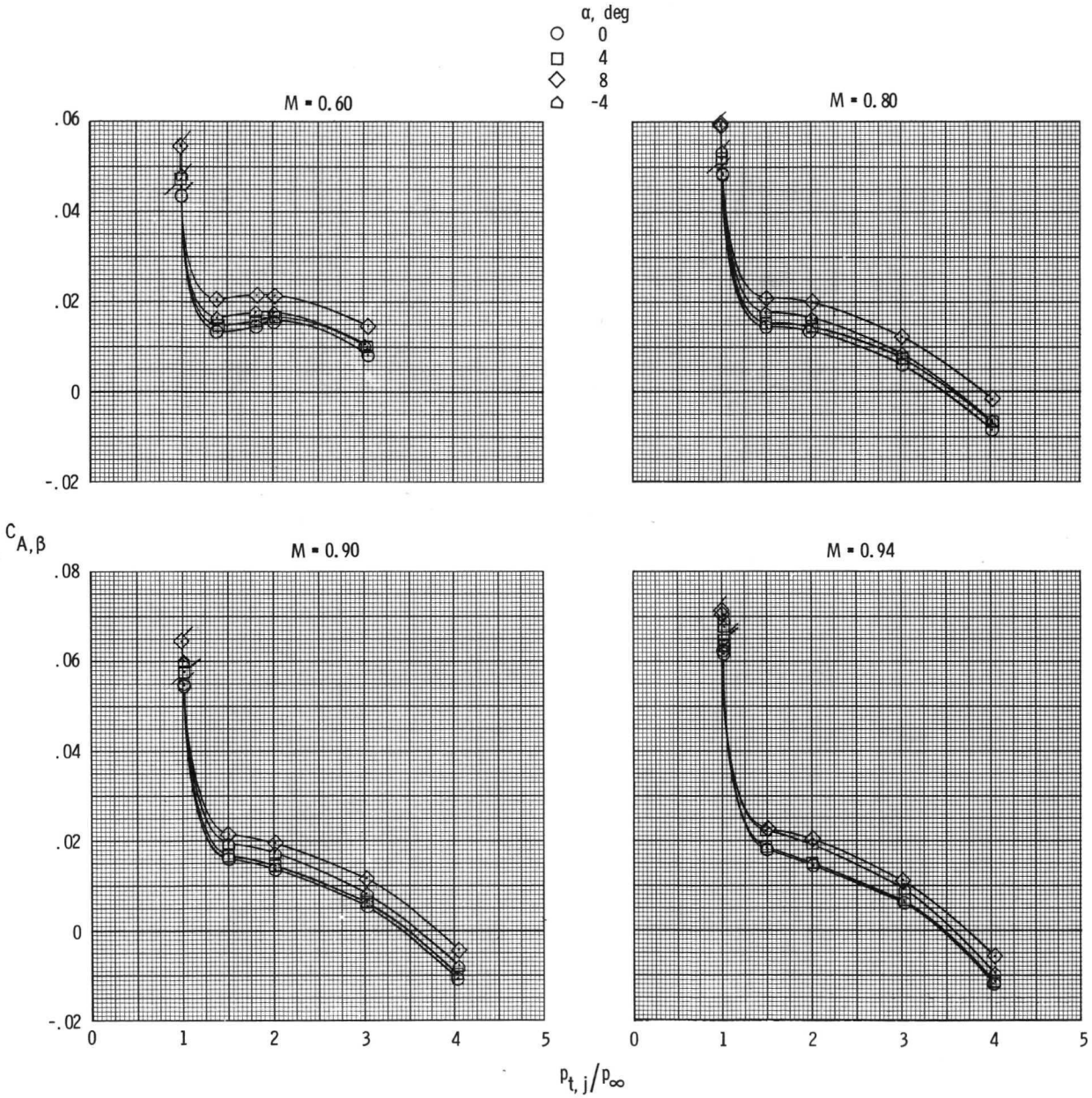
(a) M = 0.60, 0.80, 0.90, and 0.94.

Figure 29.- Effects of jet total-pressure ratio and angle of attack on the boattail axial-force coefficients of configuration 3 $\left(l/d_m = 1.0;\quad d_e/d_m = 0.7\right)$.



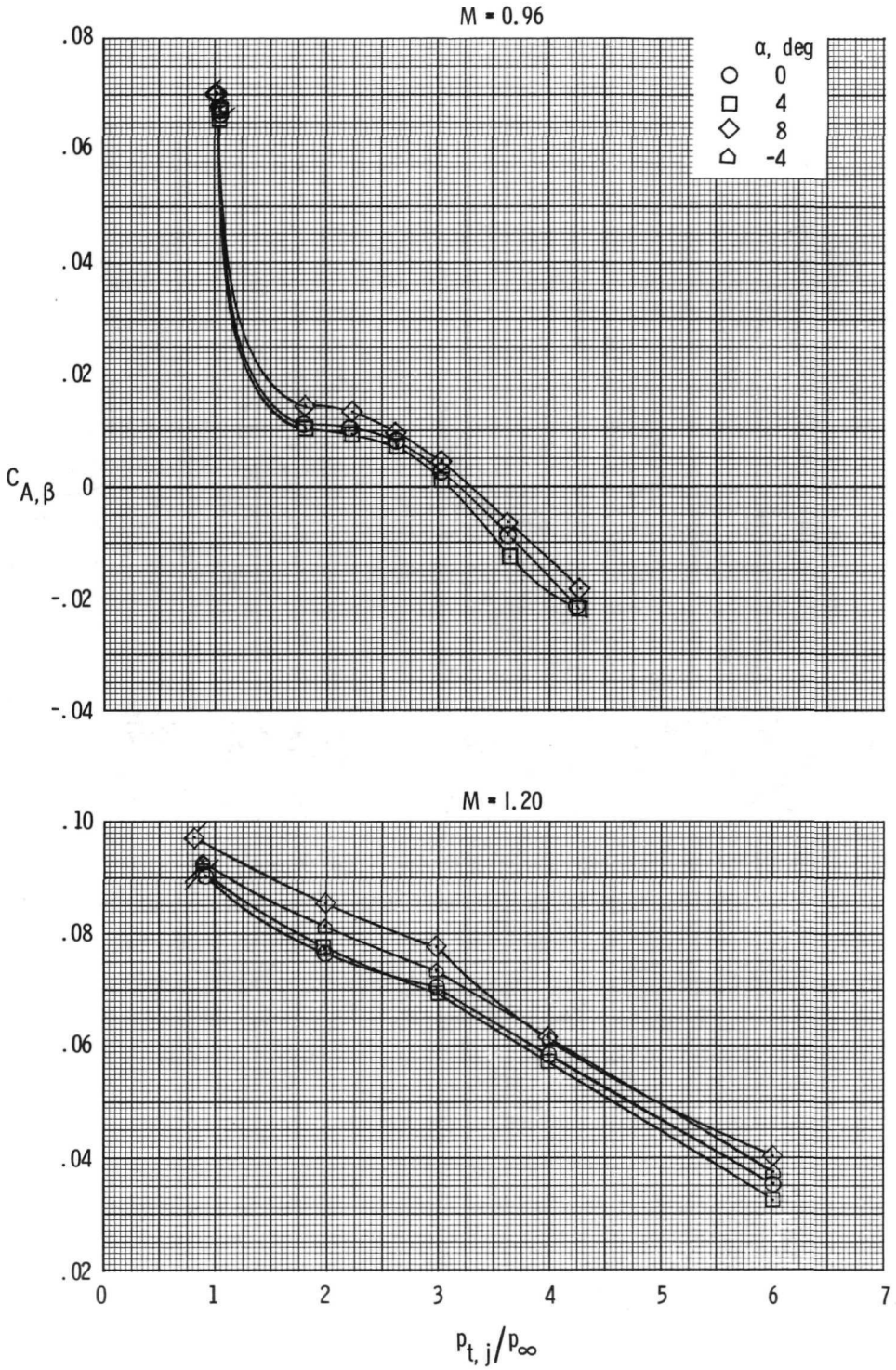
(b) M = 0.96 and 1.20.

Figure 29.- Concluded.



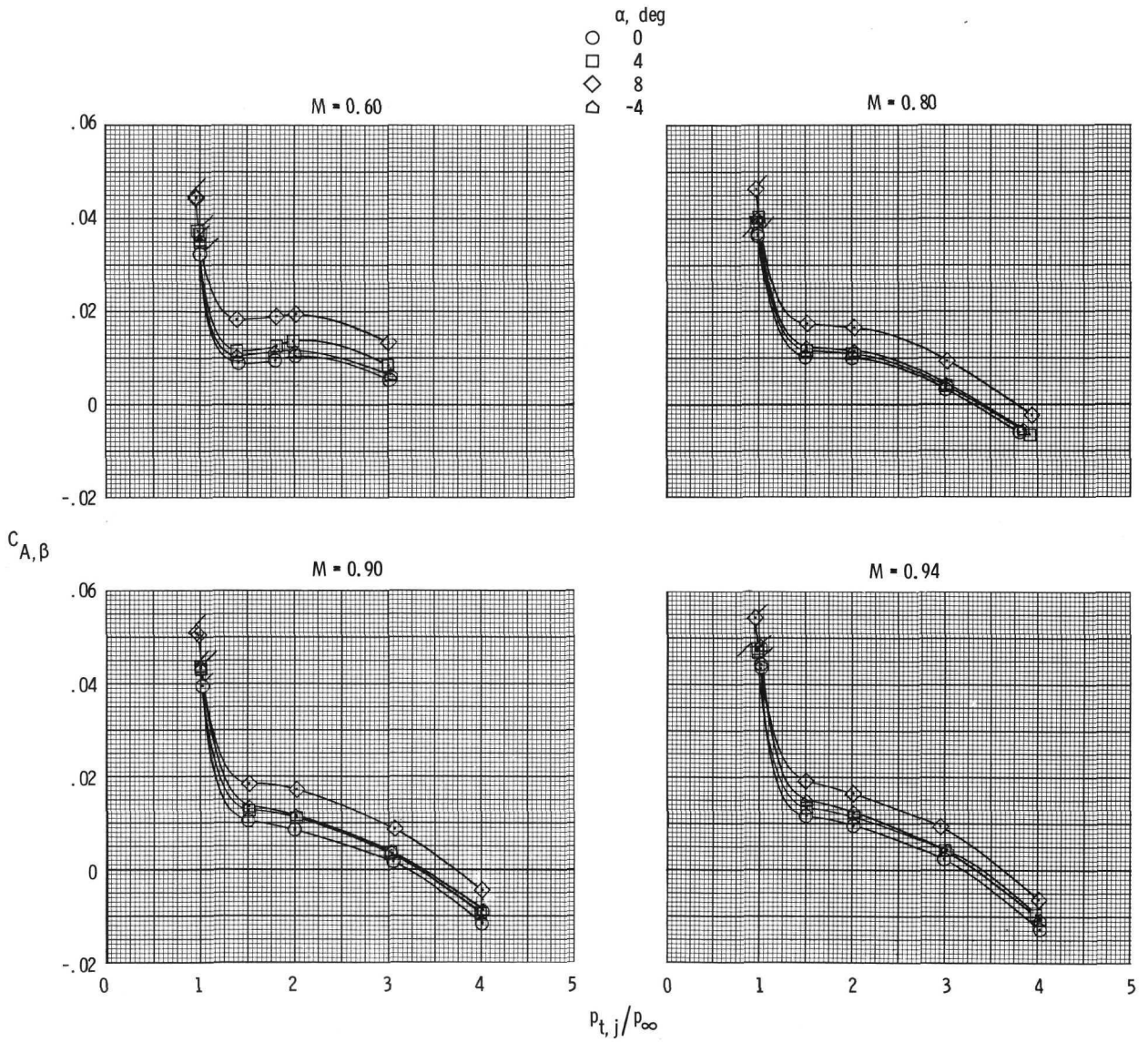
(a) M = 0.60, 0.80, 0.90, and 0.94.

Figure 30.- Effects of jet total-pressure ratio and angle of attack on the boattail axial-force coefficients of configuration 4 $\left(\ell/d_m = 1.5;\ d_e/d_m = 0.7\right)$.



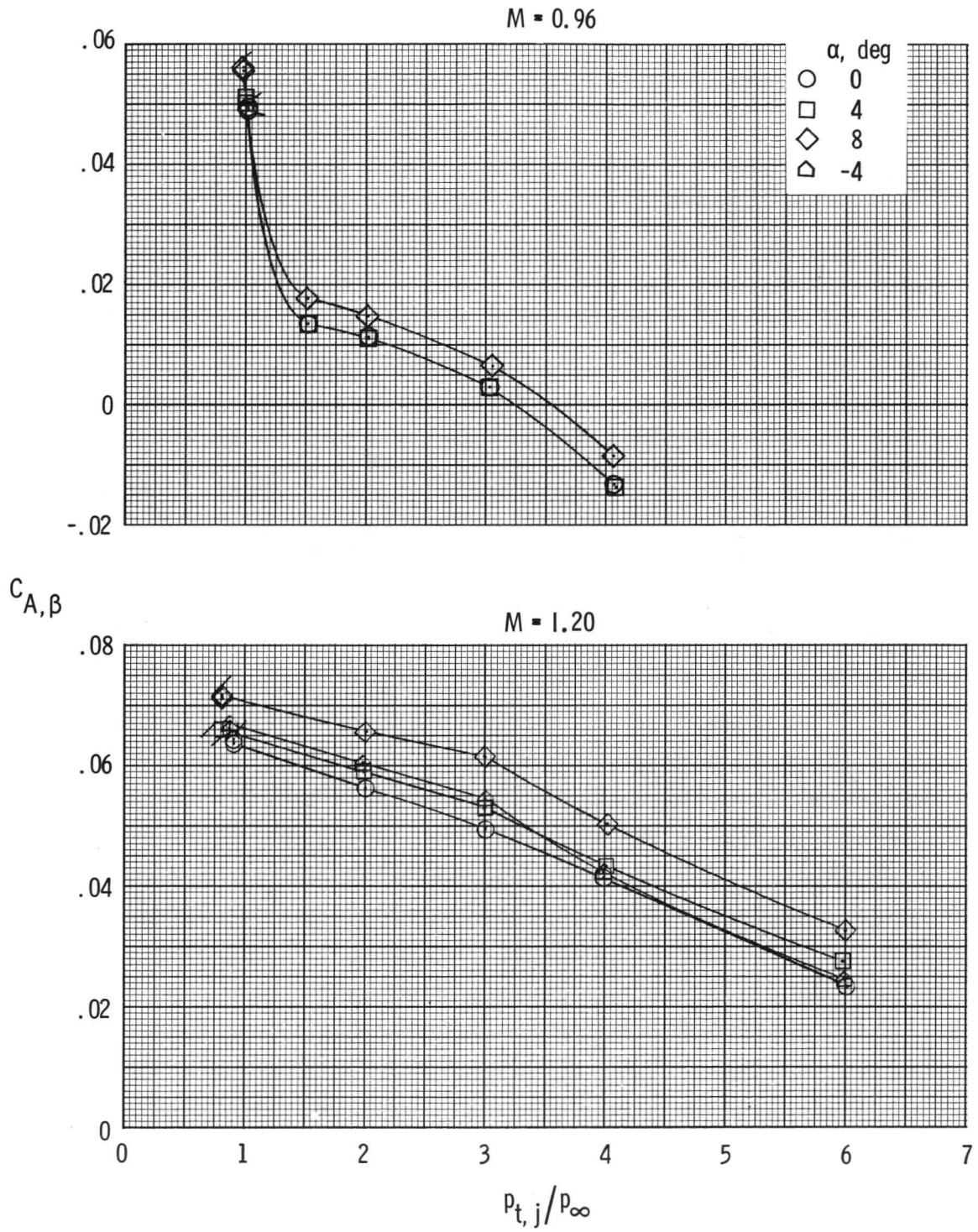
(b) M = 0.96 and 1.20.

Figure 30.- Concluded.



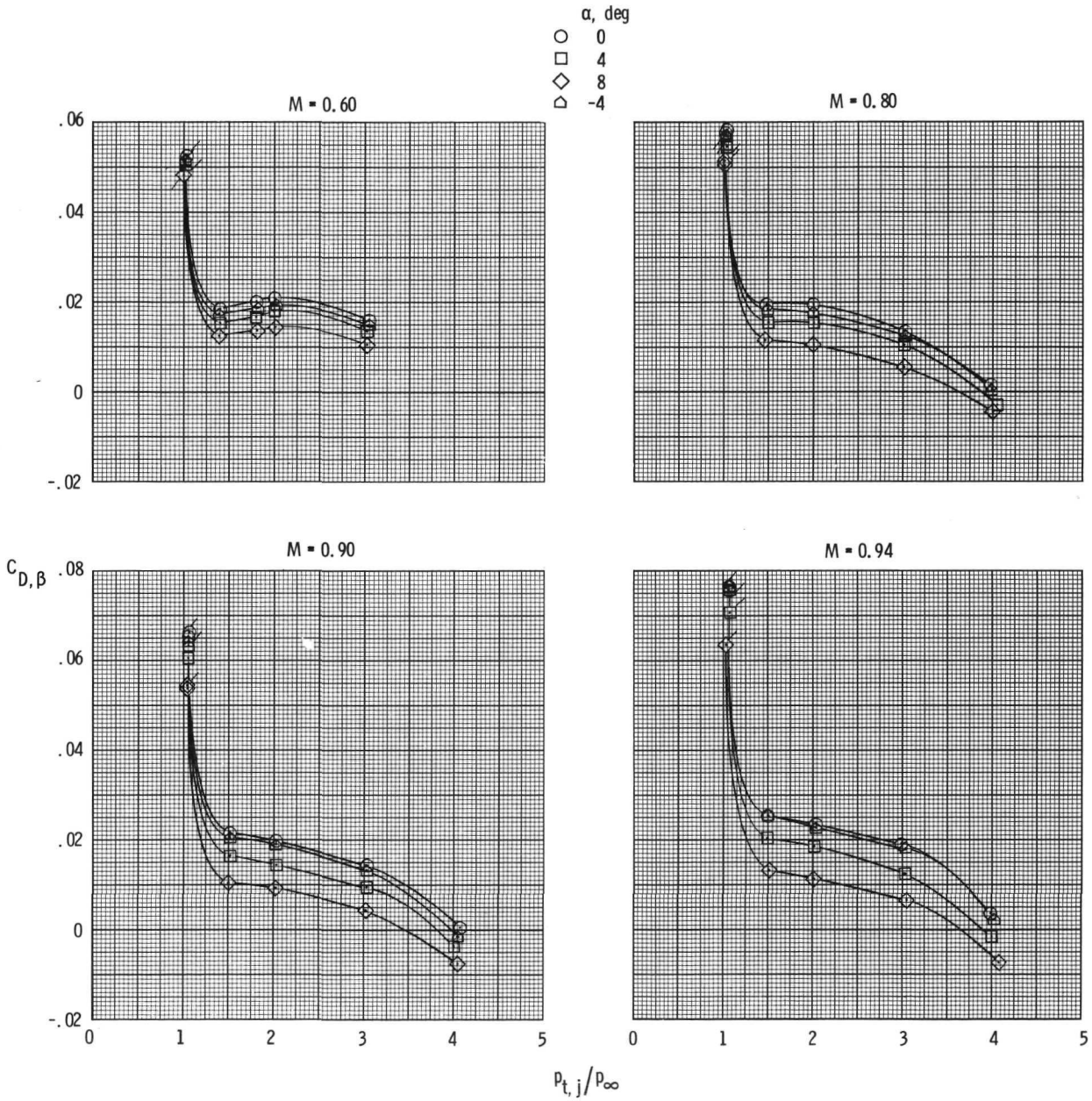
(a) M = 0.60, 0.80, 0.90, and 0.94.

Figure 31.- Effects of jet total-pressure ratio and angle of attack on the boattail axial-force coefficients of configuration 5 $\left(l/d_m = 2.0;\ d_e/d_m = 0.7\right)$.



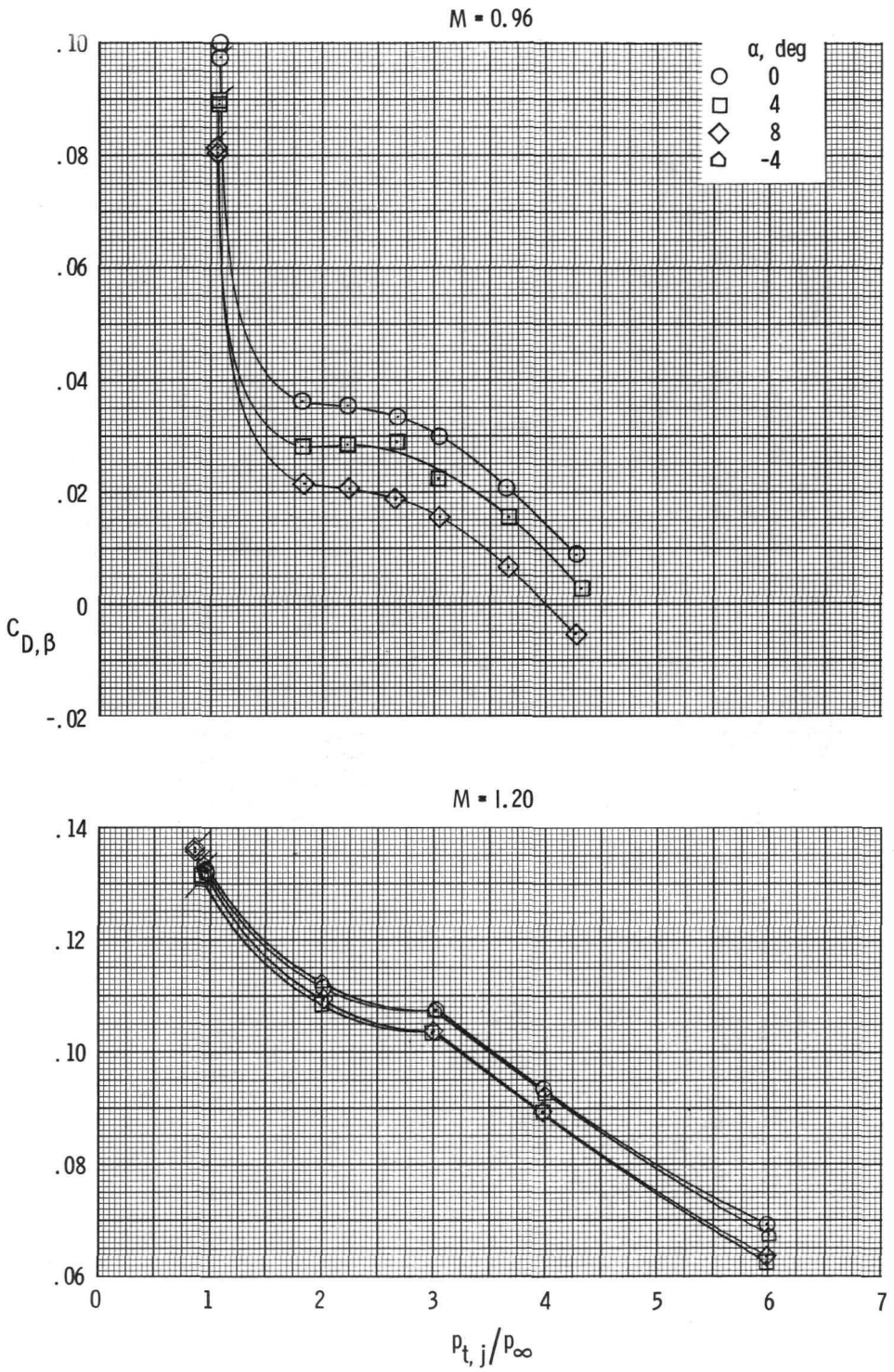
(b) M = 0.96 and 1.20.

Figure 31.- Concluded.



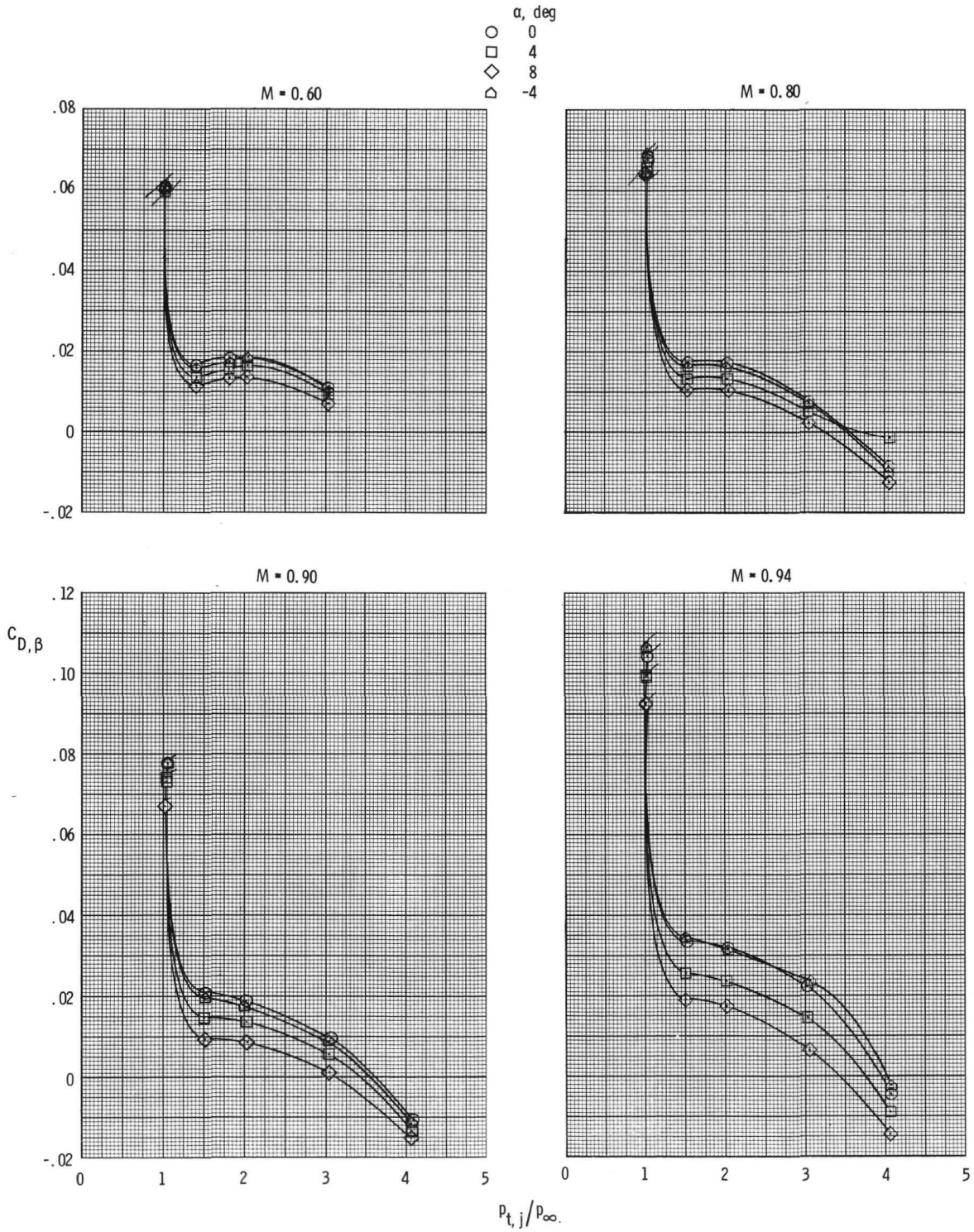
(a) M = 0.60, 0.80, 0.90, and 0.94.

Figure 32.- Effects of jet total-pressure ratio and angle of attack on the boattail drag coefficients of configuration 2 $\left(\ell/d_m = 1.5;\ d_e/d_m = 0.6\right)$.



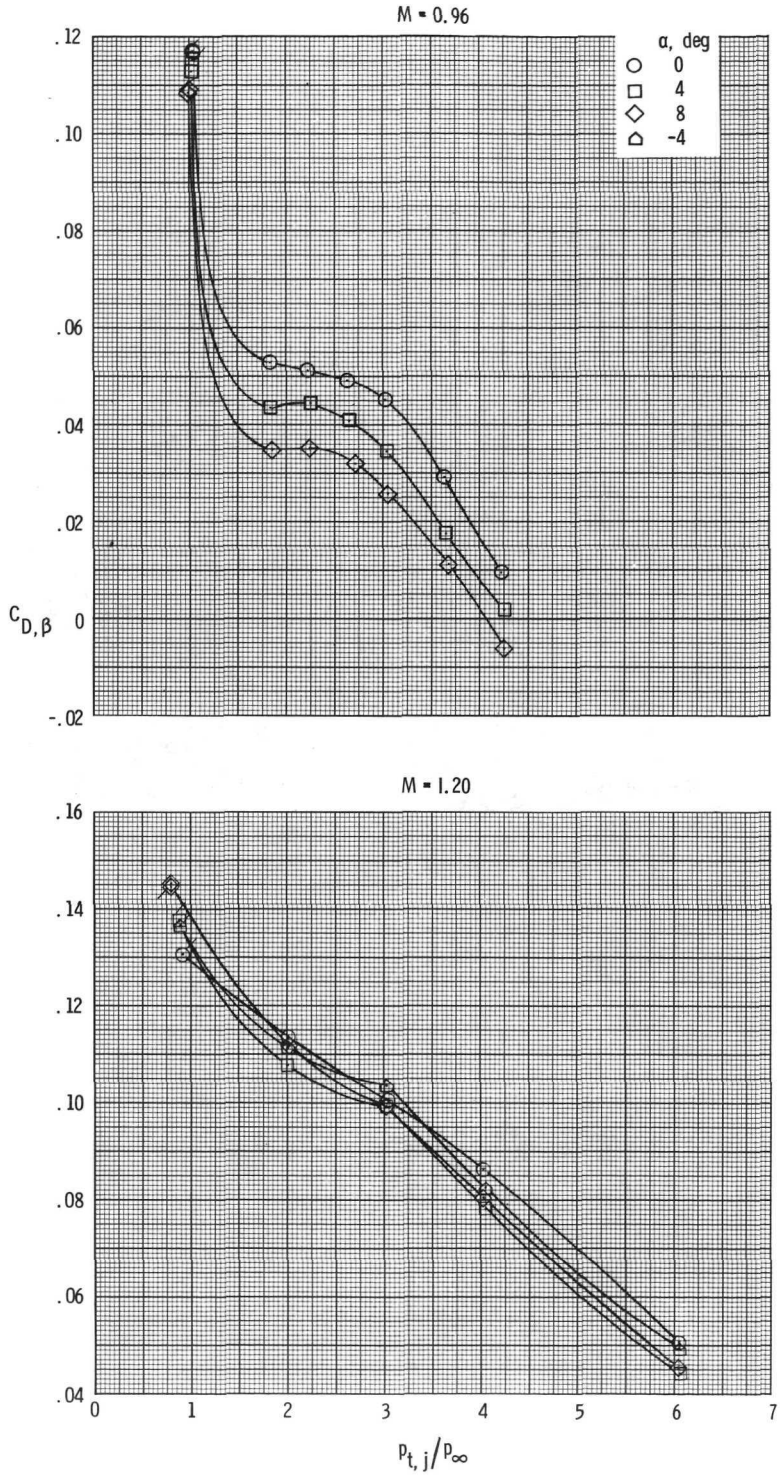
(b) M = 0.96 and 1.20.

Figure 32.- Concluded.



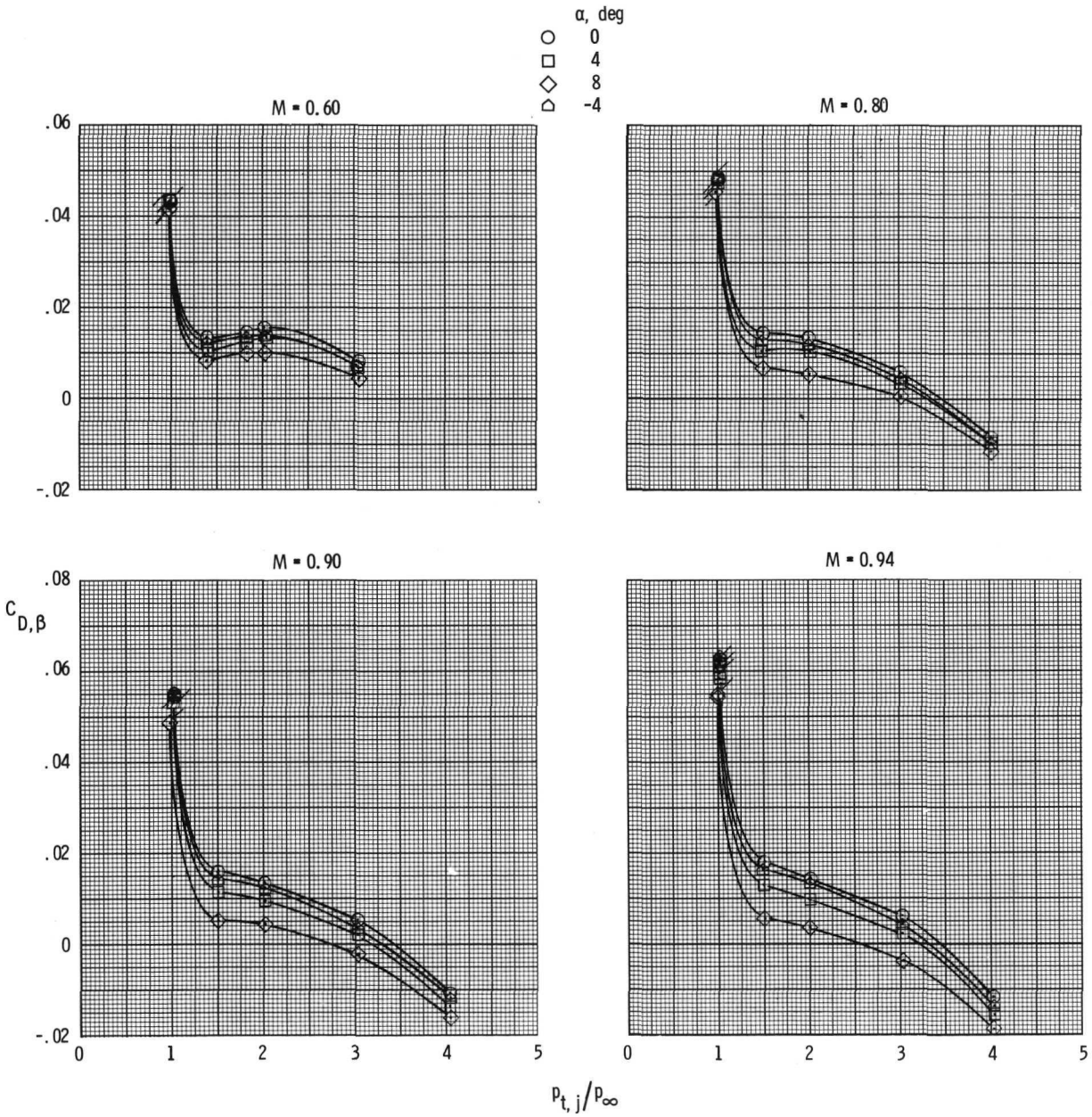
(a) M = 0.60, 0.80, 0.90, and 0.94.

Figure 33.- Effects of jet total-pressure ratio and angle of attack on the boattail drag coefficients of configuration 3 $\left(l/d_m = 1.0;\ d_e/d_m = 0.7\right)$.



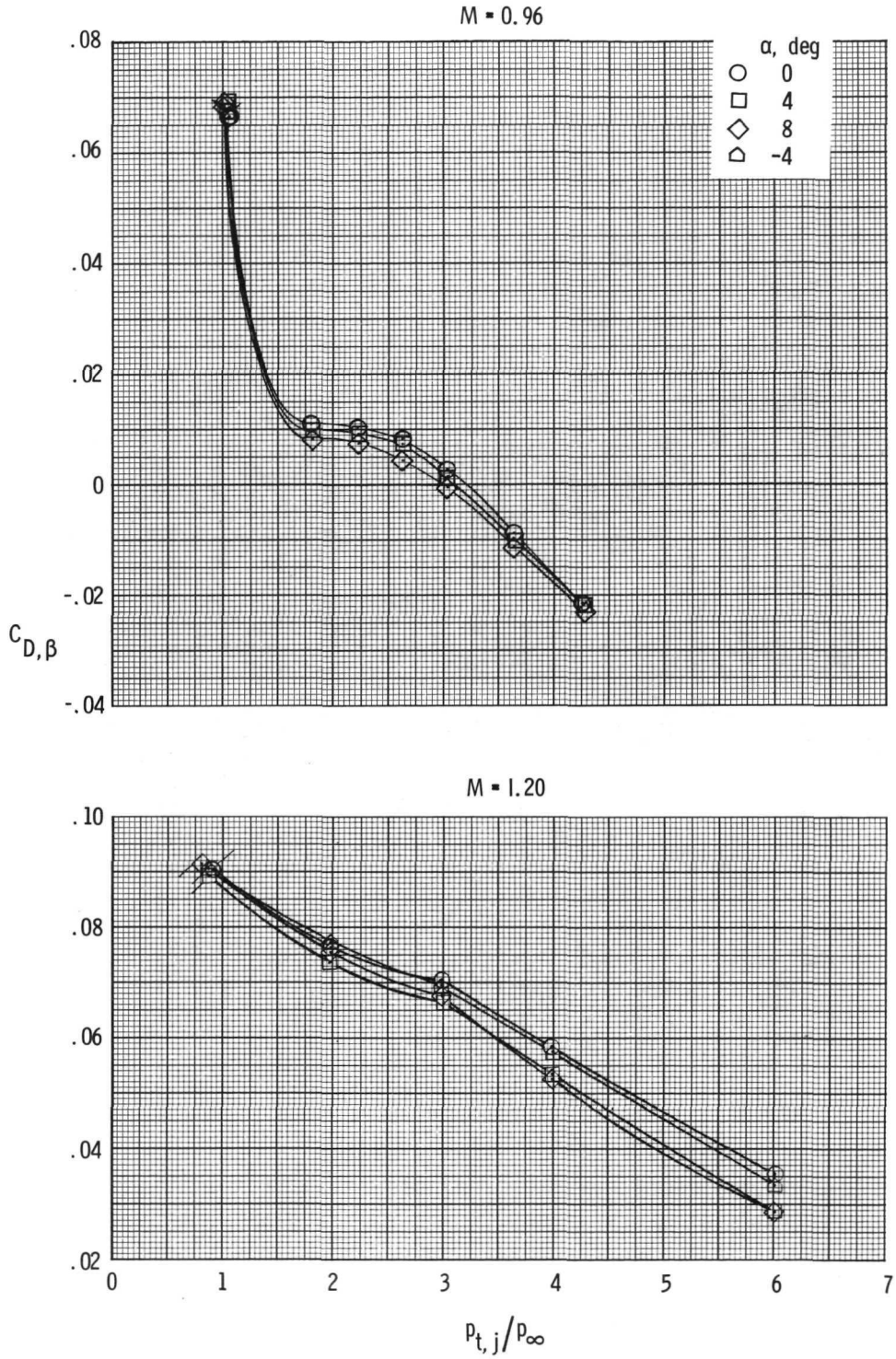
(b) M = 0.96 and 1.20.

Figure 33.- Concluded.



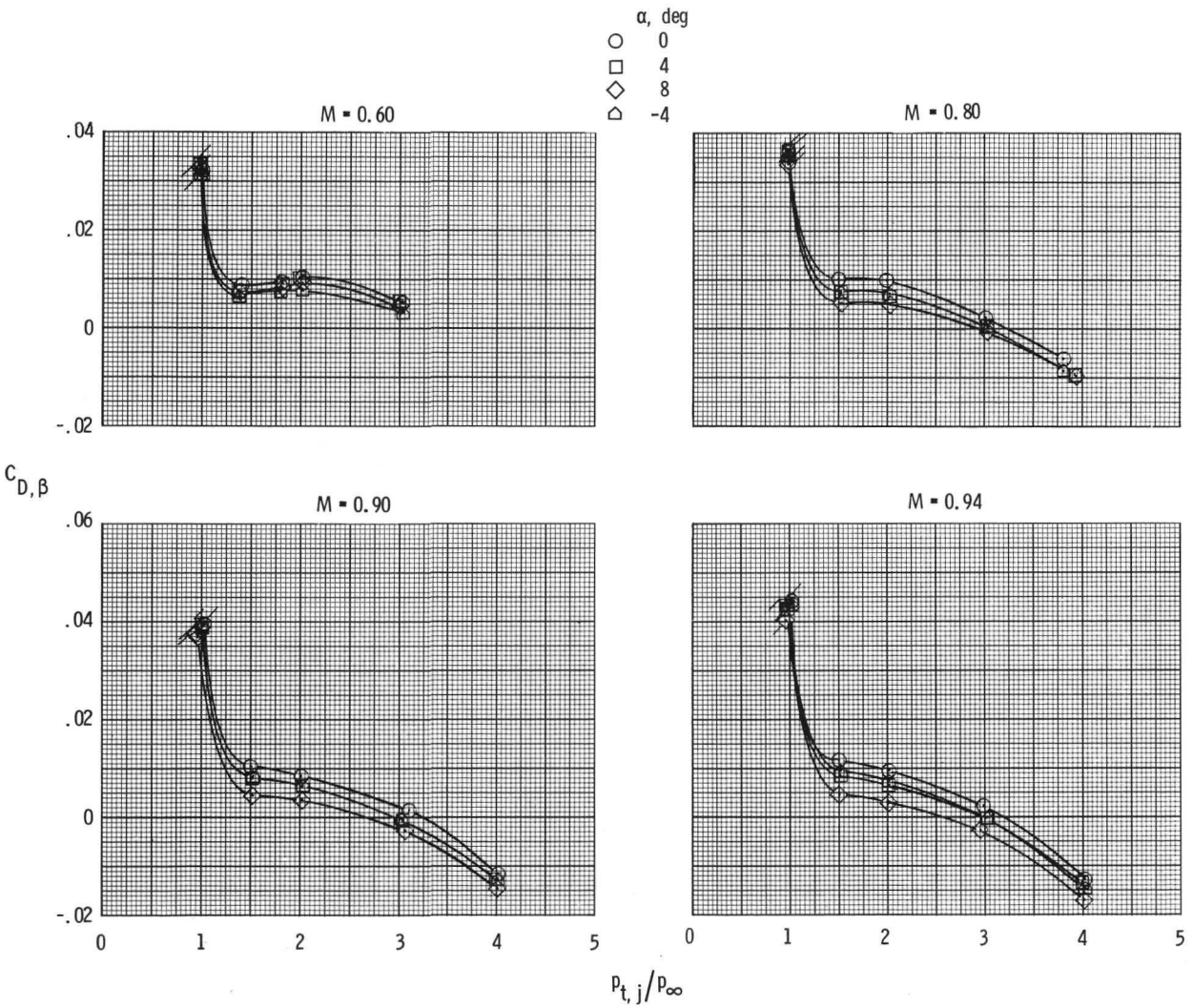
(a) M = 0.60, 0.80, 0.90, and 0.94.

Figure 34.- Effects of jet total-pressure ratio and angle of attack on the boattail drag coefficients of configuration 4 $\left(l/d_m = 1.5;\quad d_e/d_m = 0.7\right)$.



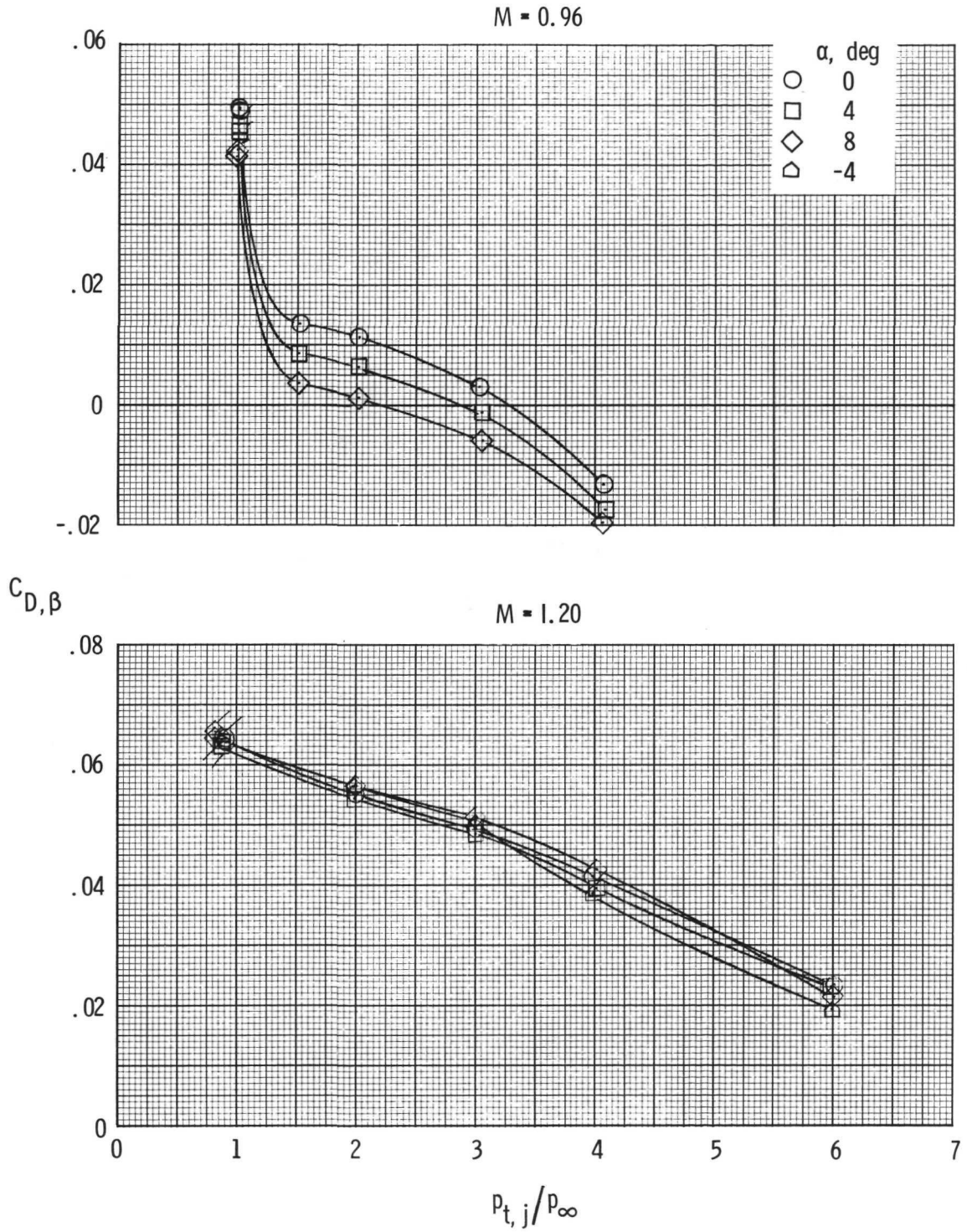
(b) M = 0.96 and 1.20.

Figure 34.- Concluded.



(a) M = 0.60, 0.80, 0.90, and 0.94.

Figure 35.- Effects of jet total-pressure ratio and angle of attack on the boattail drag coefficients of configuration 5 $\left(\ell/d_m = 2.0;\ d_e/d_m = 0.7\right)$.



(b) M = 0.96 and 1.20.

Figure 35.- Concluded.

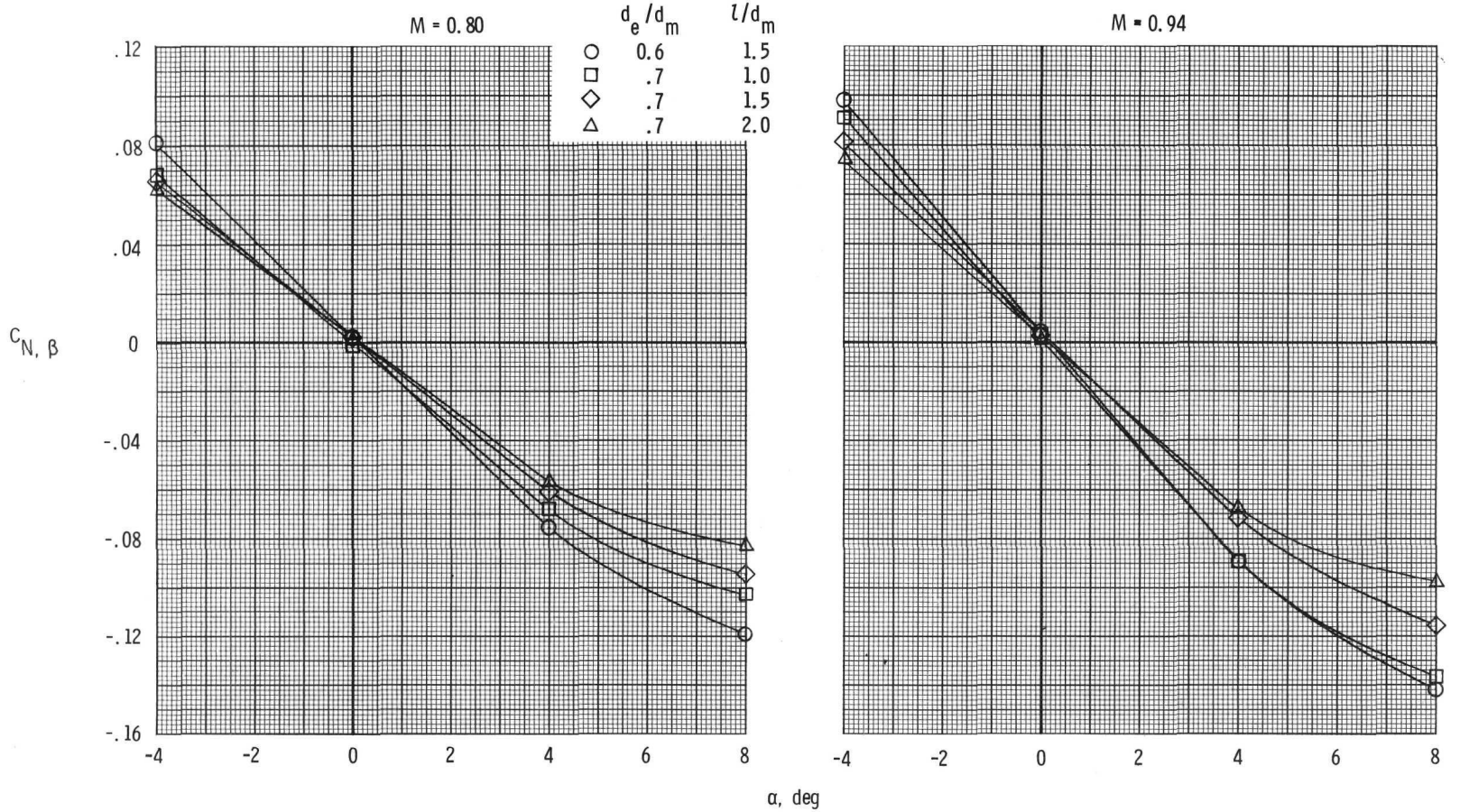


Figure 36.- Typical boattail normal-force coefficient variation with angle of attack for configurations 2 to 5 at a pressure ratio of about 2.

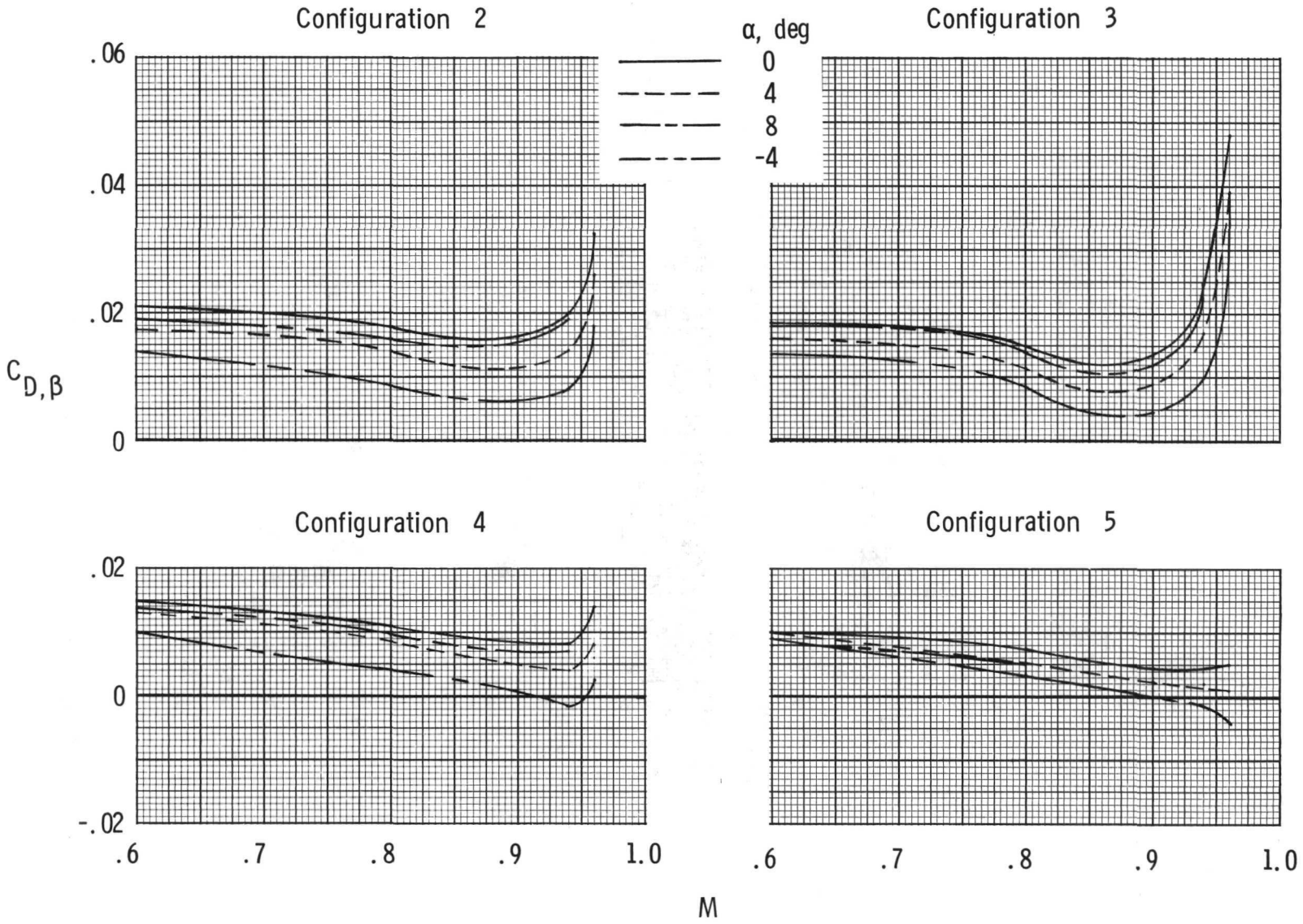


Figure 37.- Variation of boattail drag coefficient with Mach number and angle of attack for configurations 2 to 5 at the jet-total-pressure-ratio schedule of figure 25.

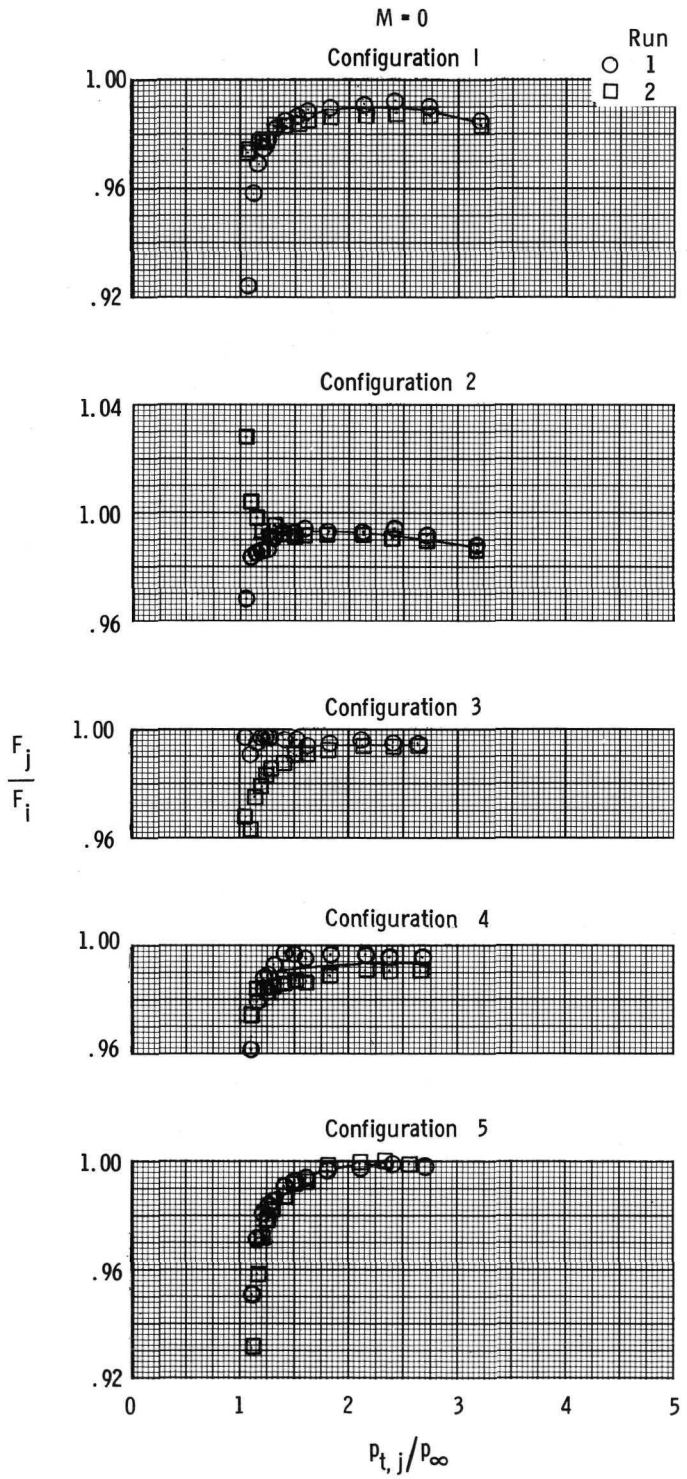


Figure 38.- Static thrust ratio variation with jet total-pressure ratio for all configurations.

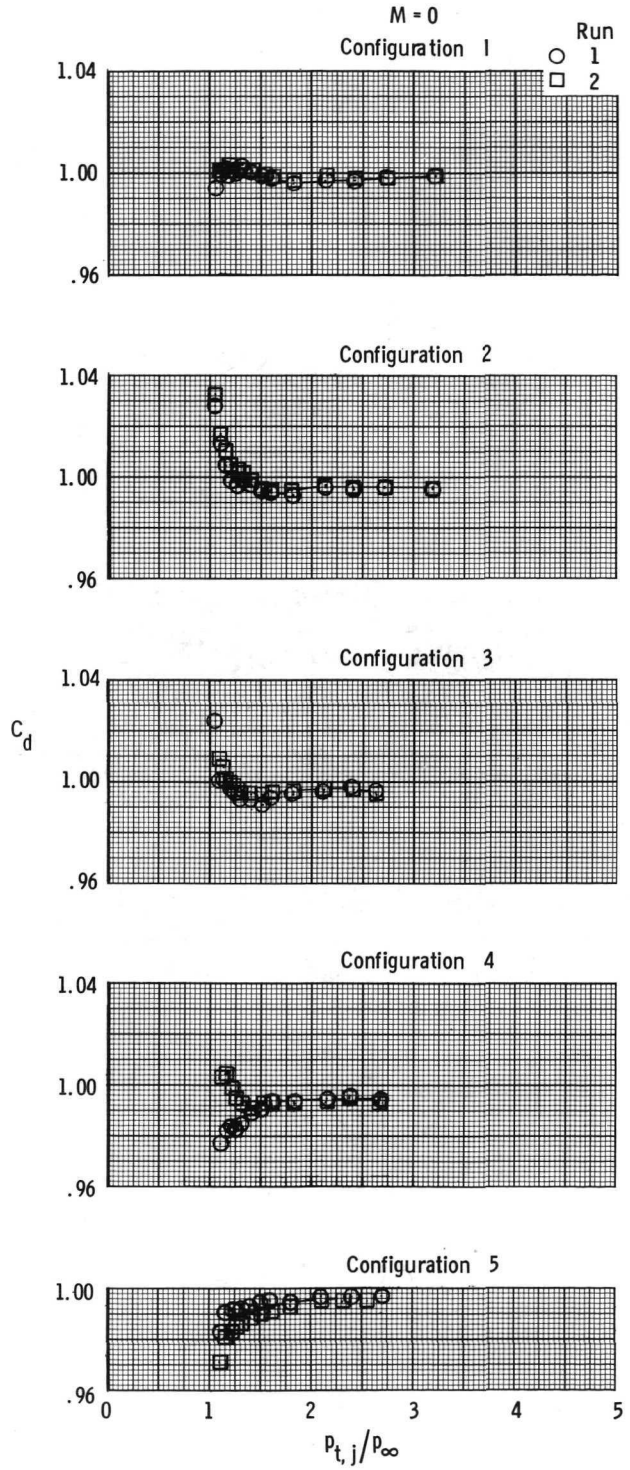


Figure 39.- Static discharge coefficient variation with jet total-pressure ratio for all configurations.

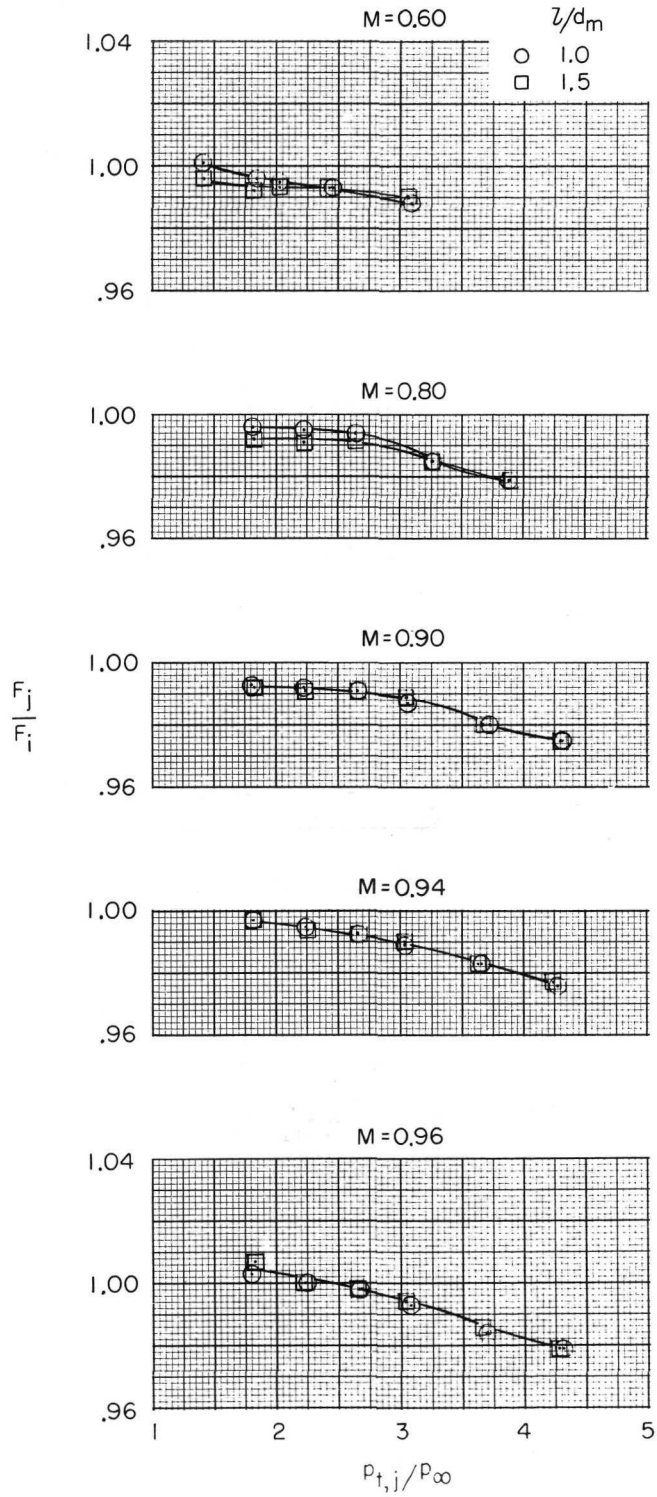


Figure 40.- Thrust ratio variation with jet total-pressure ratio for configurations 1 and 2 $\left(d_e/d_m = 0.6\right)$ at several Mach numbers.

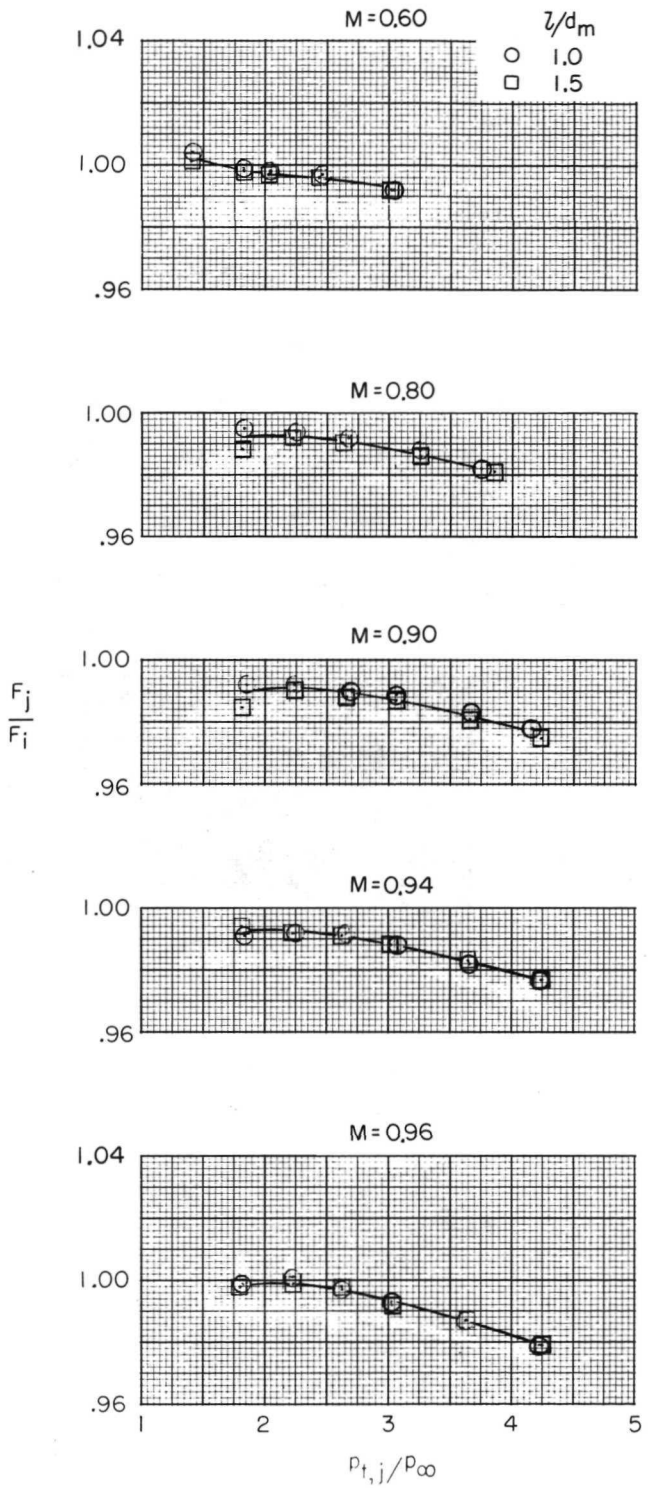


Figure 41.- Thrust ratio variation with jet total-pressure ratio for configurations 3 and 4 $\left(d_e/d_m = 0.7\right)$ at various Mach numbers.

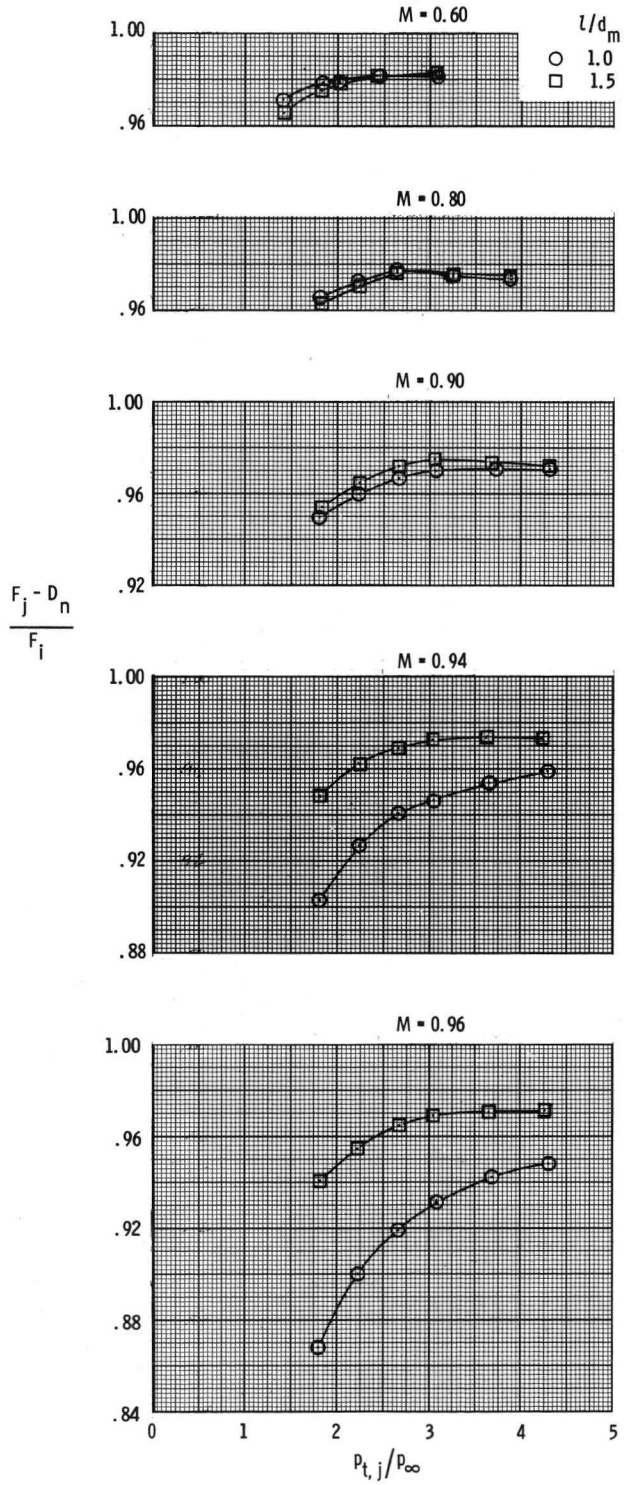


Figure 42.- Variation of thrust-minus-drag ratio with jet total-pressure ratio at several Mach numbers for configurations 1 and 2 $\left(d_e/d_m = 0.6\right)$.

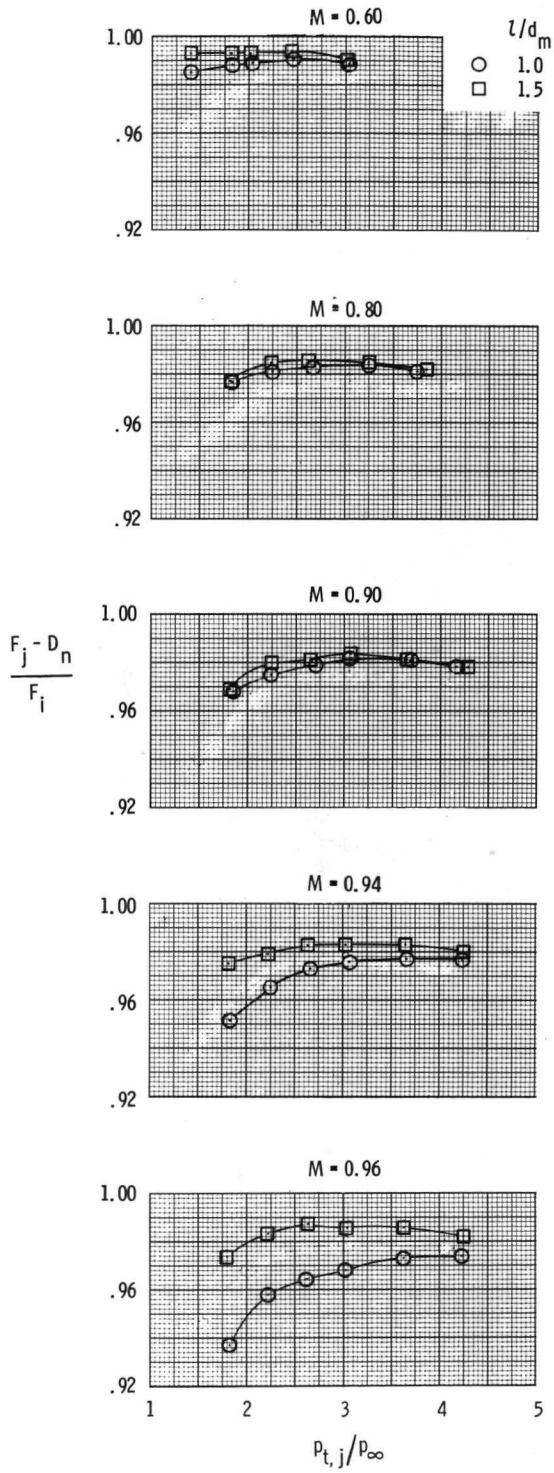
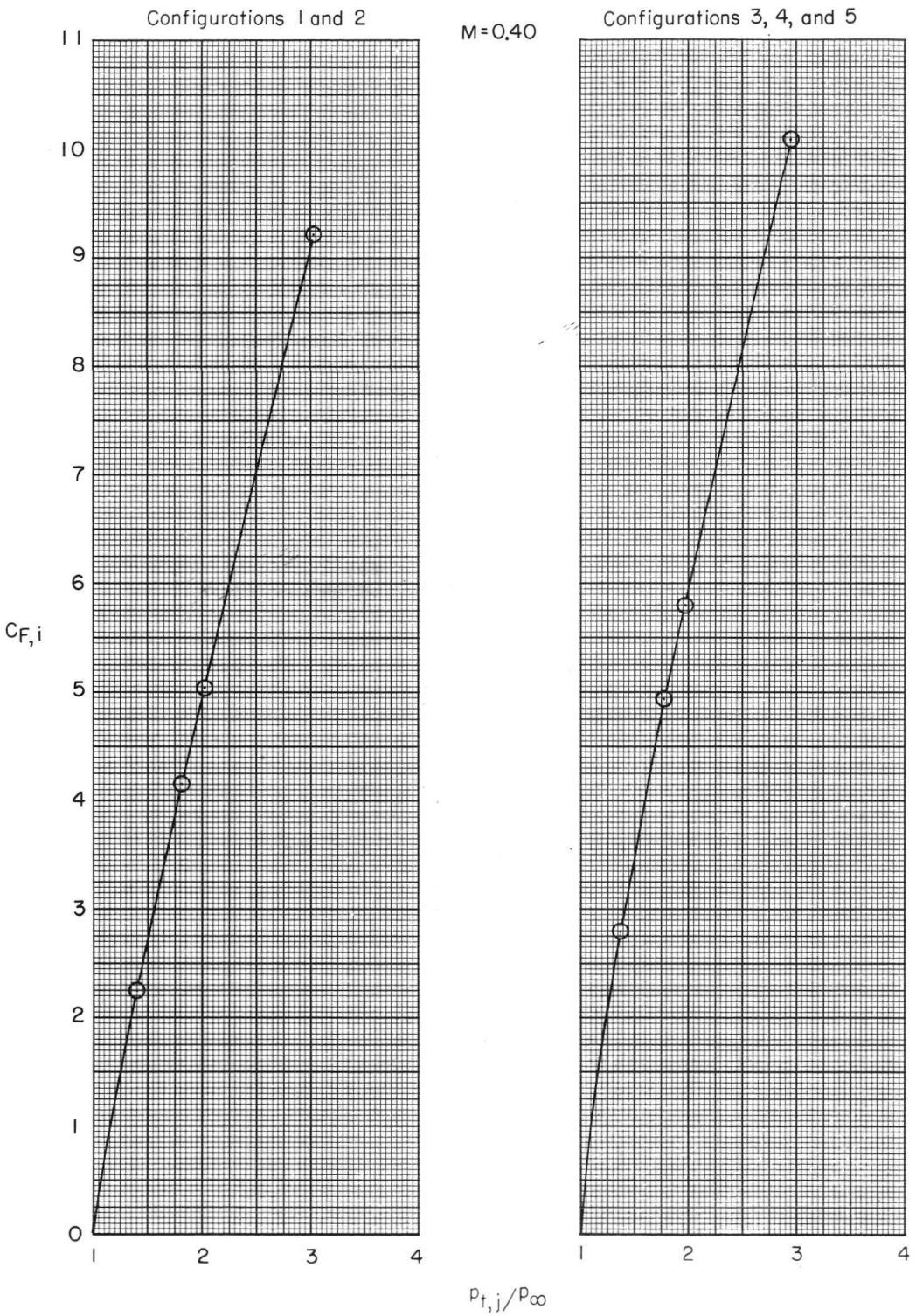
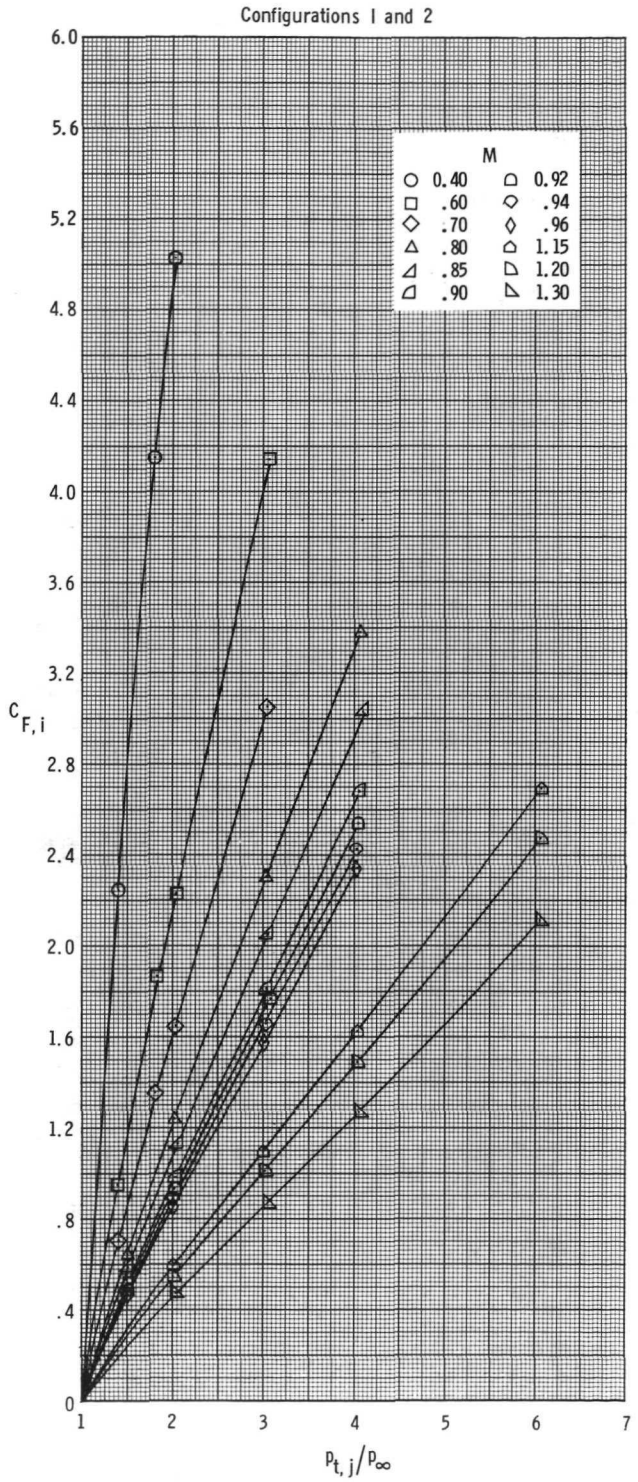


Figure 43.- Variation of thrust-minus-drag ratio with jet total-pressure ratio at several Mach numbers for configurations 3 and 4 $\left(d_e/d_m = 0.7\right)$.



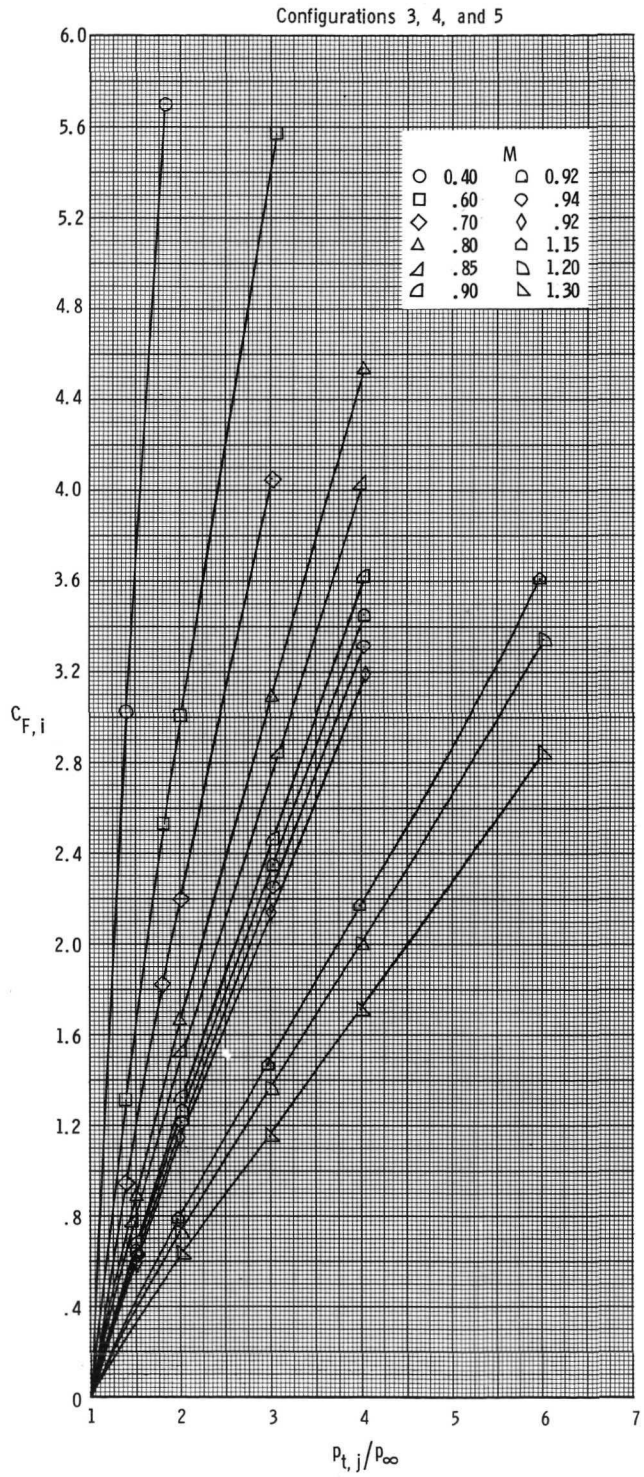
(a) M = 0.40; all configurations.

Figure 44.- Variation of aerodynamic ideal-thrust coefficient with jet total-pressure ratio for all configurations at various Mach numbers.



(b) Configurations 1 and 2 $(d_e/d_m = 0.6)$.

Figure 44.- Continued.



(c) Configurations 3, 4, and 5 $\left(d_e/d_m = 0.7\right)$.

Figure 44.- Concluded.

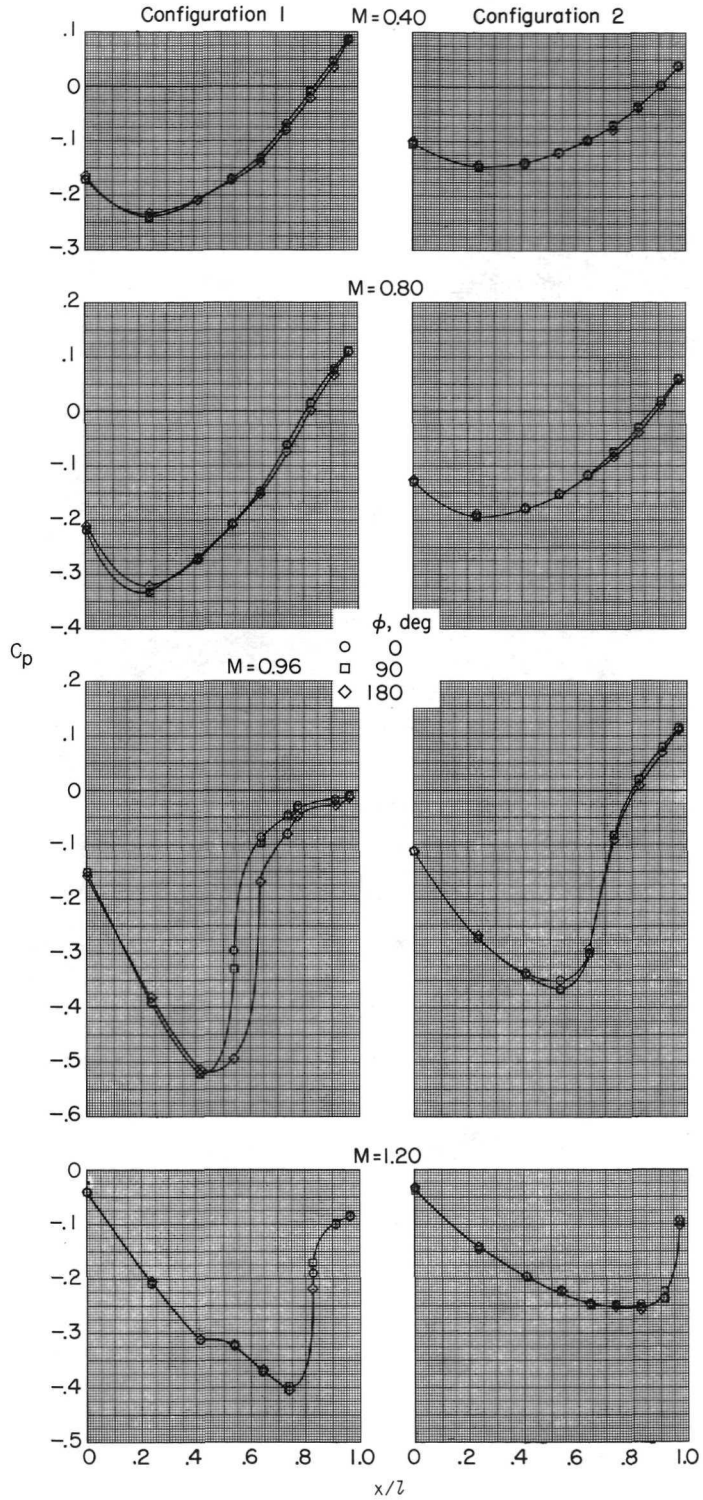
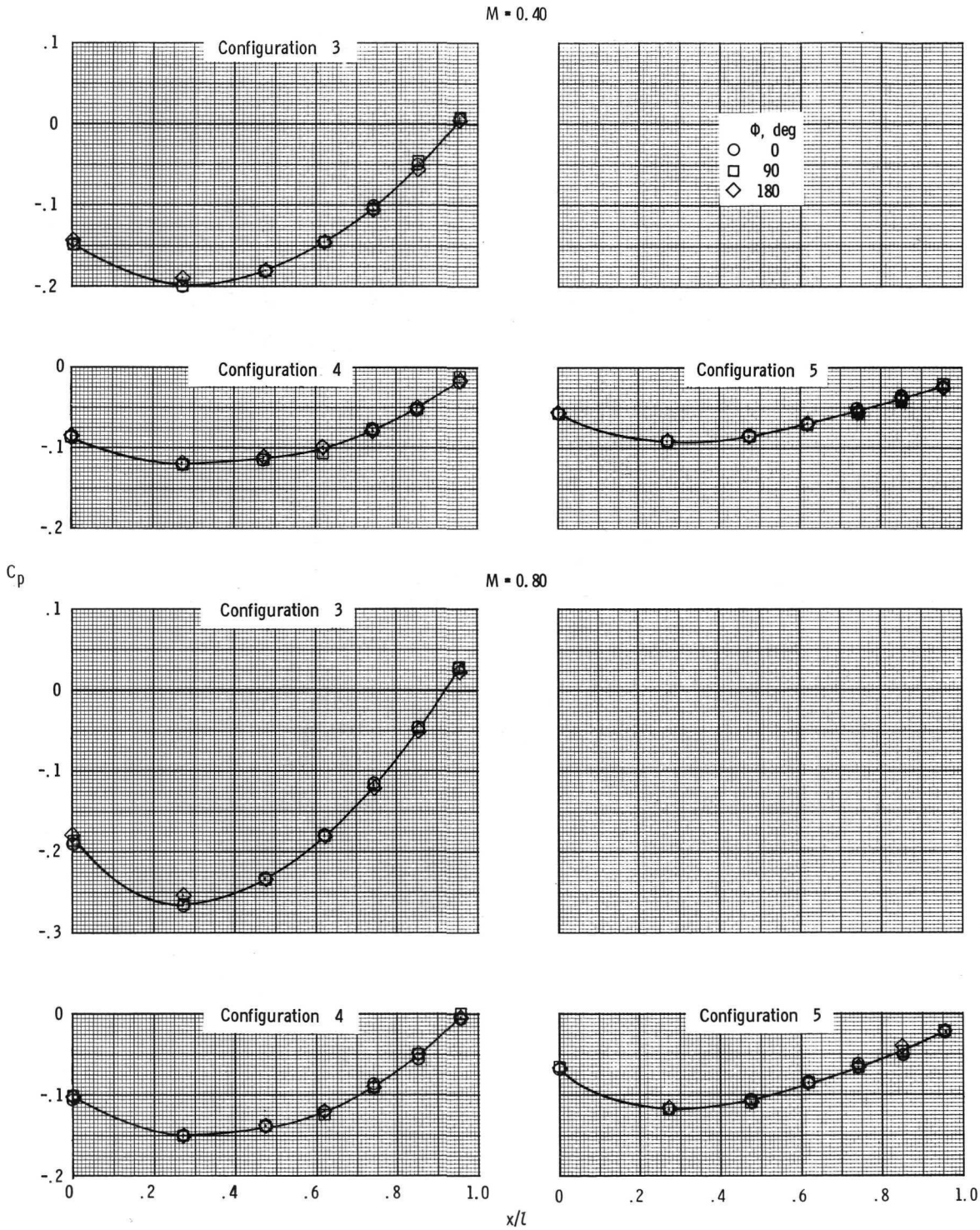
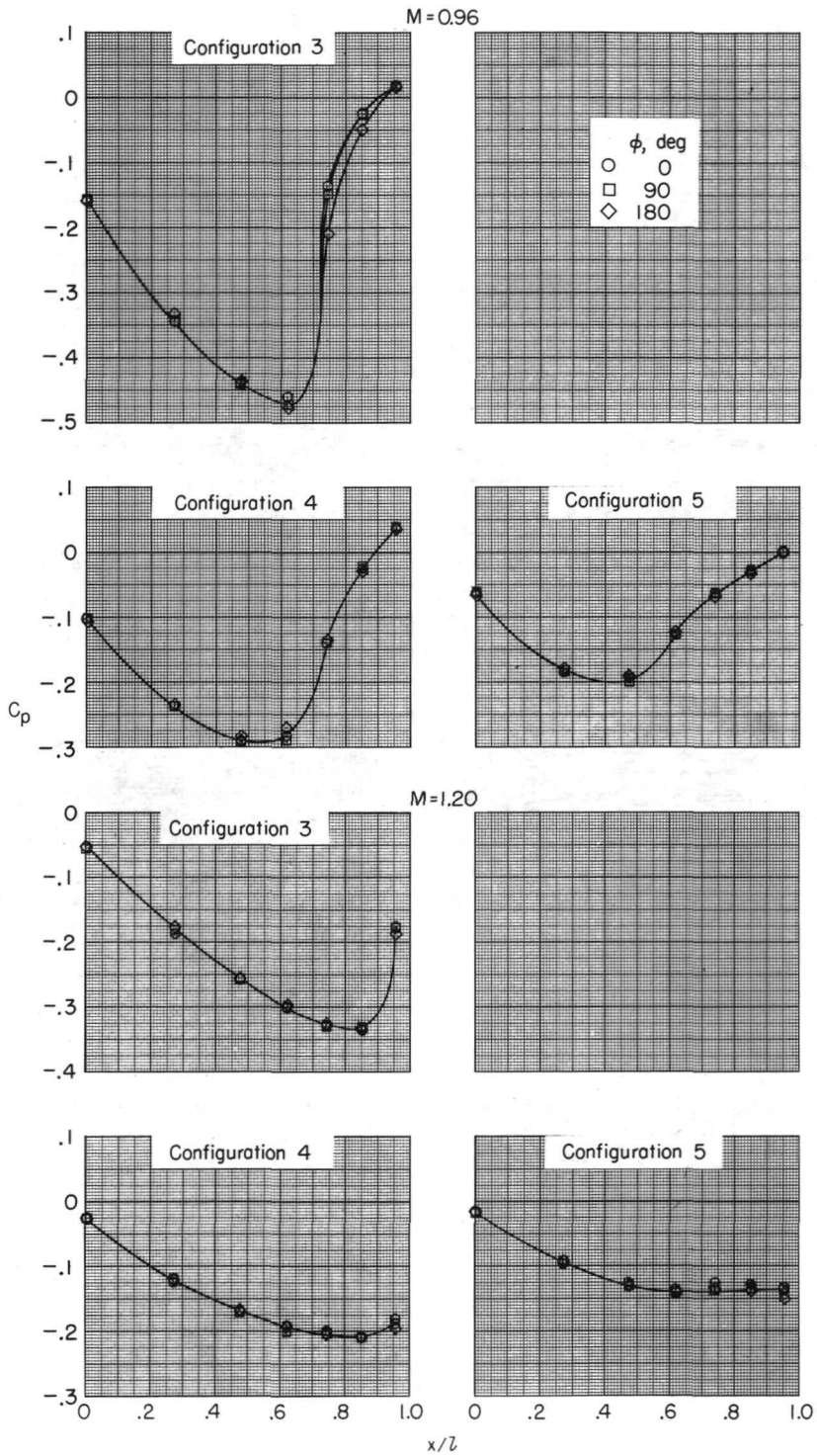


Figure 45.- Boattail longitudinal pressure-coefficient distributions for several values of ϕ at four selected Mach numbers for configurations 1 and 2 ($d_e/d_m = 0.6$; $l/d_m = 1.0$ and 1.5, respectively).



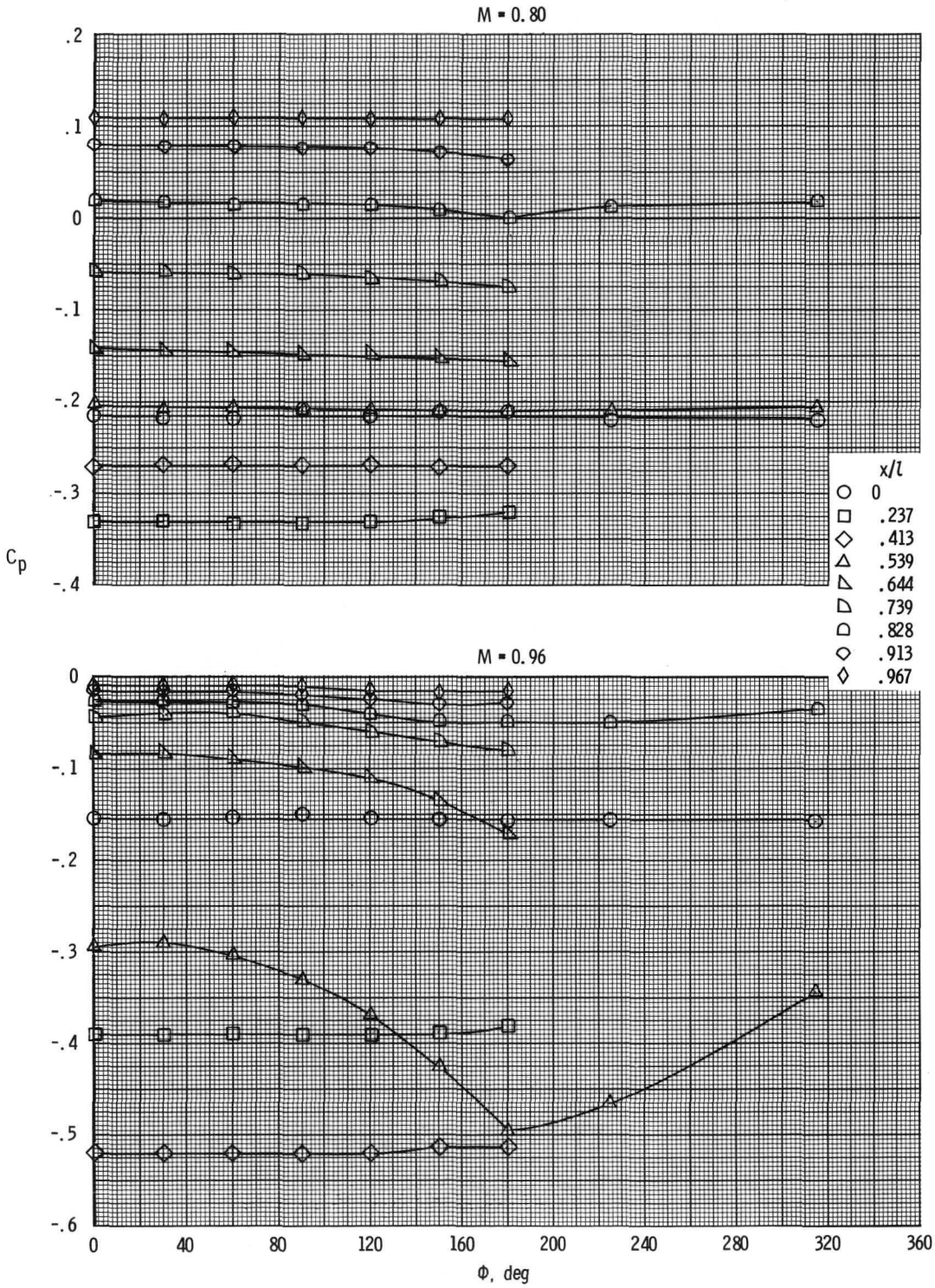
(a) M = 0.40 and 0.80.

Figure 46.- Boattail longitudinal pressure-coefficient distributions for several values of ϕ at four selected Mach numbers for configurations 3 to 5 $(d_e/d_m = 0.7;\ l/d_m = 1.0, 1.5, \text{and } 2.0)$.



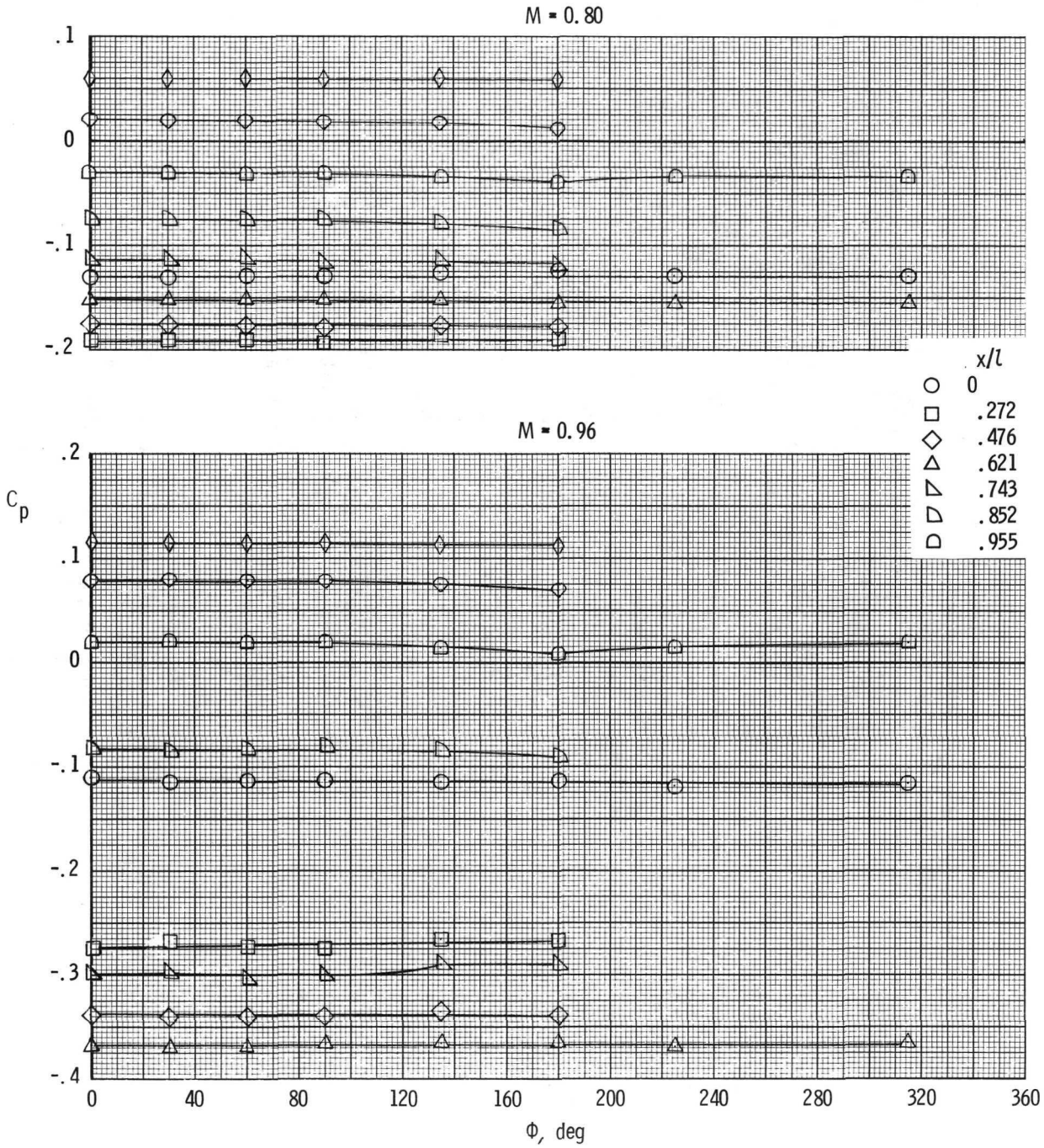
(b) M = 0.96 and 1.20.

Figure 46.- Concluded.



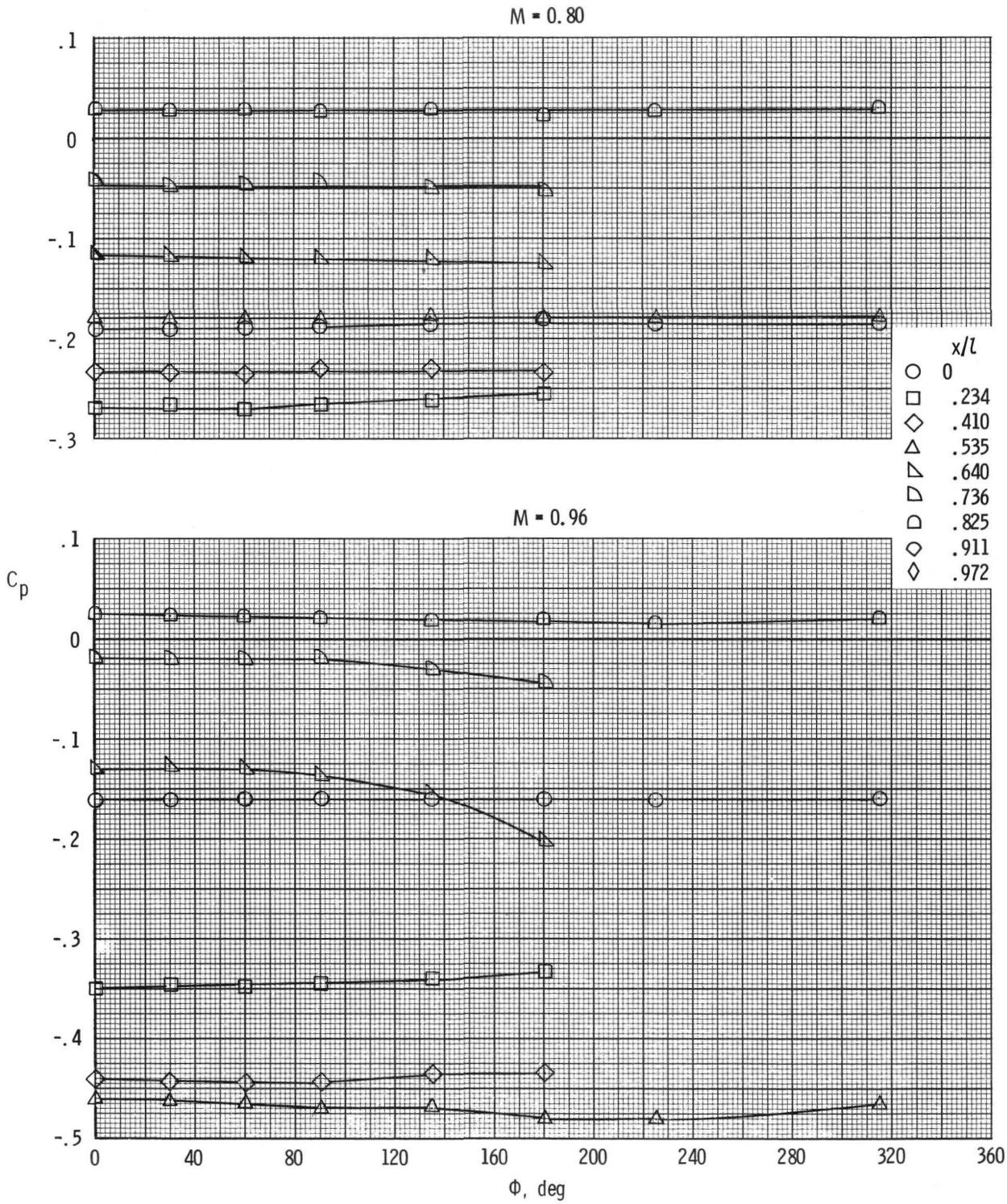
(a) Configuration 1 $\left(l/d_m = 1.0;\ d_e/d_m = 0.6\right)$.

Figure 47.- Variation of jet-off boattail pressure coefficients with ϕ for two Mach numbers and various x/l stations.



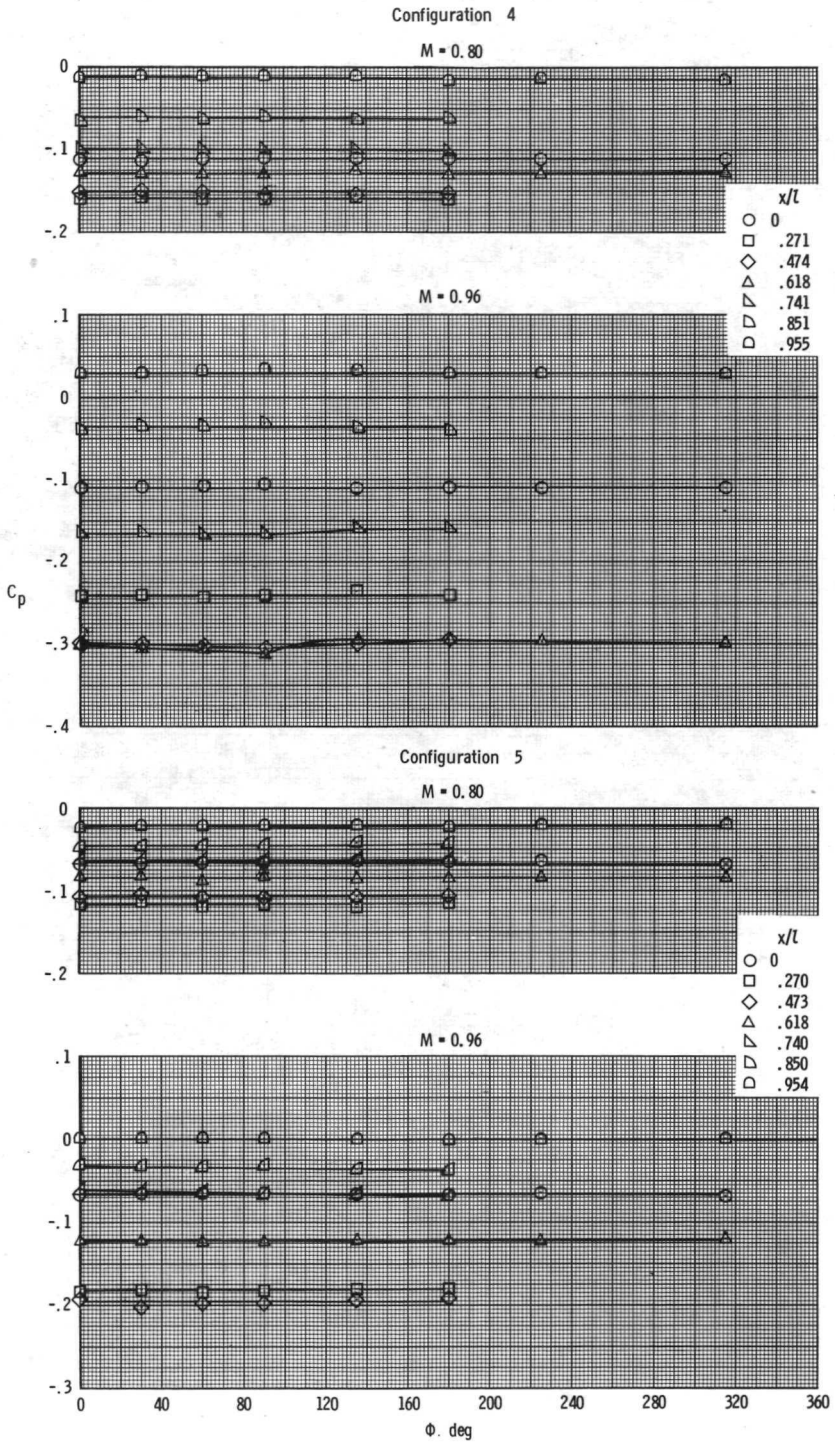
(b) Configuration 2 $\left(l/d_m = 1.5;\quad d_e/d_m = 0.6\right)$.

Figure 47.- Continued.



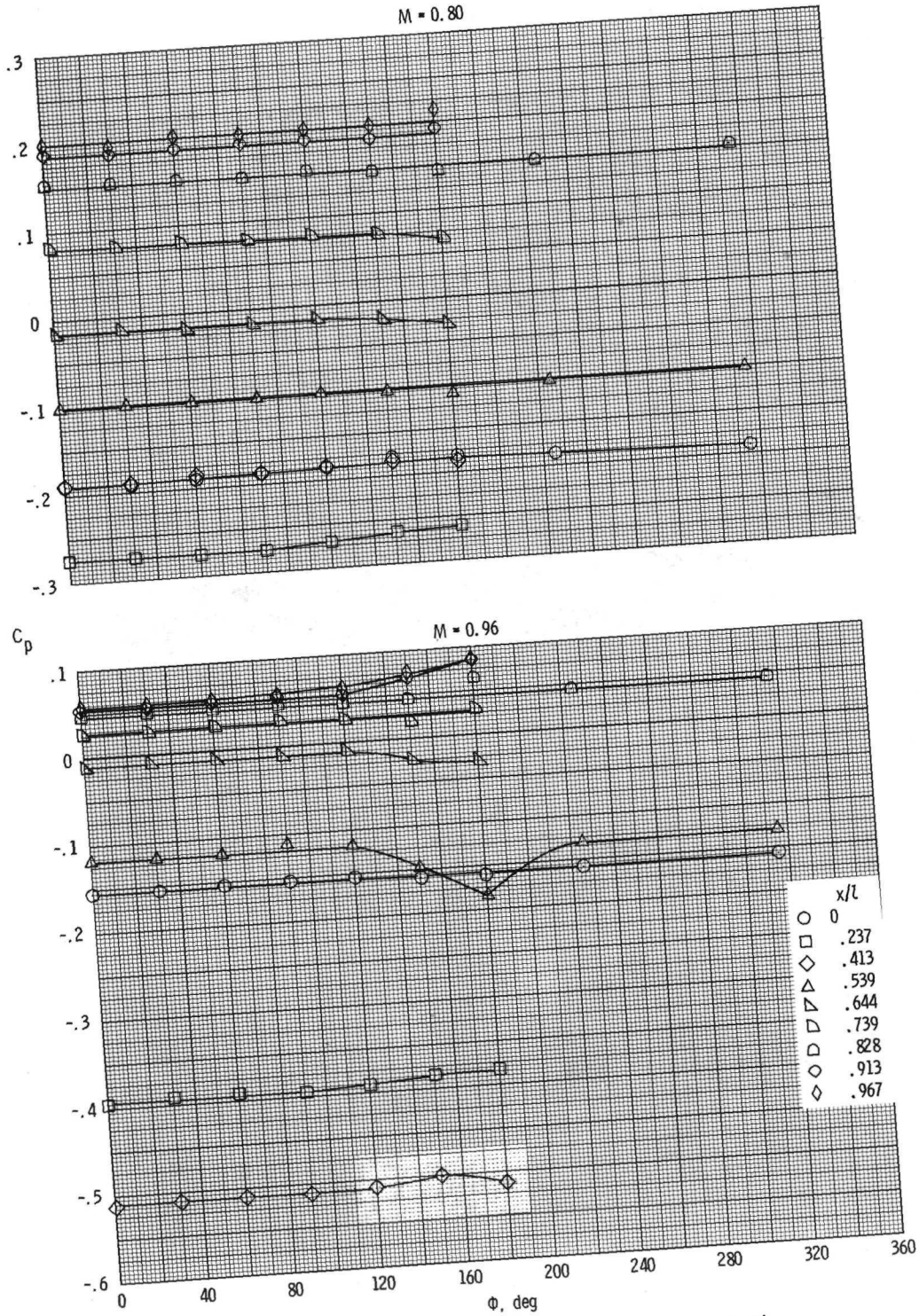
(c) Configuration 3 $\left(l/d_m = 1.0;\ \ d_e/d_m = 0.7\right)$.

Figure 47.- Continued.



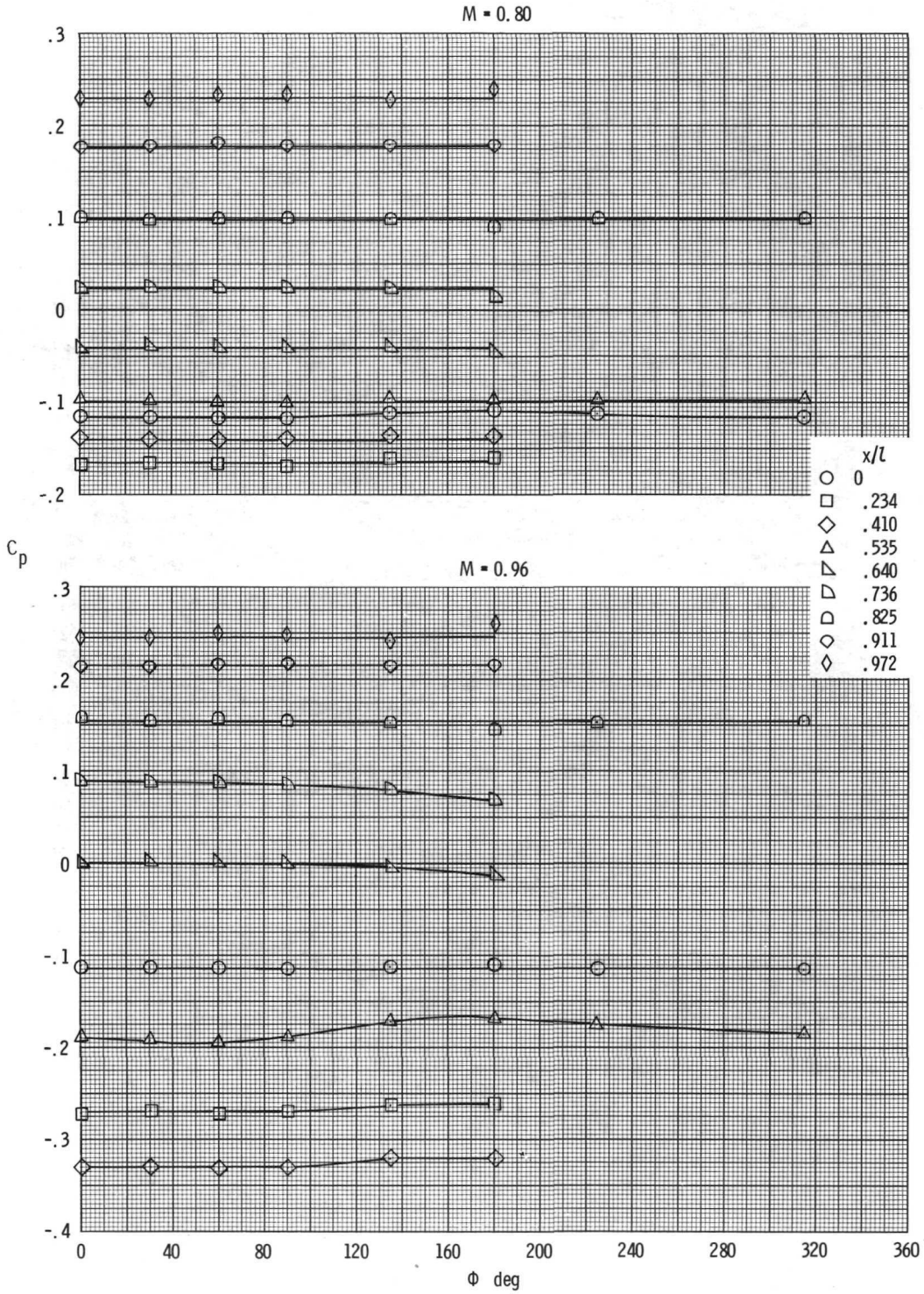
(d) Configurations 4 and 5 $\left(l/d_m = 1.5 \text{ and } 2.0;\ d_e/d_m = 0.7\right)$.

Figure 47.- Concluded.



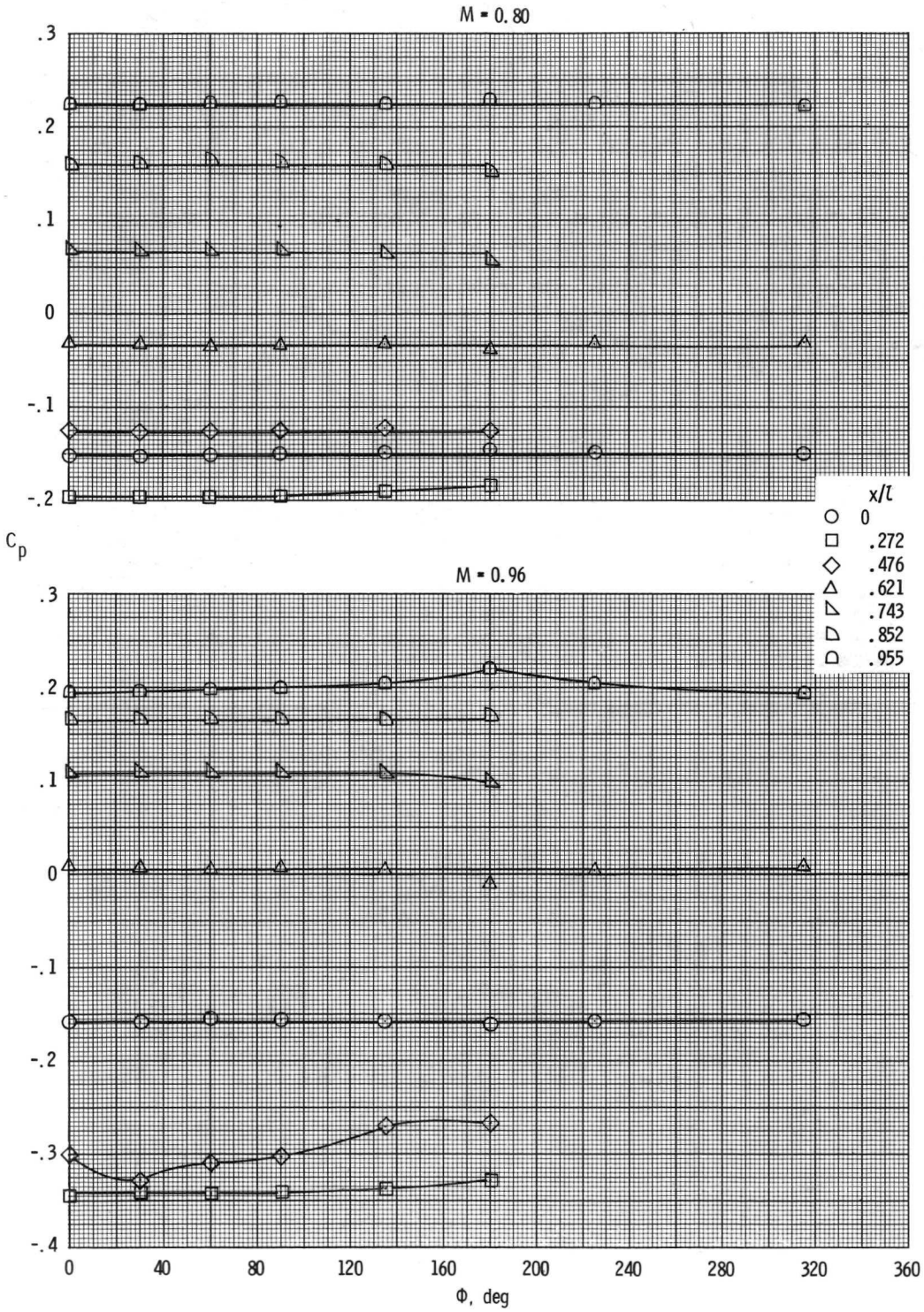
(a) Configuration 1 $\left(l/d_m = 1.0;\ \ d_e/d_m = 0.6\right)$.

Figure 48.- Variation of boattail pressure coefficients with ϕ for a jet total-pressure ratio of about 4 at two Mach numbers.



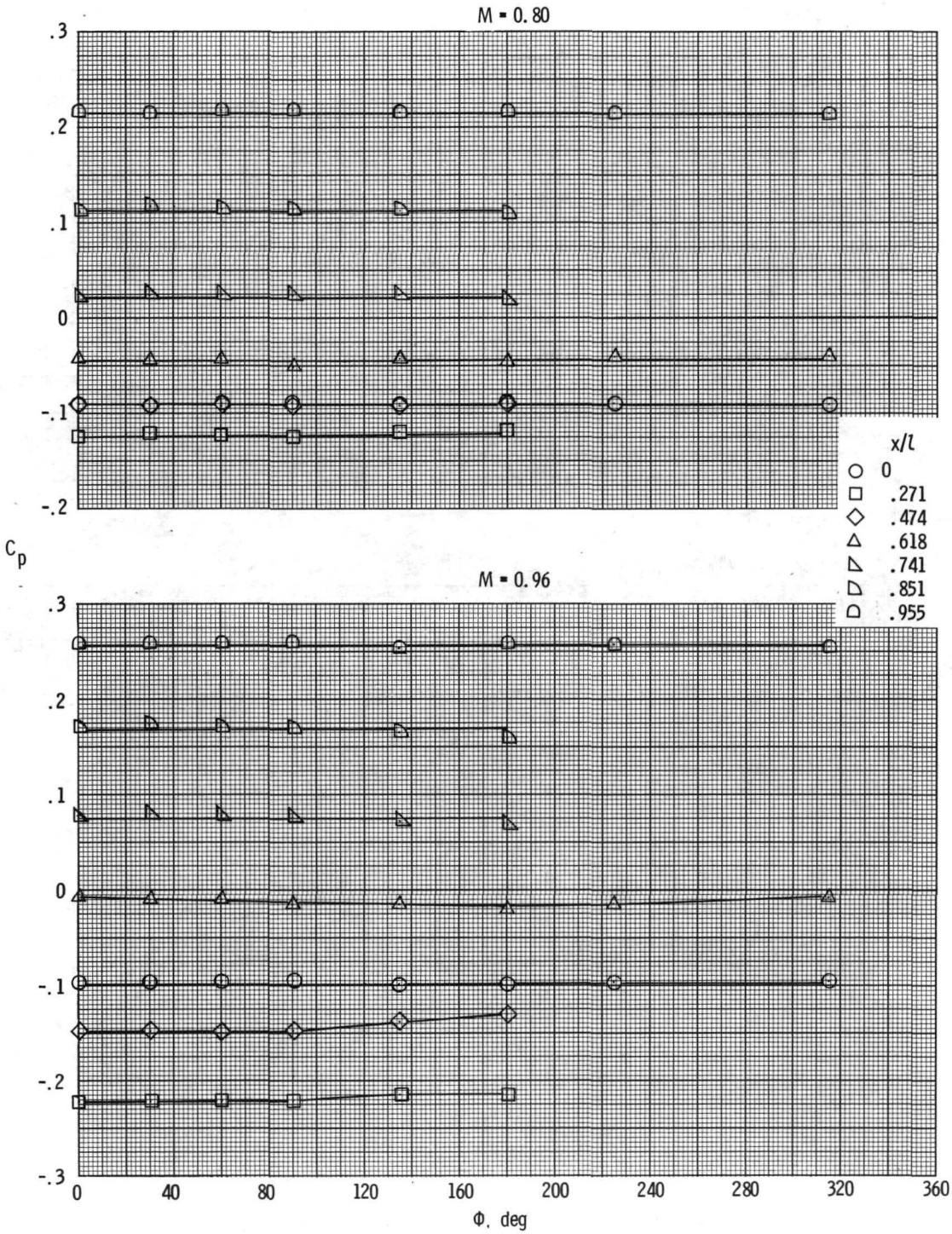
(b) Configuration 2 $\left(l/d_m = 1.5;\ \ d_e/d_m = 0.6\right)$.

Figure 48.- Continued.



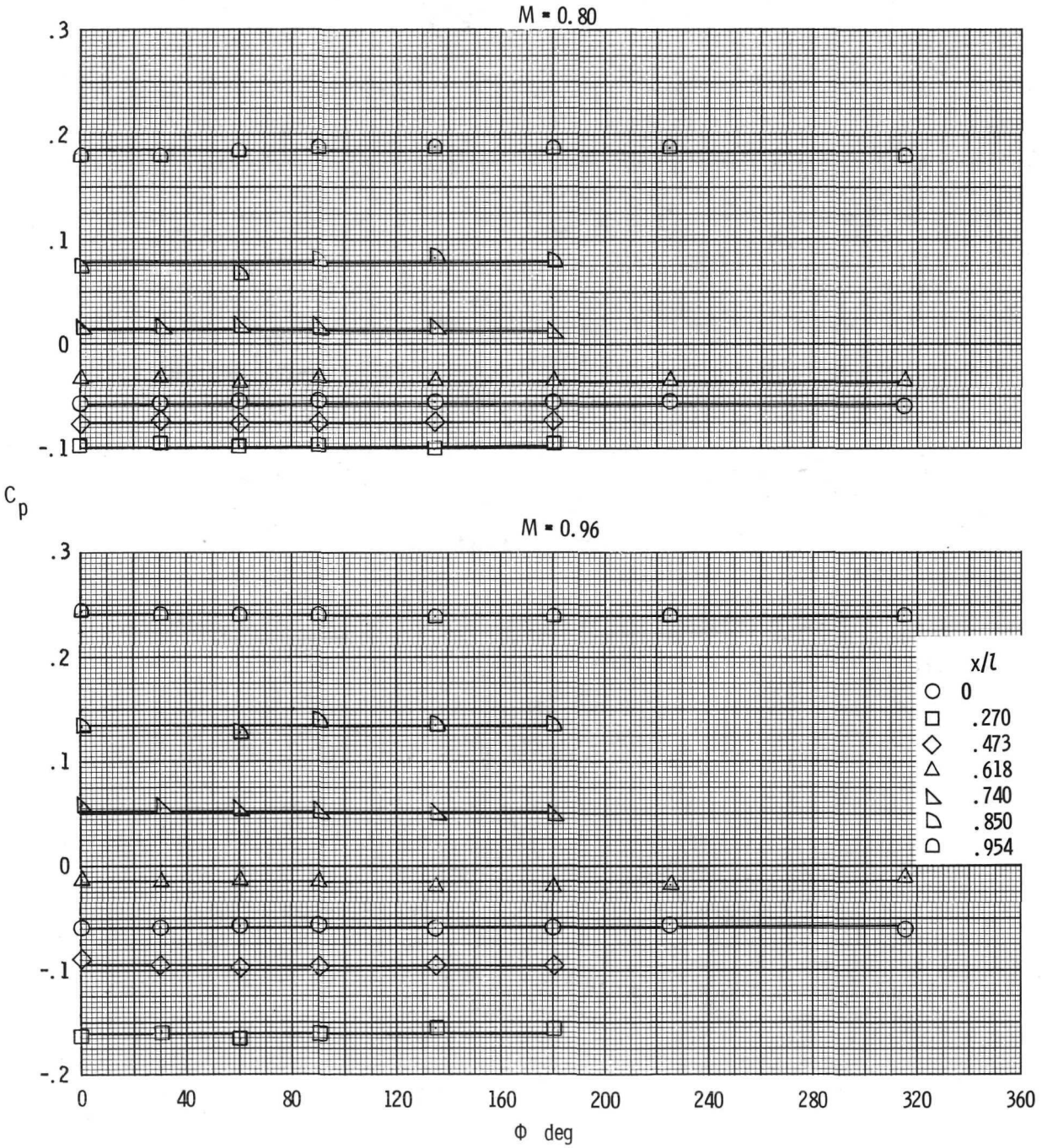
(c) Configuration 3 $\left(\ell/d_m = 1.0;\quad d_e/d_m = 0.7\right)$.

Figure 48.- Continued.



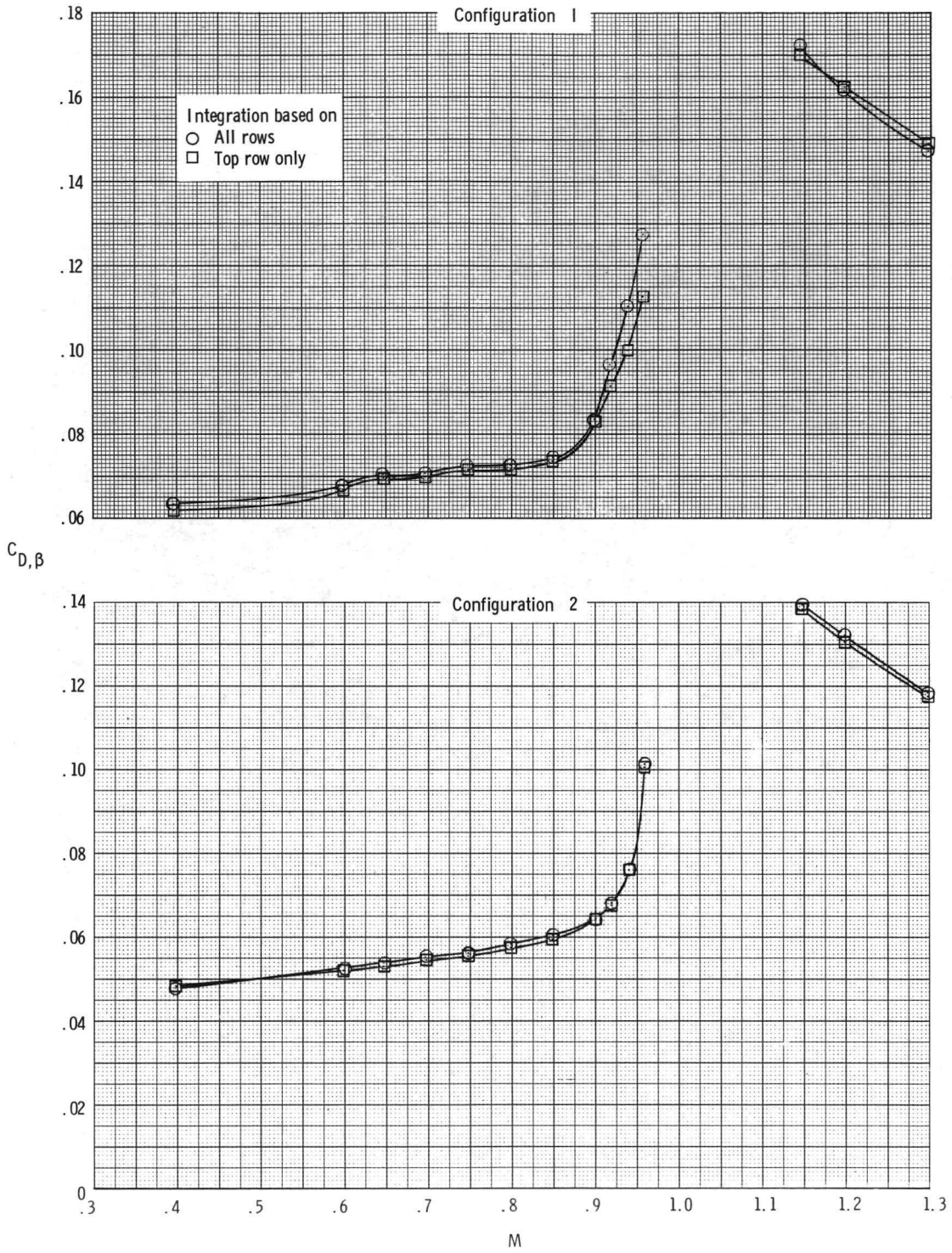
(d) Configuration 4 $\left(l/d_m = 1.5;\quad d_e/d_m = 0.7\right)$.

Figure 48.- Continued.



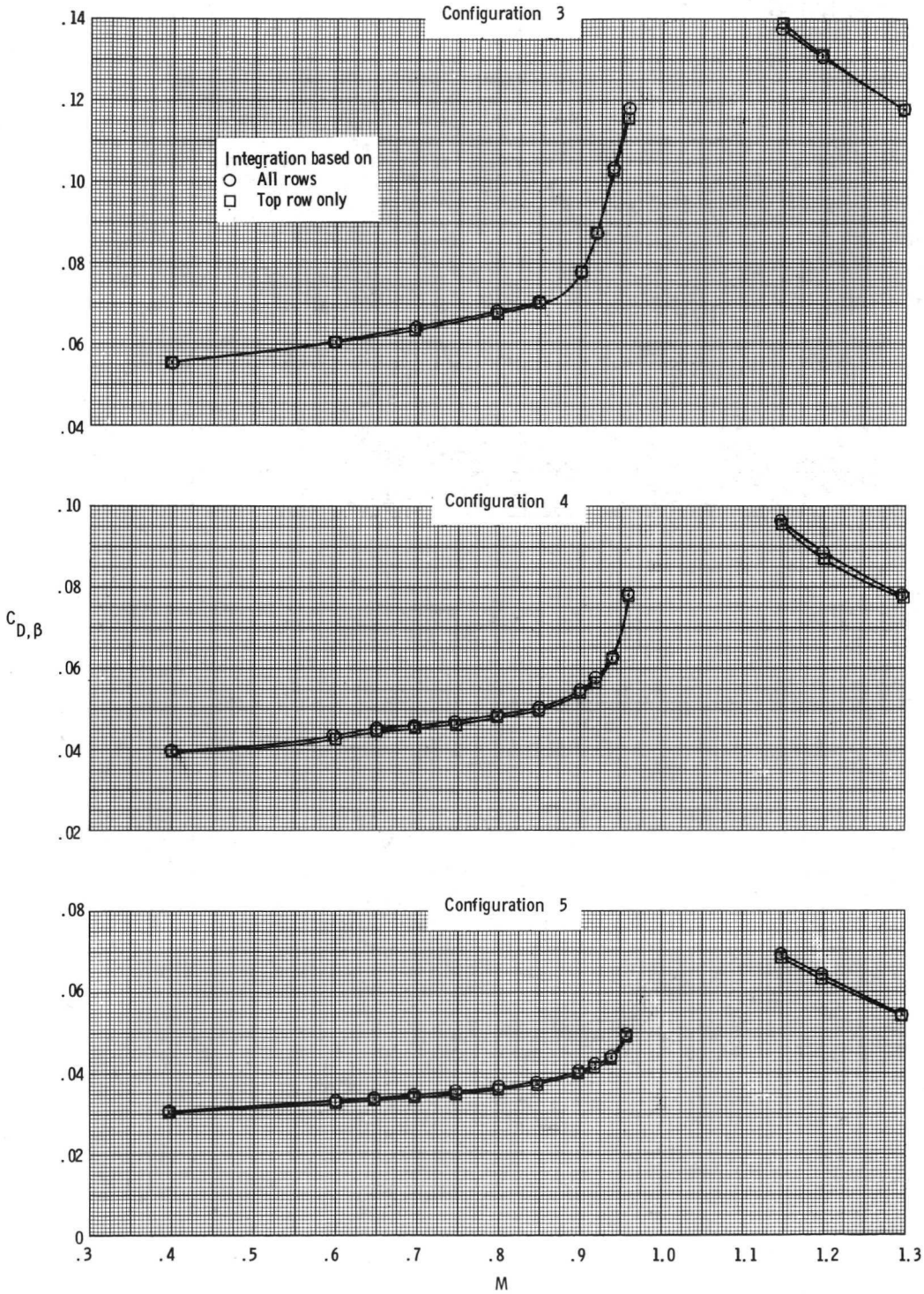
(e) Configuration 5 $\left(l/d_m = 2.0;\ \ d_e/d_m = 0.7\right)$.

Figure 48.- Concluded.



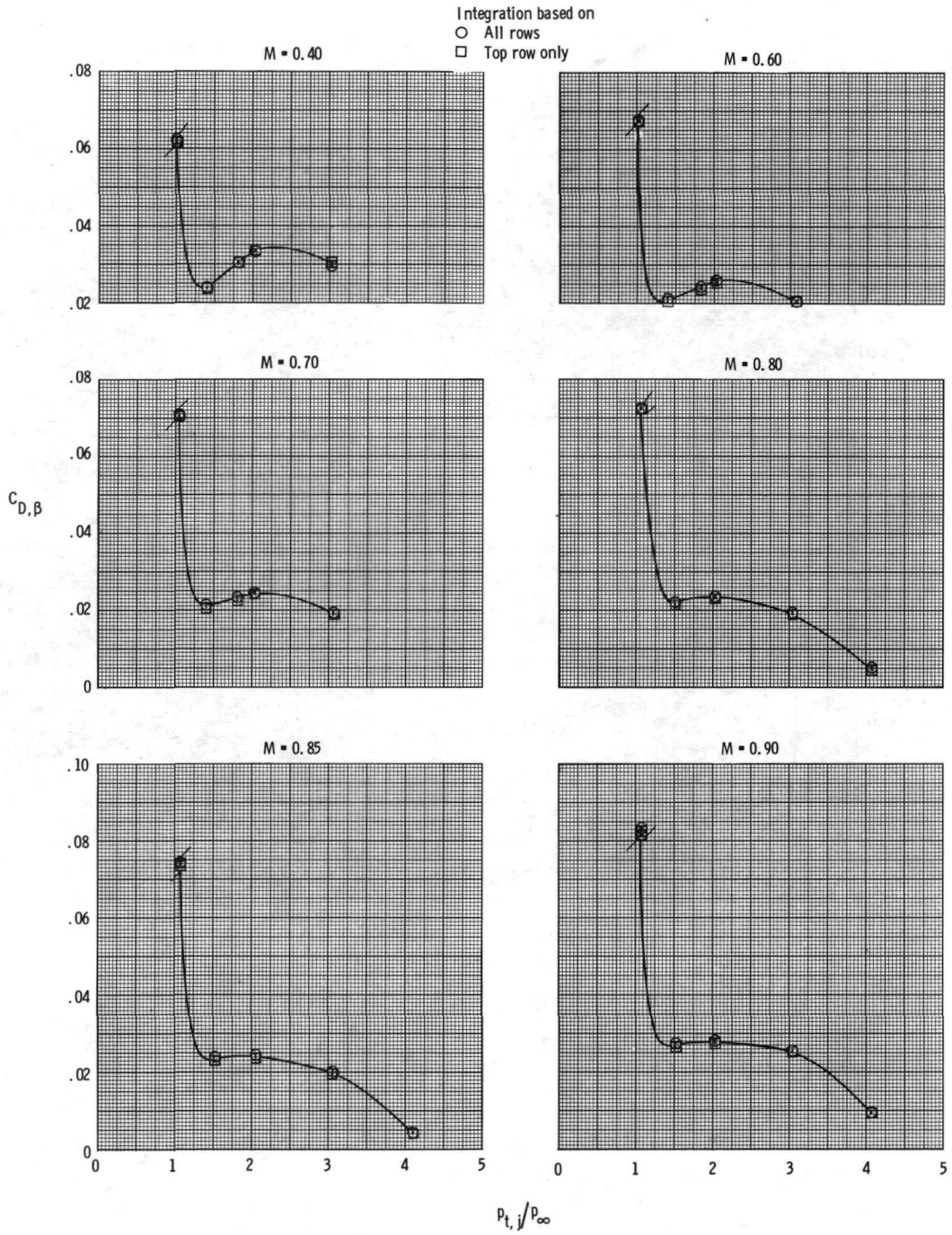
(a) Configurations 1 and 2 $\left(d_e/d_m = 0.6\right)$.

Figure 49.- Comparison of jet-off-boattail-drag variation with Mach number for integrations based on all orifices and on the top row of orifices only.



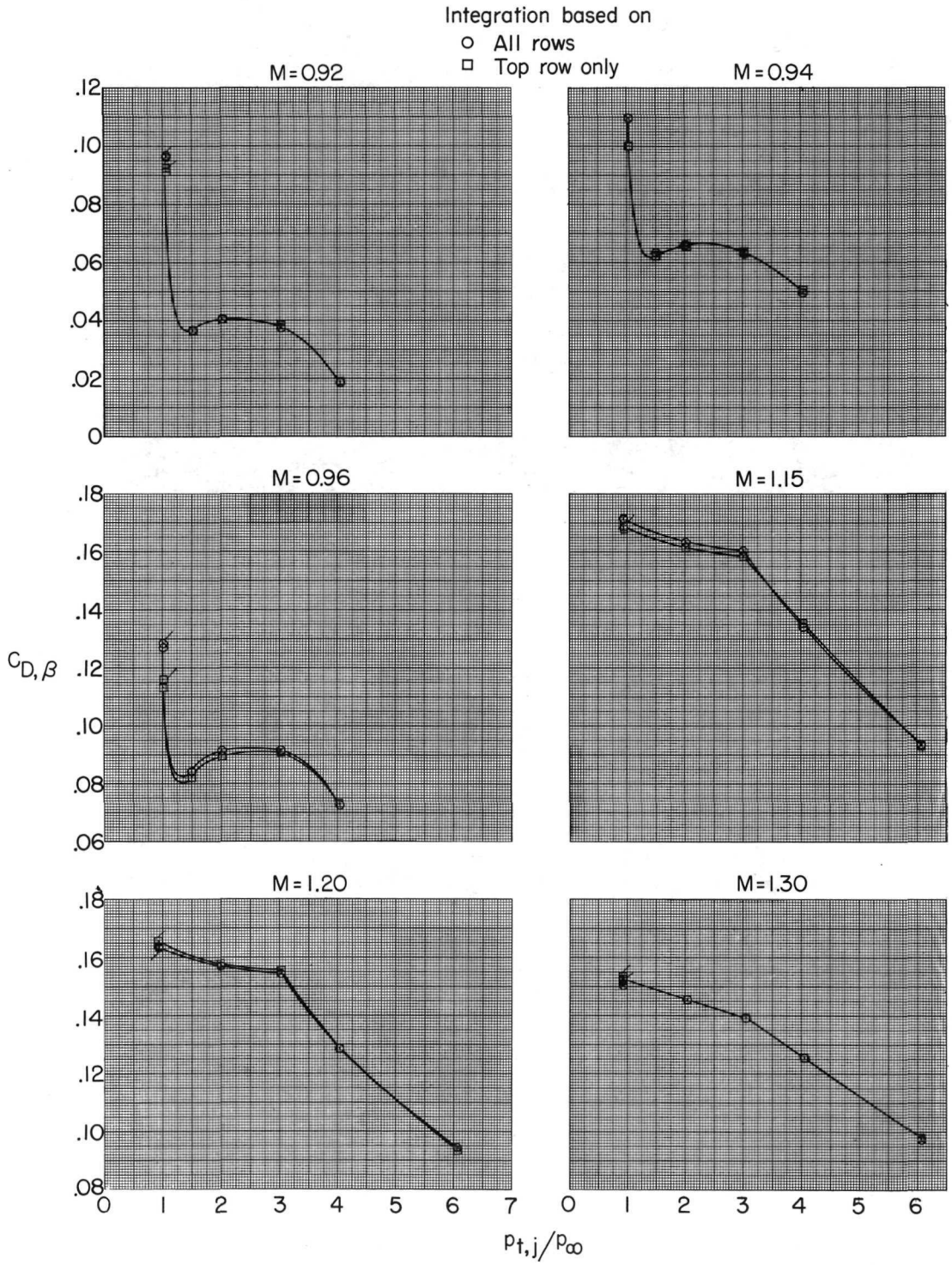
(b) Configurations 3, 4, and 5 $\left(d_e/d_m = 0.7\right)$.

Figure 49.- Concluded.



(a) M = 0.40, 0.60, 0.70, 0.80, 0.85, and 0.90.

Figure 50.- Comparison of boattail-drag variation with jet total-pressure ratio for integrations based on all orifices and on the top row of orifices only. Configuration 1 $\left(l/d_m = 1.0;\ d_e/d_m = 0.6\right)$.



(b) M = 0.92, 0.94, 0.96, 1.15, 1.20, and 1.30.

Figure 50.- Concluded.

*U.S. GOVERNMENT PRINTING OFFICE: 1973-739-027/28

NATIONAL AERONAUTICS AND SPACE ADMINISTRATION
WASHINGTON, D.C. 20546

OFFICIAL BUSINESS
PENALTY FOR PRIVATE USE $300

SPECIAL FOURTH-CLASS RATE
BOOK

POSTAGE AND FEES PAID
NATIONAL AERONAUTICS AND
SPACE ADMINISTRATION
451

U.S.MAIL

POSTMASTER : If Undeliverable (Section 158 Postal Manual) Do Not Return

"The aeronautical and space activities of the United States shall be conducted so as to contribute . . . to the expansion of human knowledge of phenomena in the atmosphere and space. The Administration shall provide for the widest practicable and appropriate dissemination of information concerning its activities and the results thereof."

—NATIONAL AERONAUTICS AND SPACE ACT OF 1958

NASA SCIENTIFIC AND TECHNICAL PUBLICATIONS

TECHNICAL REPORTS: Scientific and technical information considered important, complete, and a lasting contribution to existing knowledge.

TECHNICAL NOTES: Information less broad in scope but nevertheless of importance as a contribution to existing knowledge.

TECHNICAL MEMORANDUMS: Information receiving limited distribution because of preliminary data, security classification, or other reasons. Also includes conference proceedings with either limited or unlimited distribution.

CONTRACTOR REPORTS: Scientific and technical information generated under a NASA contract or grant and considered an important contribution to existing knowledge.

TECHNICAL TRANSLATIONS: Information published in a foreign language considered to merit NASA distribution in English.

SPECIAL PUBLICATIONS: Information derived from or of value to NASA activities. Publications include final reports of major projects, monographs, data compilations, handbooks, sourcebooks, and special bibliographies.

TECHNOLOGY UTILIZATION PUBLICATIONS: Information on technology used by NASA that may be of particular interest in commercial and other non-aerospace applications. Publications include Tech Briefs, Technology Utilization Reports and Technology Surveys.

Details on the availability of these publications may be obtained from:

SCIENTIFIC AND TECHNICAL INFORMATION OFFICE

NATIONAL AERONAUTICS AND SPACE ADMINISTRATION

Washington, D.C. 20546